



**TÉCNICO**  
LISBOA

# **Calibration and Validation of a 3D Homogenised Damage Model for FRP Composites**

**Damião Tavares Costa**

Thesis to obtain the Master of Science Degree in

**Aerospace Engineering**

Supervisors: Dr. José Manuel Cabecinhas de Almeida Gonilha  
Prof. Nuno Miguel Rosa Pereira Silvestre

## **Examination Committee**

Chairperson: Prof. Fernando José Parracho Lau  
Supervisor: Dr. José Manuel Cabecinhas de Almeida Gonilha  
Member of the Committee: Prof. Volnei Tita

**July 2022**



## **Declaration**

I declare that this document is an original work of my own authorship and that it fulfills all the requirements of the Code of Conduct and Good Practices of the Universidade de Lisboa.





## Acknowledgments

Firstly, I would like to thank Professor Nuno Silvestre for the great opportunity of developing this dissertation and expand my knowledge on the topic. I would also like to thank deeply Dr. José Gonilha for the continuous availability, fundamental guidance and feedback throughout the project, and Dr. Lourenço Fernandes for the help and clarification regarding the experimental data used.

A big thanks to my friends António, João, Luís, Rodrigo, Rui, and Serrano (in alphabetical order, so they don't discuss who is more important) for the laughs, and for the companionship during these years. Without them, it wouldn't have been the same.

I would also like to thank my family, my brothers, and specially my parents. Only their dedication and effort on giving me the best education and life conditions possible allowed me to be here.

Last but not least, a very special thanks to my girlfriend, Inês, who has supported me incessantly in good and bad times and whose company has been indispensable in the last years.



## Resumo

Devido ao aumento da utilização de materiais polímeros reforçados com fibra (FRP, sigla inglesa) em variadas indústrias, a necessidade de compreender e prever corretamente os mecanismos de falha destes materiais torna-se cada vez mais importante. A falta de confiança em modelos simples e a elevada complexidade de modelos mais recentes motivou o desenvolvimento de um novo modelo de dano progressivo para compósitos FRP pultrudidos que considera os materiais laminados como homogêneos. Neste estudo, apresenta-se a calibração e a validação do novo modelo para 6 polímeros reforçados com fibra de vidro (GFRP, sigla inglesa) de diferentes fornecedores. Para tal, foi utilizado o *software* ABAQUS juntamente com uma *user-defined material subroutine* (UMAT), previamente desenvolvida, para obter todos os resultados numéricos. O processo de calibração foi realizado através do ajuste das curvas numéricas aos resultados experimentais para todos os testes de caracterização mecânica disponíveis. Posteriormente, os materiais devidamente calibrados foram testados em ensaios de aplicação mais complexos e os resultados numéricos foram comparados com os experimentais. A calibração dos materiais foi realizada com sucesso, sendo que também foi demonstrada a necessidade de calibrar um parâmetro de regularização de malha com um teste de *compact tension*. O modelo foi também validado com sucesso, tendo sido capaz de prever a rigidez e força máxima dos ensaios de aplicação, os modos de falha e, em alguns casos, o comportamento pós-falha. Os resultados deste estudo demonstram a viabilidade de utilizar este novo modelo em projetos de dimensionamento estrutural.

**Palavras-chave:** Polímero Reforçado com Fibra de Vidro (GFRP), Modelo de Dano, Dano Progressivo, Elementos Finitos, Análise Numérica.



## Abstract

With the increasing use of fibre-reinforced polymers (FRPs) in many industries, understanding and successfully predicting the failure mechanisms of these materials is of the utmost importance. The lack of confidence in simpler criteria and the high computational costs of recent, more complete models motivated the development of a new damage progression model for pultruded FRP composites, which allows the simulation of the laminates as a homogeneous material. The present study focuses on the calibration and validation of the new model for 6 glass fibre-reinforced polymer (GFRP) materials from different suppliers. For this purpose the ABAQUS software package was used and all simulations were performed using a specific user-defined material subroutine (UMAT). The calibration was performed by adjusting the numerical curves to fit the experimental data available for different coupon tests. With all materials duly calibrated, several different application tests were simulated, and the numerical results were compared with experimental data. The calibration process was successful for all materials and coupon tests. The need to calibrate a mesh regularisation parameter with a compact tension test was also shown. For the application tests, the numerical simulations presented good agreement with the experimental data for all materials, being able to predict the failure loads, failure modes, and in some cases, even the post-failure behaviour. The results of this study show the feasibility of using the new damage progression model in structural design.

**Keywords:** Glass fibre-reinforced polymer (GFRP), Failure model, Damage progression, FE models, Numerical analysis.



# Contents

Declaration . . . . .	iii
Acknowledgments . . . . .	v
Resumo . . . . .	vii
Abstract . . . . .	ix
List of Tables . . . . .	xv
List of Figures . . . . .	xvii
Nomenclature . . . . .	xxi
List of Acronyms . . . . .	xxiv
<b>1 Introduction</b>	<b>1</b>
1.1 Motivation . . . . .	1
1.2 Topic overview . . . . .	1
1.3 Objectives and methodology . . . . .	2
1.4 Thesis outline . . . . .	3
<b>2 State of the art</b>	<b>4</b>
2.1 Composite Materials . . . . .	4
2.1.1 Classification of composites . . . . .	4
2.1.2 FRP composites . . . . .	5
2.1.3 Pultruded profiles . . . . .	6
2.1.4 Applications in aerospace industry . . . . .	7
2.2 Failure Analysis . . . . .	8
2.2.1 Composite Failure Mechanisms . . . . .	8
2.2.2 Lamina Failure Analysis . . . . .	9
2.2.3 Laminate Failure Analysis . . . . .	10
2.2.4 Failure Theories . . . . .	11
2.3 A new progressive failure model for pultruded FRPs . . . . .	13
<b>3 Experimental material characterisation and application tests</b>	<b>16</b>
3.1 Experimental mechanical characterisation . . . . .	16
3.1.1 Experimental programme and nomenclature . . . . .	17
3.1.2 Tensile tests . . . . .	18

3.1.3	Compression tests . . . . .	19
3.1.4	In-plane shear tests . . . . .	21
3.2	10° Off-axis tensile test . . . . .	23
3.2.1	Experimental procedure . . . . .	24
3.2.2	Data processing . . . . .	24
3.2.3	Results and discussion . . . . .	25
3.3	Application tests . . . . .	27
3.3.1	Experimental programme and nomenclature . . . . .	28
3.3.2	Compact tension tests . . . . .	28
3.3.3	Wide compact tension tests . . . . .	30
3.3.4	Compact compression tests . . . . .	31
3.3.5	Web-crippling tests . . . . .	32
3.3.6	Double-lap tests . . . . .	35
<b>4</b>	<b>Calibration of the model for new materials</b>	<b>38</b>
4.1	Description of FE models . . . . .	38
4.1.1	General considerations . . . . .	39
4.1.2	Tensile tests . . . . .	39
4.1.3	Compressive tests . . . . .	40
4.1.4	<i>Iosipescu</i> tests . . . . .	40
4.1.5	Compact tension tests . . . . .	40
4.2	Preliminary calibration study . . . . .	41
4.2.1	Calibration process . . . . .	41
4.2.2	Mesh sensitivity analysis . . . . .	42
4.2.3	Regularisation coefficients sensitivity analysis . . . . .	47
4.3	Results and discussion . . . . .	49
4.3.1	Longitudinal tensile tests . . . . .	49
4.3.2	Transverse tensile tests . . . . .	49
4.3.3	Longitudinal compressive tests . . . . .	51
4.3.4	Transverse compressive tests . . . . .	53
4.3.5	<i>Iosipescu</i> tests . . . . .	54
4.3.6	10° Off-axis tensile tests . . . . .	56
4.3.7	Compact tension tests . . . . .	58
<b>5</b>	<b>Application of the model</b>	<b>61</b>
5.1	Description of FE models . . . . .	61
5.1.1	Wide compact tension tests . . . . .	61
5.1.2	Compact compression tests . . . . .	62
5.1.3	Web-crippling tests . . . . .	63
5.1.4	Double-lap tests . . . . .	64



5.2	Mesh study . . . . .	65
5.2.1	Wide compact tension tests . . . . .	65
5.2.2	Compact compression tests . . . . .	66
5.2.3	Web-crippling tests . . . . .	66
5.2.4	Double-lap tests . . . . .	67
5.3	Results and discussion . . . . .	68
5.3.1	Wide compact tension tests . . . . .	68
5.3.2	Compact compression tests . . . . .	70
5.3.3	Web-crippling tests . . . . .	74
5.3.4	Double-lap tests . . . . .	76
<b>6</b>	<b>Conclusions and future developments</b>	<b>81</b>
6.1	Conclusions . . . . .	81
6.2	Future developments . . . . .	82
	<b>Bibliography</b>	<b>82</b>
<b>A</b>	<b>Additional background on the new progressive failure model</b>	<b>89</b>
<b>B</b>	<b>Summary of experimental results</b>	<b>90</b>
<b>C</b>	<b>Finite element models</b>	<b>93</b>
<b>D</b>	<b>Damage model input data</b>	<b>94</b>



# List of Tables

2.1	Main mechanical properties of different types of fibres. . . . .	5
2.2	Main mechanical properties of different types of thermoset resins. . . . .	6
3.1	Profile's geometry and dimensions studied. . . . .	18
3.2	Experimental programme and number of tested specimens for mechanical characterisation tests. . . . .	18
3.3	Average and co-variation of OAT and <i>Iosipescu</i> tests' main results for I150-AP-W. . . . .	27
3.4	Experimental programme available and number of tested specimens for application tests. . . . .	28
4.1	Main results of I200-FC-W (and I150-AP-W for OAT test) and relative difference to the experimental average for different meshes. . . . .	46
4.2	Longitudinal tensile tests - calibration inputs and summary of main results. . . . .	50
4.3	Transverse tensile tests - calibration inputs and summary of main results. . . . .	51
4.4	Longitudinal compressive tests - calibration inputs and summary of main results. . . . .	52
4.5	Transverse compressive tests - calibration inputs and summary of main results. . . . .	53
4.6	<i>Iosipescu</i> tests - calibration inputs and summary of main results. . . . .	55
4.7	10° Off-axis tensile tests - calibration inputs and summary of main results. . . . .	57
4.8	Compact tension tests - calibration input and summary of main results. . . . .	59
5.1	Main application tests' results of I200-FC (and I150-AP for DL test) and relative difference to the experimental average for different meshes. . . . .	68
5.2	Wide compact tension test - summary of main results. . . . .	69
5.3	Compact compression test - summary of main results. . . . .	73
5.4	Web-crippling test - summary of main results. . . . .	75
5.5	Double-lap test - different sets of in-plane shear calibration variables tested. . . . .	77
5.6	Double-lap test - maximum load results for different sets of properties. . . . .	79
B.1	Average and co-variation of all materials' mechanical properties. . . . .	90
B.2	Average and co-variation of CT, WCT, CC and WC test results. . . . .	91
B.3	Average and co-variation of DL results. . . . .	92
D.1	Input data for FE models: mechanical properties for all materials. . . . .	94
D.2	Input data for FE models: damage progression parameters for all materials. . . . .	95



# List of Figures

2.1	Types of composites based on shape of reinforcements: (a) particle composites; (b) short fibre composites; (c) flake composites; (d) laminated composites; (e) sandwich composites.	5
2.2	Schematic representation of the pultrusion process.	7
2.3	Evolution of structural mass percentage of composites in civil transportation aircraft.	8
2.4	Different types of composite failure mechanisms: (a) fibre failure (1, 2, 4), debonding (3) and matrix cracking (5); (b) microbuckling; (c) delamination.	9
2.5	Schematic representation of the parallel spring model.	11
2.6	Stress vs. strain relationship (for one directional case) with four stages: (i) undamaged; (ii) damaged progression; (iii) mesh regularisation; and; (iv) constant stress.	15
3.1	Different profiles studied: (a) I section; (b) U section; (c) S section.	17
3.2	Experimental setup of tensile test from I152-CP-W: (a) initial setup; (b) failure mode of a longitudinal specimen.	19
3.3	Representative stress vs. strain curves of experimental tensile tests: (a) longitudinal tension; (b) transverse tension.	20
3.4	Experimental setup of compressive tests: (a) initial setup for the CLC configuration; (b) failure mode of a transverse specimen for the CLC configuration; (c) failure of a S120-AP specimen in compression following ASTM D 695-02	21
3.5	Representative stress vs. strain curves of experimental compressive tests: (a) longitudinal compression; (b) transverse compression.	22
3.6	Experimental setup of a <i>losipescu</i> shear test for a longitudinal specimen from I150-ST-W: (a) initial setup; (b) failure mode.	22
3.7	Representative stress vs. strain curves of experimental in-plane shear tests: (a) <i>losipescu</i> tests; (b) 10° off-axis tensile tests.	23
3.8	Experimental specimens used in OAT test with different strain measurement systems: (a) strain gauges; (b) video-extensometry system.	24
3.9	10° off-axis tensile test: (a) experimental setup; (b) failure mode.	25
3.10	Schematic representation of a 10° off-axis tensile test specimen.	25
3.11	Experimental curves for all specimens of I150-AP-W: (a) stress vs. strain; (b) load vs. displacement.	27

3.12 Compact tension tests - experimental setup: (a) schematic setup and dimensions (in mm); (b) Crack Mouth Opening Displacement (CMOD) points. . . . .	29
3.13 Compact tension tests - experimental results: (a) representative load vs. Crack Mouth Opening Displacement (CMOD) curves; (b) delamination in a I152-CP specimen. . . . .	30
3.14 Wide compact tension tests - experimental schematic setup and dimensions (in mm). . .	31
3.15 Wide compact tension tests - experimental results: (a) representative load vs. Crack Mouth Opening Displacement (CMOD) curves; (b) crack propagation (typical failure mode). 31	
3.16 Compact compression tests - experimental setup: (a) schematic setup and dimensions (in mm); (b) Crack Mouth Closing Displacement (CMCD) points. . . . .	32
3.17 Compact compression tests - experimental results: (a) representative load vs. Crack Mouth Closing Displacement (CMCD) curves; (b) tensile failure mode on the opposite side to the notch. . . . .	33
3.18 Web-crippling tests - schematic configurations of: (a) Internal Two Flanges; (b) External Two Flanges. . . . .	33
3.19 Web-crippling tests - location of the points used to measure the displacements in both configurations: (a) Internal Two Flanges (ITF); (b) External Two Flanges (ETF). . . . .	34
3.20 Web-crippling tests - representative load vs. displacement curves from experimental re- sults for: (a) ITF-100 configuration; (b) ETF-15 and ETF-100 configurations. . . . .	35
3.21 Web-crippling tests - main failure modes registered in experimental tests: (a) web-crushing (U150-ST-ITF); (b) web-buckling (I152-CP-ETF). . . . .	35
3.22 Double-lap tests - experimental setup: (a) schematic GFRP plate dimensions (in mm); (b) schematic setup; (c) experimental setup. . . . .	36
3.23 Double-lap tests - failure modes of I150-AP specimens for all configurations. . . . .	37
3.24 Double-lap tests - Representative load vs. displacement curves from experimental results: (a) Shear-out failure mode; (b) shear-out and bearing failure modes. . . . .	37
4.1 Mesh detail view near the weak region with different mesh sizes for a tensile test. . . . .	43
4.2 Different mesh sizes for a <i>losipescu</i> test: (a) 2 mm mesh; (b) 1 mm mesh; (c) 0.5 mm mesh. 43	
4.3 Different mesh sizes for a compact tension test: (a) general model overview; (b) mesh detail view. . . . .	43
4.4 Experimental and numerical results of load vs. displacement curves of tensile tests for the I200-FC-W material with different mesh sizes: (a) longitudinal tension; (b) transverse tension. . . . .	44
4.5 Experimental and numerical results of load vs. displacement curves of compressive tests for the I200-FC-W material with different mesh sizes: (a) longitudinal compression; (b) transverse compression. . . . .	44
4.6 Experimental vs. numerical curves of in-plane shear tests with different mesh sizes: (a) stress vs. strain curve for I200-FC-W <i>losipescu</i> test; (b) load vs. displacement curve for I150-AP-W OAT test. . . . .	45

4.7	Experimental vs. numerical curves of compact tension tests with different mesh sizes. . .	45
4.8	Sensitivity analysis of regularisation factors for I200-FC-W-LT test: (a) varying $\alpha$ with fixed $\eta_i = 1 \times 10^{-5}$ ; (b) varying $\eta_i$ with fixed $\alpha = 15$ mm. . . . .	47
4.9	Sensitivity analysis of regularisation factors for I200-FC-W-CT-30 test: (a) varying $\alpha$ with fixed $\eta_i = 1 \times 10^{-5}$ ; (b) varying $\eta_i$ with fixed $\alpha = 30$ mm. . . . .	48
4.10	Longitudinal tensile tests - experimental and numerical results for web plates: (a) stress vs. strain curves; (b) load vs. displacement curves. . . . .	50
4.11	Transverse tensile tests - experimental and numerical results for web plates: (a) stress vs. strain curves; (b) load vs. displacement curves. . . . .	51
4.12	Longitudinal compressive tests - experimental and numerical results for web plates: (a) stress vs. strain curves; (b) load vs. displacement curves. . . . .	52
4.13	Transverse compressive tests - experimental and numerical results for web plates: (a) stress vs. strain curves; (b) load vs. displacement curves. . . . .	53
4.14	<i>Iosipescu</i> tests - stress vs. strain curves of experimental and numerical results: (a) web plates; (b) flange plates. . . . .	55
4.15	Failure of a numerical <i>Iosipescu</i> test and degradation of main variables - $G_{12}$ (SDV7) and $E_{22}$ (SDV5) in Pa for: (a) I200-FC-W; (b) U150-ST-W. . . . .	56
4.16	10° Off-axis tensile tests - experimental vs. numerical results for web plate: (a) stress vs. strain curves; (b) load vs. displacement curves. . . . .	57
4.17	Failure progression of a numerical 10° off-axis tensile test and degradation of $G_{12}$ (SDV7) in Pa. . . . .	58
4.18	Compact tension tests - experimental and numerical load vs. CMOD results for web plate: (a) notch length of 30 mm; (b) notch length of 35 mm. . . . .	59
4.19	Compact tension tests - detailed view of failure progression and variable degradation of a numerical simulation for I200-FC-CT-35: (a) $E_{22}$ (SDV5) in Pa; (b) $\sigma_{22}$ (S22) in Pa. . . . .	60
4.20	Compact tension tests - detailed view of failure progression and variable degradation of a numerical simulation for I152-CP-CT-35: (a) $E_{22}$ (SDV5) in Pa; (b) $\sigma_{22}$ (S22) in Pa; (c) out-of-plane displacements (U3) in mm. . . . .	60
5.1	Wide compact tension test - main characteristics of a numerical model for I200-FC-WCT-30: (a) Boundary conditions and general mesh overview; (b) mesh refinement detailed view. . . . .	62
5.2	Compact compression test - main characteristics of a numerical model for I200-FC-CC-40: (a) Boundary conditions and general mesh overview; (b) mesh refinement detailed view. . . . .	63
5.3	Web-crippling test - main characteristics of a complete numerical model for I152-FC-WC-ITF-100: (a) Boundary conditions and general mesh overview; (b) mesh refinement detailed view. . . . .	64

5.4	Double-lap test - main characteristics of a DL-35 numerical model for: (a) Boundary conditions and general mesh overview; (b) mesh refinement detailed view. . . . .	65
5.5	Experimental and numerical results of load vs. displacement curves of application tests with different mesh sizes: (a) I200-FC-WCT-30; (b) I200-FC-CC-40. . . . .	66
5.6	Experimental and numerical results of load vs. displacement curves of application tests with different mesh sizes: (a) I200-FC-WC-ITF-100; (b) I150-AP-DL-15. . . . .	67
5.7	Wide compact tension test - experimental and numerical load vs. displacement curves for: (a) 30 mm notch length; (b) 40 mm notch length. . . . .	69
5.8	Wide compact tension test - failure progression and variable degradation of a numerical simulation for I150-ST-WCT-30: (a) $E_{22}$ (SDV5) in Pa; (b) $\sigma_{22}$ (S22) in Pa. . . . .	70
5.9	Compact compression test - experimental and numerical load vs. displacement curves for: (a) I200-FC and I150-ST (b) I152-CP and U150-ST. . . . .	71
5.10	Compact compression test - $r_{22}^-$ parametric study for I200-FC with compressive elastic modulus $E_{22}^-$ as input. . . . .	73
5.11	Compact compression test - notch and application holes' failure of a numerical simulation for I200-FC-CC-40- $E_{22}^-$ - $r_{22}^-$ =0.4: (a) $E_{22}$ (SDV5) in Pa; (b) $\sigma_{22}$ (S22) in Pa units. . . . .	73
5.12	Compact compression test - tensile failure of: (a) a numerical simulation for I200-FC-CC-40- $E_{22}^-$ - $r_{22}^-$ =0.4; (b) an experimental specimen. . . . .	74
5.13	Web-crippling test - experimental and numerical load vs. displacement curves for: (a) ITF-100 configuration (b) ETF-15 (I200-FC and I150-ST) and ETF-100 (I152-CP and U150-ST) configurations. . . . .	75
5.14	Web-crippling test - web-crushing failure of an I200-FC numerical model for different configurations: (a) ITF-100; (b) ETF-15. . . . .	76
5.15	Web-crippling test - buckling and mixed failure of an I152-CP numerical model for different configurations: (a) ITF-100 (with a scale factor of 3); (b) ETF-100. . . . .	76
5.16	Double-lap test - experimental and numerical load vs. displacement curves with different calibration parameters for: (a) DL-15 configuration for I150-AP (b) DL-70 configuration for I150-AP and S120-AP. . . . .	78
5.17	Web-crippling test - failure of an I152-CP numerical model for different configurations: (a) ITF-100 (with a scale factor of 3); (b) ETF-100. . . . .	79
5.18	Double-lap test - numerical failure and shear modulus degradation (SDV7) of I150-AP-DL-15 for different sets of properties: (a) OAT; (b) IS-vOAT. . . . .	80
5.19	Double-lap test - numerical failure shear modulus degradation (SDV7) of I150-AP-DL-70 for different sets of properties: (a) OAT; (b) IS-vOAT. . . . .	80
C.1	Boundary conditions' model view for different tests: (a) tensile test; (b) compressive test. .	93
C.2	Boundary conditions' model view for different tests: (a) <i>losipescu</i> test; (b) compact tension test. . . . .	93



# Nomenclature

## Greek Symbols

$\alpha$	Mesh regularisation.
$\gamma$	Shear strain.
$\Delta$	Relative difference.
$\epsilon$	Normal strain.
$\eta$	Viscous regularisation.
$\theta$	Fibre orientation.
$\nu$	Poisson coefficient.
$\sigma$	Normal stresses.
$\tau$	Shear stresses.

## Roman Symbols

$D$	Damage.
$d$	Maximum damage input.
$E$	Elastic modulus.
$F$	Failure function.
$f$	Failure index.
$G$	Shear modulus.
$m$	Exponential evolution input.
$r$	Residual strength.
$S$	Ultimate stress.

## Subscripts

11	Longitudinal direction.
----	-------------------------

12	Plane 12.
13	Plane 13.
22	Transverse direction.
23	Plane 23.
33	Thickness direction.
$i, j, k$	Computational indexes.
$op$	Out-of-plane.
$pl$	In-plane.
$r$	Residual.
$u$	Ultimate.
$x, y, z$	Cartesian components.

### **Superscripts**

+	Tension.
-	Compression.

# List of Acronyms

**AFRP** Aramid Fibre-Reinforced Polymer

**ASTM** American Society for Testing and Materials

**C/C** Carbon/Carbon Composite

**CC** Compact Compression

**CFRP** Carbon Fibre-Reinforced Polymer

**CLC** Combined Loading Compression

**CMC** Ceramic Matrix Composite

**CMCD** Crack Mouth Closing Displacement

**CMOD** Crack Mouth Opening Displacement

**CT** Compact Tension

**DL** Double-Lap

**ETF** External Two Flanges

**FE** Finite Element

**FEA** Finite Element Analysis

**FRC** Fibre-Reinforced Composite

**FRP** Fibre-Reinforced Polymer

**GFRP** Glass Fibre-Reinforced Polymer

**IS** In-plane Shear

**ISO** International Organization for Standardization

**ITF** Internal Two Flanges

**LC** Longitudinal Compressive

**LT** Longitudinal Tensile

**MMC** Metal Matrix Composite

**OAT** Off-Axis Tensile

**PMC** Polymer Matrix Composite

**TC** Transverse Compressive

**TT** Transverse Tensile

**UMAT** User-Defined Material Subroutine

**WC** Web-Crippling

**WCT** Wide Compact Tension

**WWFE** World-Wide Failure Exercise

# Chapter 1

## Introduction

### 1.1 Motivation

With the increasing usage of composite materials in many industries such as automotive, aerospace and construction [1], understanding and successfully predicting failure of these materials is of the utmost importance. As pointed out in World-Wide Failure Exercise (WWFE) [2] in the beginning of the 20<sup>th</sup> century, there was a lack of confidence in the failure criteria used for Fibre-Reinforced Polymers (FRPs) at the time. A research showed that around 90% of designers used simple criteria as the maximum stress and maximum strain theories, or quadratic polynomial criteria [2]. Gonilha *et al.* [3] recently stated that failure initiation models such as Tsai-Hill [4] and Hashin [5] are still widely used, even when the materials in question do not comply with all theoretical conditions used to develop these models. For example, Hashin's theory [5] was developed for unidirectional FRP composites, thus not accounting for the non-transverse isotropy of pultruded FRPs [3]. More importantly, the use of these criteria alone leads to the underestimation of the composites' strength, highlighting that damage propagation needs to be taken into account [6–9].

Even though several other theories were developed [10–15], the high computational costs in numerical applications and the required (and difficult-to-obtain) damage parameters motivated the development of a novel progressive failure model for quasi-orthotropic pultruded FRP structures [3, 16]. The present study was driven by the need to validate that damage progression model in order to predict with greater confidence the failure mechanisms of FRP materials when subjected to any given actions.

### 1.2 Topic overview

Composite materials are the combination of two or more materials on a macroscopic scale into a new material, where the properties of the final composite material are naturally a combination of the constituent materials [1, 17, 18]. Fibre-Reinforced Polymers (FRPs) are a type of composite in which two distinct constituents are present. The fibres, which are mainly responsible for the structural function of the composite, provide high stiffness and strength to the material, and the polymeric matrix, which

provides the shape of the composite, holding the fibres in position and allowing for the load transfer between them [1]. Most commonly used FRPs include Carbon Fibre-Reinforced Polymers (CFRPs) and Glass Fibre-Reinforced Polymers (GFRPs).

Both these materials are used in a wide variety of industries, including aerospace, automotive, construction, and others. Pultruded GFRPs, due to their higher strength-to-weight ratio and resistance to corrosion than traditional metals, and associated with low production cost, are mainly used in civil engineering applications. In the aerospace field, where high performance is very important, CFRPs are more extensively used. Nevertheless, in smaller applications where a compromise between cost-effectiveness and performance may be reached, GFRP parts are still used.

With the increasing use of FRP materials across all industries, there is also a need to comprehend and predict their failure mechanisms. This failure can occur on the lamina constituents - the fibres and the matrix (or even in the interface between them) - or between laminae, *i.e.* delamination. To study the failure of FRPs, several theories were developed in the last century. First, non-interactive failure theories such as the Maximum Stress and Maximum Strain criteria were developed [19]. Then, understanding that the interaction between stresses played an important role in failure, other theories (interactive failure theories) were developed, with Tsai-Hill [4] and Tsai-Wu [20] theories as main examples. Finally, considering these stress interactions but also developing different criteria for each distinct failure mechanism, failure mode theories such as Hashin [5] and Puck and Schürmann [11] were developed. Recently, more complex theories have been developed considering also the progressive nature of laminae failure and adding the delamination effects.

### 1.3 Objectives and methodology

This study focuses on the calibration and validation of a new progressive failure model for quasi-orthotropic pultruded FRP materials. The main objective is to understand if the use of this failure model in numerical simulations is able to correctly predict the experimental behaviour by comparing numerical and experimental: (i) load/stress vs. displacement/strain curves; (ii) maximum load and stiffness results; and (iii) damage propagation and failure modes. Additionally, as a consequence of this process, the secondary objective is to expand the library of calibrated materials and the experimental application tests for which it has been tested.

For this purpose, the ABAQUS FEA software package [21] was used, and all simulations were performed using the User-Defined Material Subroutine (UMAT) developed by Gonilha *et al.* [3]. For the material calibration, the mechanical properties were retrieved from coupon tests or the literature [22–24], and the necessary calibration inputs for the novel failure model were computed by resorting to a trial and error curve-fitting process. With all materials duly calibrated, several different application tests (with non-uniform stress states) were simulated and the numerical results were compared with experimental data.

## 1.4 Thesis outline

This thesis is organised in 6 chapters. In the current chapter (Chapter 1), the motivation for this study is presented, followed by a succinct overview of composites and their failure mechanisms and theories. The objectives and methodology of this dissertation are then presented, followed by the presentation of the document's organisation.

Chapter 2 focuses on the state of the art. Firstly, a brief introduction to composite materials is made. Secondly, a failure analysis on FRP materials is done, presenting several failure mechanisms and summarising the main failure theories and criteria developed in the last century. Lastly, the novel progressive failure model used in this dissertation is addressed.

Chapter 3 presents all the experimental data used to develop this study, including mechanical characterisation tests and application tests, with special emphasis on the  $10^\circ$  off-axis tensile tests performed by the author.

Chapter 4 addresses the model calibration process for new materials, presenting the FE models used, mesh studies for every different test and the final results of the calibrated materials.

Chapter 5 focuses on the numerical simulation of the application tests, including FE models, a brief mesh study and results for all materials.

In Chapter 6, the conclusions are presented, some remarks regarding the progressive failure model are made, and suggestions for future developments are proposed.

# Chapter 2

## State of the art

Composite materials have existed for centuries. For example, Egyptian civilisations fabricated straw-reinforced mud bricks for construction and Japanese samurai used laminated metals to make swords. In the past century, composites started to be commercially produced and their study has enable remarkable progression and optimisation [1].

In this chapter, an introduction to composite materials and their classification is made, followed by an emphasis in FRP composites and their constituents. Some manufacturing techniques are then presented, with more focus on the pultrusion process. The use of FRPs in the aerospace applications is also mentioned. Section 2.2 presents an overview on the failure analysis of FRP composites. The composite failure mechanisms are addressed first, followed by the different lamina and laminate failure analysis approaches, and an overview on the history of failure theories and their most notable achievements. Finally, the last section addresses the new progressive failure model used in this dissertation, with the presentation of its main theoretical principles, limitations, failure initiation and damage propagation equations.

### 2.1 Composite Materials

#### 2.1.1 Classification of composites

In general, materials can be divided into four different categories: metals, ceramics, polymers, and composites. Composite materials are the combination of two or more materials on a macroscopic scale into a new material, where the properties of the final composite material are naturally a combination of the constituent materials [1, 17, 18]. This generally results in a new heterogeneous and anisotropic material [17], where, in the case of Fibre-Reinforced Composites (FRCs), two main features are commonly present - the fibres and the matrix. The fibres' main function is to provide the best mechanical properties (stiffness and strength) in the directions that are most important when creating the composite, while the matrix acts as a glue between the fibres and allows for a continuous material, while also increasing the material's strength in the directions perpendicular to the fibre.

Composite materials can be classified in various ways. One way is to define the type of composite



by the matrix material - Polymer Matrix Composites (PMCs), Metal Matrix Composites (MMCs), Ceramic Matrix Composites (CMCs) and Carbon/Carbon Composites (C/Cs) [17]. Additionally, given the different geometry and size of the reinforcements, other classifications are possible - phased composites and layered composites [17]. Phased composites can have particulate reinforcements, short fibres, unidirectional fibres or flake reinforcements, while layered composites may be laminated or sandwich composites (Figure 2.1).

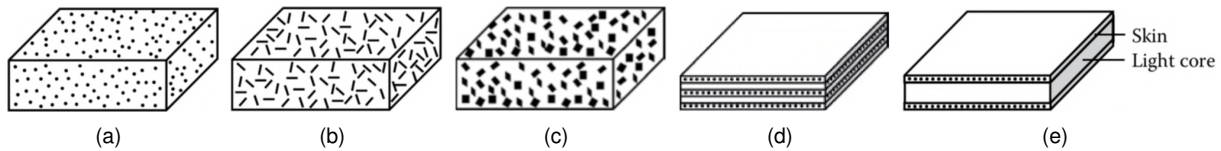


**Figure 2.1:** Types of composites based on shape of reinforcements: (a) particle composites; (b) short fibre composites; (c) flake composites; (d) laminated composites; (e) sandwich composites. Adapted from [1]

## 2.1.2 FRP composites

Fibre-Reinforced Polymers (FRPs), as the name suggests, are composites of polymeric matrix and fibre reinforcements, where the latter is responsible for the main strength properties of the composite. The main materials used for the fibres are: (i) carbon, (ii) glass, or (iii) aramid (kevlar). Carbon fibres have high elasticity modulus compared to the others and are used in high-performance industries such as aerospace and defence sectors [1]. Glass fibres, although also used in the aerospace sector, are more widely used in the construction field, as they present a better production price vs. strength ratio, and can be divided into various types according to their main features (A, C, E, AE, and S). For example, E-glass (electrical glass) is widely used due to its electric insulation properties, while S-glass (structural glass) is known for its mechanical properties. Aramid fibres present very high tenacity and toughness, which are useful properties where energy absorption is required, such as bulletproof vests or crash attenuators [25]. Table 2.1 shows typical mechanical properties of these fibres.

Type of fibre	Tensile strength [MPa]	Tensile modulus [GPa]	Ultimate strain [%]	Density [kg/m <sup>3</sup> ]
Carbon	3650–7000	207–600	2.5-4.5	1700–1800
Glass (E)	2500–4800	70–81	0.6-1.5	2540–2570
Aramid	2900–3400	70–152	2.0-4.0	1390–1467

**Table 2.1:** Main mechanical properties of different types of fibres [25, 26].

As for the polymeric matrices, two main groups can be defined: (i) thermoplastic resins (polypropylene, polyphenylene sulfone, polyamide), and (ii) thermoset resins (polyesters, vinyl esters, phenolics, melamines, silicones, polyurethanes, epoxies) [17]. Both types of resin undergo a high-temperature process in their fabrication, but while this process in thermosets is irreversible (once cooled, they have low thermal resistance), thermoplastics can be remelted and reshaped. However, although thermoplastics have higher fracture toughness, their increased production cost leads to a higher use of thermosets in

structural composite applications [27], such as pultruded profiles. Table 2.2 presents the main properties of the most commonly used thermosets.

Type of resin	Tensile strength [MPa]	Tensile modulus [GPa]	Ultimate strain [%]	Density [kg/m <sup>3</sup> ]
Epoxy	55–130	2.5–4.1	1-8	1100–1300
Polyester	20–100	1.8–4.1	1-5	1000–1450
Vinyl ester	70–87	3.0–5.1	3-4	1100–1300

**Table 2.2:** Main mechanical properties of different types of thermoset resins [25, 26].

The FRPs that result from the combination of the fibres and resins presented are divided into multiple categories, such as Carbon Fibre-Reinforced Polymer (CFRP), Glass Fibre-Reinforced Polymer (GFRP) and Aramid Fibre-Reinforced Polymer (AFRP). CFRP and GFRP are by far the most utilised across all industries [17] when compared to AFRP.

All FRPs have high tensile strength and stiffness and high specific strength and specific modulus (ratio between strength or modulus and the density), with CFRP being superior over GFRP in these aspects. These are considerable advantages when compared to metals, hence their growing use in industries that require efficient and light-weight components and structures. Nevertheless, FRP composites are generally weaker in the transverse direction as they are optimised for certain load scenarios. To improve this, instead of having only longitudinal fibres (usually supplied by rovings), other fibre architectures that reinforce the transverse direction are also used, such as woven fabrics and unwoven mats [28]. Moreover, another crucial advantage of FRPs over metal materials is their resistance to corrosion.

### 2.1.3 Pultruded profiles

There are several methods of fabricating FRP composites, with some examples being: wet lay-up, prepreg lay-up (both open mould processes), compression moulding (closed mould process), filament winding, tape winding (both continuous moulding processes), and others [1, 17, 25]. Since only pultruded FRPs are studied in this dissertation, the pultrusion process is the only one addressed.

Pultrusion is an automated and continuous process (continuous moulding process) used to produce FRP parts from raw materials [25]. This process is widely used in the mass production of FRP composites, specially GFRP for the construction industry due to its increased cost-effectiveness when compared to other production methods. Various profile sections can be obtained through pultrusion - open sections, closed sections, and even multicellular sections - however, the profile shape has to be constant along the length, and curved shapes (along the length) cannot be obtained in traditional pultrusion processes.

In a typical pultrusion process, dry fibres in various forms (rovings, fabrics and mat fibres) are supplied from rolls or spools and guided with the desired shape through a thermoset resin bath. In a second stage, the material is cured in a heated die, getting its final shape. In the last stage, the profile is pulled (hence the name pultrusion), and cut to its final length with a saw. Figure 2.2 exemplifies a general pultrusion line.

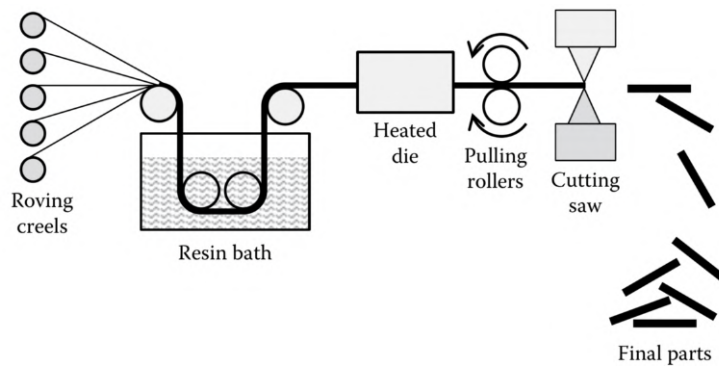


**Figure 2.2:** Schematic representation of the pultrusion process. Source: [1].

Most commonly, pultruded materials are obtained from fibre rovings, resulting in unidirectional fibres along the length of the profile. This enhances the mechanical properties in the longitudinal direction while compromising the strength in the transverse direction. For this reason, some profiles combine fibre mats and fabrics, which, due to their multi-directional fibre alignment, enhance the final pultruded profile strength in the transverse direction.

#### 2.1.4 Applications in aerospace industry

FRP composites have multiple applications in a different variety of fields. In civil engineering structures, GFRP with polyester, vinyl ester and epoxy are used for modular houses, and bridges [1]. GFRPs are also used in the marine and automotive fields, but high-performance structures are usually fabricated with CFRP, including most applications in the aerospace industry. Nevertheless, some examples of GFRP composites use in the aerospace sector include lighter aircraft's propeller blades, drones, and helicopter rotor blades and rotor hubs [17].

The first FRP composite parts in aircraft were made with glass fibre, and were used mostly for small applications where insulation was needed. Then, in the early 60s structural parts fabricated with boron/epoxy composite were used, although exclusively for military aircraft. An example is the F-14 aircraft, where the skins of the horizontal stabilizer were made of boron/epoxy composites [1]. Shortly after, the breakthrough of CFRP started, with uses in both military and commercial aviation. The first features made of CFRP were the engine rotor blades, with exterior surfaces such as flaps and stabilizers following.

As depicted in Figure 2.3, the use of composite in commercial aviation has increased a lot since their breakthrough. While in the 80s, the mass of composite structures accounted for around 10% or less of the structural weight of aircrafts, most recent examples show that this ratio is already around 50% or more. In the Airbus A380, which has 25% of its structural mass in composite materials, one of the main innovations was the use of CFRP (with epoxy resin) in the centre wing box that connects the wing to the fuselage, with 50% of its weight composed of this carbon/epoxy composite [17]. More recently, the Boeing 787 and the Airbus A350 have around 50% of their structural mass made from composite materials. Additionally to the centre wing box, the entire wings and most of the fuselage are fabricated with CFRP stiffened panels [17].

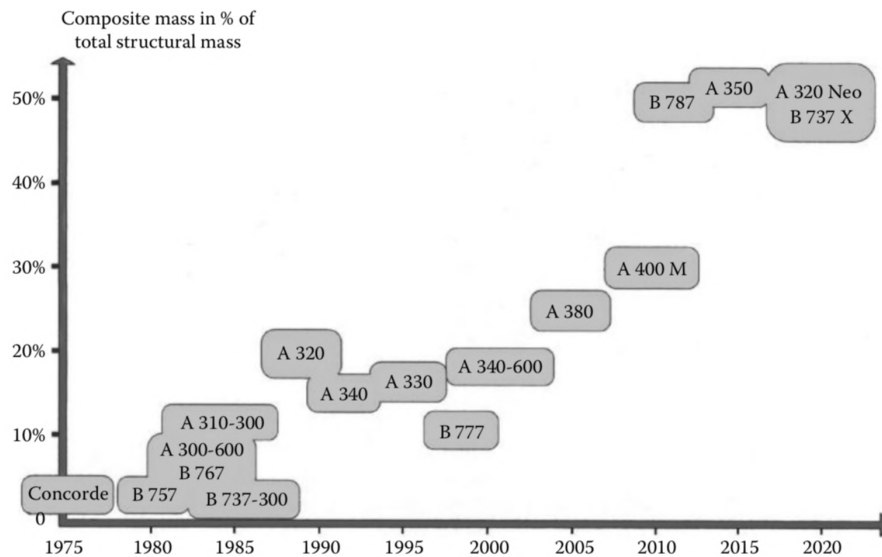


**Figure 2.3:** Evolution of structural mass percentage of composites in civil transportation aircraft.  
Source: [17].

## 2.2 Failure Analysis

### 2.2.1 Composite Failure Mechanisms

Due to their main characteristics - heterogeneity and anisotropy (or orthotropy) - FRP composite materials exhibit more intricate failure mechanisms than traditional materials, such as metals. Some of these failure mechanisms are illustrated in Figure 2.4 and can be divided into two major categories: (i) intra-ply failure - failure that occurs in fibre, matrix or in the interface between them, and (ii) inter-ply failure - failure that occurs between plies, that is, delamination.

Mechanisms 1 and 2 of Figure 2.4 (a) are called fibre pull-out and fibre bridging, respectively. Even though both are tensile failure mechanisms, the former occurs when the fibre-matrix interface is weak, otherwise, the latter is more likely to take place [29]. Both these failures are preceded by another failure mechanism - debonding (mechanism 3 of Figure 2.4 (a)) - which occurs when there is a loss of adhesion between the two surfaces (fibre and matrix). Another and more common failure mechanism regarding fibre tensile modes is fibre fracture (mechanism 4 of Figure 2.4 (a)), which takes place when the maximum strength of the fibre is surpassed.

Fibre splitting and fibre kinking are two other relevant failure mechanisms, but these are related to compression stresses. Splitting is usually associated with combined compressive and in-plane shear stresses and is the most common of these two failure modes. On the other hand, fibre kinking is generally associated with higher compressive stresses, and it is more likely to happen when there are misaligned fibres in relation to the principal stresses orientation [30]. Another failure similar to kinking called microbuckling may occur, as depicted in Figure 2.4 (b).

Concerning matrix failure modes, they usually occur due to transverse stresses. Puck and Schürmann [11] differentiated three phenomena - matrix cracking due to tensile stresses and two types of matrix cracking due to compressive stresses depending on the relevance of shear stresses induced.

When shear stresses are dominant and associated with a compressive state, the fracture plane is usually perpendicular to the applied load, otherwise, the cracking plane will be inclined. Even though these are the most recurrent phenomena, longitudinal loads can also induce matrix cracks between fibres (mechanism 5 of Figure 2.4 (a)). These type of cracks are characteristic of brittle polymeric matrices [29].

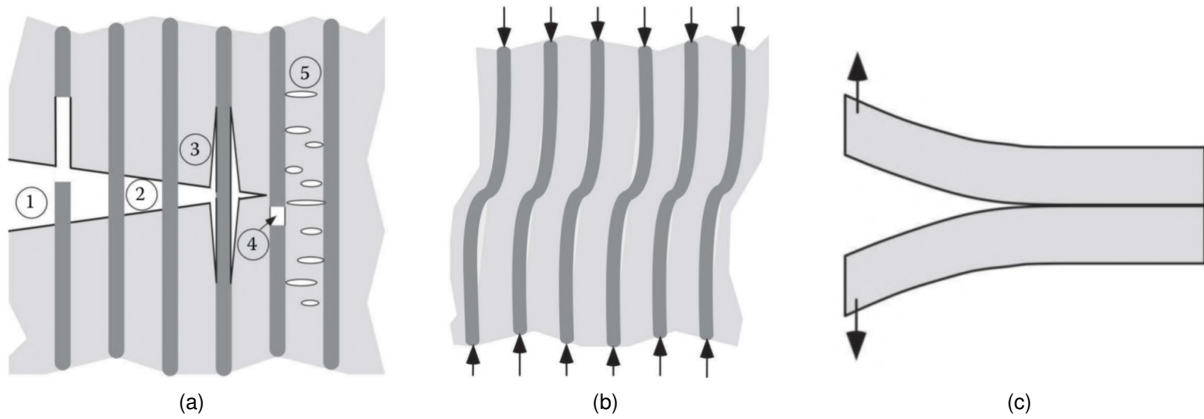


**Figure 2.4:** Different types of composite failure mechanisms: (a) fibre failure (1, 2, 4), debonding (3) and matrix cracking (5); (b) microbuckling; (c) delamination. Adapted from [31].

The delamination process illustrated in figure 2.4 (c) is the only inter-ply failure mechanism, although different stress states can lead to this process. As the name suggests, it consists of the separation of layers of a laminated structure, resulting in a reduction of mechanical properties due to the loss of composite behaviour. Inter-ply failure usually occurs after some form of intra-ply failure has taken place [29]. In a unidirectional fibre composite, this mechanism is more likely to occur when the laminate is subjected to bending or compressive stresses along the principal stress direction, resulting in high shear stresses between laminae [29]. In the case of laminates with different fibre orientations in each lamina, the delamination risk increases because the interface between laminae with different fibre orientations possesses weaker interface strength [32].

## 2.2.2 Lamina Failure Analysis

With the increased use of composite materials in the industry, there is also a need to understand and predict their behaviour when subjected to different types of applied stresses. During the last century, several researchers in the field started developing failure theories and criteria.

Until 1970, theories were based on a stress field failure envelope concept, that is, when a lamina was subjected to a stress field that was outside of this failure envelope, it would have been predicted to fail. These envelopes could assume various shapes, depending on the authors' assumptions. This methodology is an empirical form of trying to fit experimental data obtained from various types of tests with mathematical formulations [19].

In earlier attempts, these criteria did not incorporate interaction between stresses nor strains (for example, failure in the longitudinal direction was assumed to be independent of transverse stresses),

therefore, they are classified as (i) Noninteractive or Limit Failure Theories. The best examples of such theories are the Maximum Stress and Maximum Strain criteria [19].

As more experiments were made, it became obvious that such theories could not accurately predict failure under combined stress states and that stress interaction did actually played a role in failure. Many more criteria were then developed in what can be classified as (ii) Interactive Failure Theories. Most of these were based on mathematical approaches and usually considered quadratic interaction between stresses, resulting in ellipsoid-like failure envelopes in stress planes. Two famous criteria that can be classified as such are the Tsai-Hill [4] and Tsai-Wu [20] criteria.

Even though interactive failure theories presented good data-fitting curves, the lack of physical meaning in some theories and the difficulty of determining many necessary constants to recreate failure envelopes lead researchers to try a phenomenological approach, that is, conceive criteria that can predict and distinguish the different failure modes [19]. These types of theories are classified as (iii) Failure Mode Theories, with Hashin [5] and Puck and Schürmann [11] as two examples.

### 2.2.3 Laminate Failure Analysis

The different categories of failure theories presented above are all related to lamina failure. To study the entire laminate failure, one common approach is to use the Ply-by-Ply Discount Method [33].

This method consists of considering each lamina as a homogeneous material, applying a selected lamina failure criterion to each ply, and according to the evolution of stresses and strains calculated with laminated plate theory, determine which plies will fail. Stiffness reduction models are then applied to account for the stiffness loss of the whole laminate due to ply failures. The stresses and strains are then again analysed accounting with this reduction of stiffness and the whole process is done cyclically until ultimate failure is achieved [33].

Ultimate failure "per si" can too have different meanings. Depending on project requirements, first ply failure can be considered an ultimate failure, in which case the process described above is not necessary. This concept is more used in fibre dominated composites, where matrix cracking may be negligible and sudden fibre fracture is more common. In a less conservative approach, ultimate failure can be considered when the last ply fails.

Concerning the stiffness reduction of a laminate, Sun *et al.* [33] highlighted two ways of treating this phenomenon. The first one is called Parallel Spring Model, in which each lamina is modelled as a pair of springs, one representing fibre (longitudinal failure mode) and the other representing the matrix (transverse and shear failure modes). This representation is based on a phenomenological point of view. The laminate is then represented by the parallel assembly of springs, as seen in Figure 2.5. Then according to the failure that occurs in the lamina, properties related to that failure are usually set to zero (per example, if fibre failure occurs,  $E_1$  is reduced and  $E_2$  and  $G_{12}$  remain intact), taking a total discount method approach. They can also be set to other residual values or even considered as an exponential decay, which is called a partial discount method [19].

In addition to the methods presented, it is also important to complement laminate failure with the

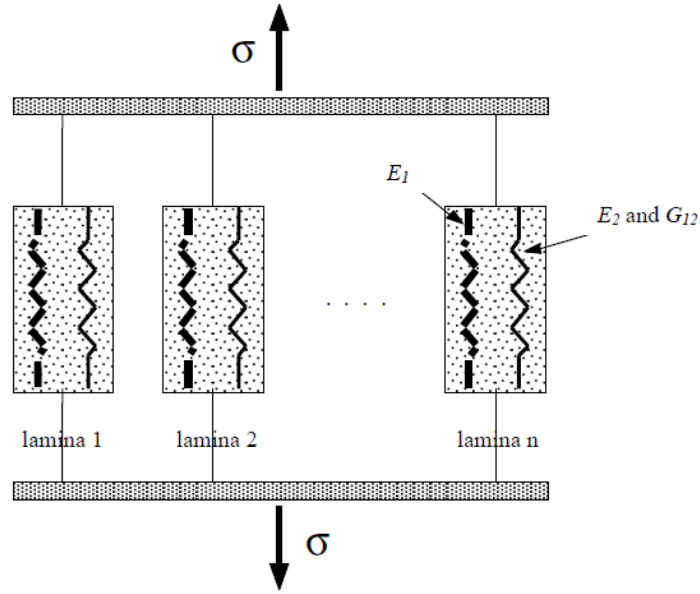


**Figure 2.5:** Schematic representation of the parallel spring model [33].

study of delamination, which is one of the predominant failure in laminated composites [19]. To predict delamination failure, a common approach is to start by predicting initial damage using stress-based criteria, and then using fracture mechanics to study the damage propagation [19].

## 2.2.4 Failure Theories

The most relevant failure theories for isotropic ductile materials were developed in the beginning of the 20<sup>th</sup> century. Tresca developed his criterion stating that yielding would only occur when maximum shear stress equals the shear stress at yielding in an uniaxial test, correctly neglecting the effect of hydrostatic stresses. Most famously, the Von-Mises theory was based on the principle of maximum distortion energy instead of shear stresses. Both these theories are valid and their failure envelopes present good correlation with experimental data, with the first being more conservative than the latter. Later, Mohr-Coulomb theory developed a criterion that recognized different tensile and compressive strengths of materials [34].

However, these criteria are valid only for isotropic materials. With the increased use of composites across several industries, the necessity of establishing criteria that could successfully predict failure in orthotropic or even anisotropic materials also increased.

The first failure criteria developed for composite materials were the Maximum Stress and Maximum Strain criteria. For each lamina, a stress-strain analysis in the local coordinate system is employed, and one is considered to fail if the stress (or strain) in one principal direction is higher than the maximum stress (or strain) allowed in that same direction. Even though these criteria may be used in some uniaxial stress cases, not considering the interaction between principal stresses is a rough approximation. Moreover, the maximum strain has an advantage relatively to the maximum stress theory because it accounts for the Poisson ratio effect [33].

In 1950, Hill extended the Von-Mises formulation for anisotropic materials assuming a quadratic

stress approximation. This criterion includes several parameters characteristic of the state of anisotropy [35]. In the next decade, Tsai simplified Hill's theory for orthotropic materials, in what we know today as the Tsai-Hill failure criteria [4]. Considering material orthotropy, a plane stress state and resorting to theoretical uniaxial tests, Tsai determined the previous formulation constants as functions of the material's strength, leading to a two-dimensional failure envelope depending on longitudinal, transverse, and shear stresses ( $\sigma_{11}$ ,  $\sigma_{22}$ , and  $\tau_{12}$ , respectively). Even though he reached a single equation envelope, different material strength constants have to be used in different quadrants (*i.e.* compressive strength if  $\sigma_{11}$  or  $\sigma_{22}$  are negative and tensile strength if positive).

Recognizing this limitation, Hoffman [36] altered the Tsai-Hill criterion to include both tensile and compressive properties resulting in a single equation with no quadrant-dependent variables. Nonetheless, this incorporation proposes that the compressive strength of a material influences the failure in pure tension, which is understood to be physically unacceptable [5].

In 1971, Tsai and Wu [20] followed a more generic approach like Hill. They proposed a model based on mathematical tensors  $F_i$  and  $F_{ij}$  and a quadratic stress approximation (*i.e.* neglecting cubic terms and higher order terms), resulting in a polynomial equation when expanded. The consequent failure envelope is valid for anisotropic materials but can be easily simplified for orthotropic materials. Although it was an improvement on every criteria until that date and some terms of the tensor are of straightforward computation, others require experimental data that is difficult to obtain. Namely, the term  $F_{12}$  can only be determined with a biaxial test and it has very little sensitivity to biaxial stresses [37]. Like Hoffman [36], this criterion also indirectly states that tensile failure is dependent on compressive strength and vice versa.

Until then, all failure criteria were developed assuming a lamina as a homogeneous material. While this is a valid approximation, it combines the behaviour of fibre and matrix into one when it is known that they have different stress and strain responses when separate. To better understand and identify different failure modes in composites, Hashin and Rotem [38] developed a criterion based on a phenomenological approach, separating and assuming that fibre and matrix failure modes were independent. While fibre failure mode was expressed by the maximum stress criteria with respect to  $\sigma_{11}$ , a plane stress state and quadratic approximation of stresses was used for matrix failure mode, considering the interaction between  $\sigma_{22}$  and  $\tau_{12}$ .

Later in 1980, Hashin extended this criterion accounting for three-dimensional stress state, but only for unidirectional fibre composites [5]. Starting from stress invariants, he then wrote generic fibre and matrix mode failure and specified a different envelope for tensile and compressive cases. Contrarily to his previous work, he stated that tensile fibre failure mode was also influenced by shear stresses  $\tau_{12}$  and  $\tau_{13}$ . Perceiving the difficulty of correctly predicting matrix failure he also assumed a quadratic stress approximation but fully understanding that a loss of accuracy was being made [5].

When comparing the mentioned failure theories (except for the Hill and Hoffman criteria) in  $\tau_{12} - \sigma_{22}$  plots, Sun *et al.* [33] observed that the Tsai-Wu criteria showed better agreement with experimental results. However, due to its extensive and complex nature and for not considering phenomenological failure aspects he proposed an improvement on Hashin's criteria. He noticed from the experimental



data available that in the case of biaxial stress loading concerning  $\sigma_2$  and  $\tau_{12}$  the lamina showed greater strength when  $\sigma_2$  is compressive [33]. With that in mind, he introduced a parameter  $\mu$  in Hashin's compressive matrix failure mode equation that plays a similar role to a friction coefficient. This parameter differs from material to material and leads to better agreement between the theoretical curve and experimental results.

In 1998, Puck and Schürmann [11] also contributed to improve Hashin's criterion. With respect to fibre failure, they wrote the equations resorting to strains and not stresses, considering also that transverse stresses influence this failure mode. For compression specifically, they added an additional empirical shear stress correction to the failure envelope in the form of a distortion term  $\gamma_{21}$ . However, the most important contribution from Puck and Schürmann was to divide matrix failure mode in three distinct phenomena and being able to calculate the fracture plane angle  $\theta_{fp}$ . Mode A relates to transverse tension and mode B to transverse compression when shear stresses  $\tau_{12}$  are dominant over transverse stresses  $\sigma_{22}$ , both with  $\theta_{fp} = 0^\circ$ . Mode C is associated with transverse compression but when compressive stresses are dominant over the shear stresses, resulting in a fracture plane angle  $\theta_{fp} \neq 0^\circ$  [11].

In the turn of the 20<sup>th</sup> century, Dávila *et al.* [13] developed a new criteria designated LaRC03, having Hashin [5], Sun *et al.* [33] and Puck and Schürmann [11] as a starting point. LaRC03 consists in a set of six different equations based on phenomenological events. They assumed plane stress state for simplicity and derived their matrix failure equations based on Mohr-Coulomb theory. The main addition of this criteria is that it considers *in situ* strength properties by using fracture mechanics solutions [13]. They also included an additional toughness ratio  $g$  related to transverse stresses. The resulting equations describe one case of matrix tension, two cases of matrix compression, one case for fibre tension and two novel equations that describe fibre compression failure modes.

All the aforementioned theories were developed to predict composite failure based on a stress field. However, they do not consider the progressive nature of the damage that occurs in laminate composite materials, as is often verified experimentally [19, 39]. For this purpose, a fracture mechanics approach can be used to predict failure propagation, including delamination [15]. Moreover, these two criteria may be used in a hybrid approach, with stress-based criterion used to predict failure initiation and fracture mechanics for the failure propagation [15].

Matzenmiller *et al.* [10] had an important role in characterising the damage evolution in composites, developing an exponential damage growth law that is a function of the strain. Their work was later extended by Williams *et al.* [12]. Other important studies were made by Pinho *et al.* [14] and Donadon *et al.* [15].

## 2.3 A new progressive failure model for pultruded FRPs

The novel progressive failure model for quasi-orthotropic pultruded FRPs was developed by Gonilha *et al.* [3, 16] mainly to address the high computational costs of using the most recent works in finite element analysis [40–43], while still producing accurate results for most imposed stress states. For this

reason, the major simplification of considering composite materials as homogeneous was done, which results in the neglecting the explicit effect of delamination.

The model's formulation is divided in two stages: (i) failure initiation, and (ii) damage propagation. For the failure initiation, ellipsoid envelopes considering a quadratic combination of stresses are defined independently for in-plane (Eq. 2.1) and out-of-plane failure (Eq. 2.2):

$$F_{pl}(\sigma) = \left( \frac{\sigma_{11} - C_{11}}{A_{11}} \right)^2 + \left( \frac{\sigma_{22} - C_{22}}{A_{22}} \right)^2 + \left( \frac{\tau_{12}}{A_{12}} \right)^2 = 1 \quad (2.1)$$

$$F_{op}(\sigma) = \left( \frac{\sigma_{33} - C_{33}}{A_{33}} \right)^2 + \left( \frac{\tau_{13}}{A_{13}} \right)^2 + \left( \frac{\tau_{23}}{A_{23}} \right)^2 = 1 \quad (2.2)$$

where  $\sigma_{ii}$  and  $\tau_{ij}$  represent the normal and shear stresses in directions  $ii$  and  $ij$ , respectively,  $C_{ii}$  is defined as the average of tensile ( $S_{ii}^+$ ) and compressive strengths ( $S_{ii}^-$ ), and  $A_{ii}$  and  $A_{ij}$  are also functions of tensile, compressive and shear strengths (Eqs. A.1 to A.6, cf. Appendix A).

The failure indexes for in-plane ( $f_{pl}$ ) and out-of-plane ( $f_{op}$ ) are then defined by Eqs. 2.3 and 2.4, respectively:

$$F_{pl} \left( \frac{\sigma}{f_{pl}} \right) = 1 \quad (2.3)$$

$$F_{op} \left( \frac{\sigma}{f_{op}} \right) = 1 \quad (2.4)$$

As for the damage propagation model, an approach based on Matzenmiller *et al.* [10] was used, considering an exponential damage law but extending it for every direction. Figure 2.6 exemplifies the implemented stress vs. strain relationship for one direction only. The first undamaged stage is characterised by linear behaviour according to the undamaged elastic modulus. The second stage is where damage propagation occurs, with the elastic modulus ( $E$ ) defined as a function of the damage variable ( $D$ ) given by Eqs. 2.5 and 2.6:

$$D_i = d_{i,max}^{\pm} \left( 1 - e^{-\frac{f_{pl}(\hat{\sigma})^{m_i^{\pm}}}{m_i^{\pm} \cdot e}} \right) \quad i = 1, 2, 4 \quad (2.5)$$

$$D_i = d_{i,max}^{\pm} \left( 1 - e^{-\frac{f_{op}(\hat{\sigma})^{m_i^{\pm}}}{m_i^{\pm} \cdot e}} \right) \quad i = 3, 5, 6 \quad (2.6)$$

where  $d_{i,max}^{\pm}$  and  $m_i^{\pm}$  are the maximum damage allowed at this stage and the exponential damage evolution control variable, respectively, for the  $i$  direction, the superscript  $\pm$  indicates the load direction, and the failure indexes  $f_{pl}$  and  $f_{op}$  are computed for the effective stresses ( $\hat{\sigma}$ ).

The elastic modulus decreases until a residual value is reached (when the variable  $D$  is at its maximum and equal to  $d_{i,max}^{\pm}$ ). When the limit strain is reached ( $\epsilon_u$ ), the behaviour is characterised by a constant residual strength ( $\sigma_{bls}$ ) [3].

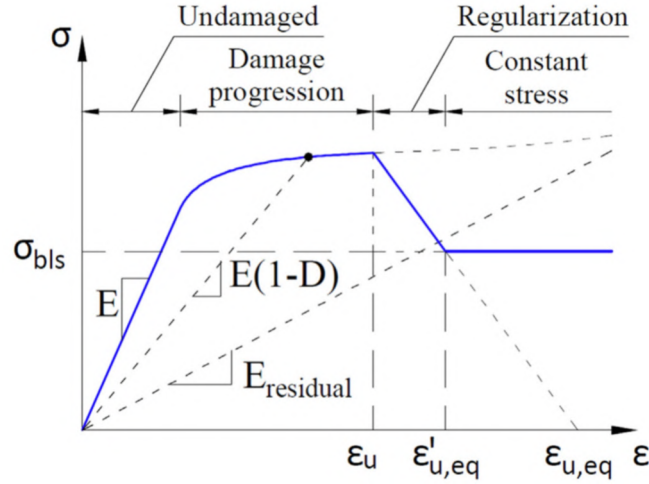


**Figure 2.6:** Stress vs. strain relationship (for one directional case) with four stages: (i) undamaged; (ii) damaged progression; (iii) mesh regularisation; and; (iv) constant stress. Source: [3].

Additionally, in order to tackle mesh sensitivity issues when implementing the model in FE applications, a regularisation stage between the damage progression and the constant stress stages is implemented by using a mesh regularisation parameter ( $\alpha$ ) that must be calibrated with experimental data. Furthermore, to avoid severe convergence difficulties in implicit analysis, an additional viscous regularisation parameter that depends on the time step interval used was defined for every direction ( $\eta_i^\pm$ , nine in total).

Although the preliminary tests performed in [3] and [16] showed that this decoupling of in-plane and out-of-plane failure is a reasonable approximation, more complex tests for non-orthotropic composites where there is a clear association between, for example, transverse and through-thickness stresses ( $\sigma_{22}$  and  $\sigma_{33}$ , respectively), may result in difficulties regarding the numerical prediction capabilities of the damage model. Moreover, it should be stressed that the distinction between the undamaged and damage progression stages is purely theoretical, as in reality only the damage progression stage is applied numerically until the limit strain is reached. This region, however, presents mostly linear behaviour, unless very small  $m_i^\pm$  values are used (smaller than 1).

Summarising, the damage model requires the calibration of 64 input variables: (i) 9 elasticity inputs, including elastic and shear moduli and Poisson coefficients ( $E_{ii}$ ,  $G_{ij}$ ,  $\nu_{ij}$ ), (ii) 9 strength inputs ( $S_{ii}^\pm$  and  $S_{ij}^\pm$ ), (iii) 18 damage progression control inputs ( $d_{i,max}^\pm$  and  $m_i^\pm$ ), (iv) 18 residual strength control inputs ( $\epsilon_{ii,u}^\pm$ ,  $\gamma_{ij,u}$ ,  $r_{ii}^\pm$ , and  $r_{ij}$ ), 9 viscous regularisation parameters ( $\eta_i^\pm$ ), and (v) 1 mesh regularisation parameter ( $\alpha$ ).

## Chapter 3

# Experimental material characterisation and application tests

This chapter is focused on the presentation of all experimental data used for this work. The first section addresses the previously performed material characterisation tests that were used to obtain the relevant mechanical properties in order to correctly calibrate the damage model for every material studied. The second section includes a more detailed description of  $10^\circ$  off-axis tensile tests performed by the author to better characterise the in-plane shear properties of a material already calibrated by Gonilha *et al.* [3]. The experimental setup and data processing methods are duly described, followed by the results and their discussion, comparing the properties obtained with the other method used (*i.e.* *Iosipescu* test). The third and last section focuses on the presentation of all experimental data used to address the damage model's validity. This data includes load vs displacement curves, stiffness and maximum load results and failure modes for several application tests with distinct characteristics.

These experimental tests, except for the  $10^\circ$  off-axis tensile test addressed in Section 3.2, were not performed by the author and their respective data was made available by the supervisors of this work and by Dr. Lourenço Fernandes [3, 8, 16, 44–51]. However, all data processing was done by the author, since the novel failure model requires a more detailed analysis on each test as it will be explained later in the chapter.

### 3.1 Experimental mechanical characterisation

This section presents the experimental methodology implemented to characterise the mechanical properties of all materials studied. As mentioned in Section 2.3, there are 18 variables needed as input for the novel failure model regarding mechanical properties, 6 corresponding to the material's elasticity moduli in all directions, 3 coefficients of Poisson and other 9 for the ultimate strengths.

Most of these properties were obtained through coupon tests. Some assumptions were made given the experimental data available and the preliminary studies [3, 16] that highlighted the non-existence of standardized tests to determine the through-thickness properties. Therefore, for each material,

(i) the through-thickness elasticity module ( $E_{33}$ ) and ultimate strengths ( $S_{33}^+$  and  $S_{33}^-$ ) were assumed to be the same as found in the literature [22–24] for similar GFRP materials, even though this information is scarce [3], (ii) for the shear moduli  $G_{13}$  and  $G_{23}$ , the  $G_{12}$  values were adopted, and (iii) for the Poisson coefficients (with the exception of I200-FC) and ultimate shear strengths for planes 12 and 13, the I150-AP values were adopted. With these simplifications and assumptions, only 5 experimental coupon tests were needed for each material, namely: (i) Longitudinal Tensile (LT) tests, (ii) Transverse Tensile (TT) tests, (iii) Longitudinal Compressive (LC) tests, (iv) Transverse Compressive (TC) tests, and (v) In-plane Shear (IS) tests.

### 3.1.1 Experimental programme and nomenclature

For this work, six different GFRP materials from four distinct suppliers were studied (all composed by E-glass type fibres and polyester resin). To explain the nomenclature used, the example I200-FC-W-LT-1 will be used. The first term refers to a profile with an “I” shaped cross-section and with 200 mm of height. The profiles studied also include “U” and “S” (“S” from SHS - square hollow section) sections. Figures 3.1 (a) to (c) show all different configurations. The second term refers to the profiles’ suppliers, which are “AP” (Alto Perfis Pultrudidos, Lda, a Portuguese manufacturer), “CP” (Creative Pultrusions, a US manufacturer), “FC” (Fiberline Composites, a Danish manufacturer), and “ST” (STEP - Sociedade Técnica de Estruturas Pultrudidas - a Portuguese supplier). Table 3.1 summarises the geometric details of each profile. The third term represents the plate from which the specimens were retrieved - “W” for the web and “F” for the flange.

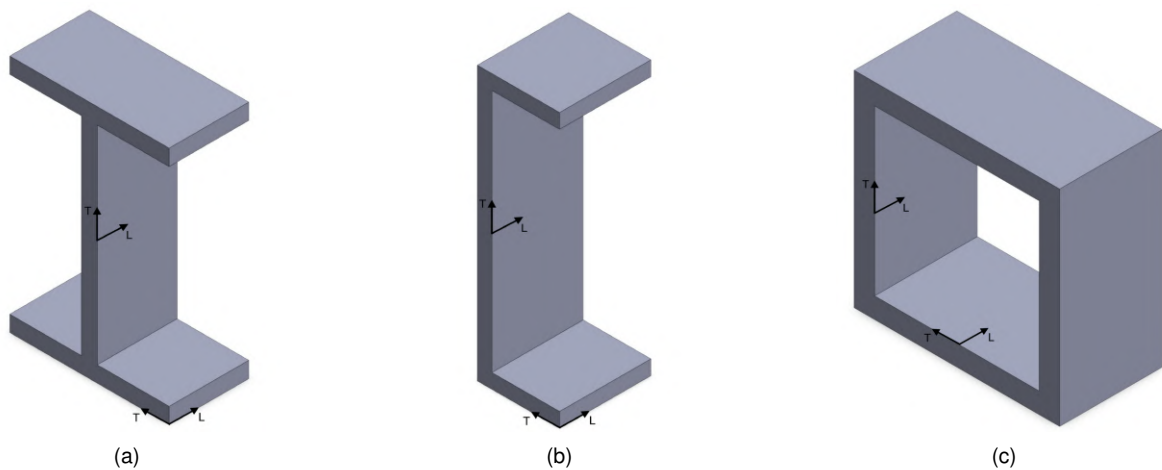


**Figure 3.1:** Different profiles studied: (a) I section; (b) U section; (c) S section.

The fourth term refers to the type of test in question - these can be LT, TT, LC, TC, *losipescu* and 10° Off-Axis Tensile (OAT) tests. Both *losipescu* and 10° OAT tests are used to retrieve the in-plane shear properties. Table 3.2 summarises the tests available (or performed) for each material. Finally, the last term indicates the number of the experimental specimen. For most tests with materials retrieved from the web, 5 to 6 specimens were used. For the flange, however, the data available was less complete, and when existent, usually only 2 specimens were used.

Material	Cross-section	Height [mm]	Width [mm]	Plate thickness [mm]	Web-flange radius [mm]
I200-FC	I	200	100	10	7
I150-AP	I	150	75	8	4
I150-ST	I	150	75	8	5
I152-CP	I	152	76	6	5
U150-ST	U	150	45	8	6
S120-AP	Square	120	120	10	-

**Table 3.1:** Profile's geometry and dimensions studied.

Material		LT	TT	LC	TC	IS	OAT
I200-FC	W	5	5	5	6	7	-
	F	6	-	-	-	4	-
I150-AP	W	-	-	-	-	-	4
I150-ST	W	5	4	6	8	-	-
	F	5	-	-	-	2	-
I152-CP	W	6	5	6	6	4	-
	F	2	-	-	-	-	-
U150-ST	W	4	5	6	6	4	-
	F	2	-	-	-	-	-
S120-AP		4	-	11	8	8	5

**Table 3.2:** Experimental programme and number of tested specimens for mechanical characterisation tests.

### 3.1.2 Tensile tests

#### Experimental test

The LT tests were performed according to ISO 527 [52]. Specimens with a nominal length and width of 250 mm and 25 mm, respectively, were taken from both web and flange for every material. The nominal thickness of the specimens varies with each profile geometry as described in Table 3.1. For the transverse tests, it was not possible to use the same length because of the profiles' geometric limitations. Instead, a nominal length of 160 mm was used for the I200-FC profile and 120 mm for other materials. It is important to note that there was no available data on the transverse tensile test for the S120-AP profile, and that this profile does not have a flange and web distinction.

Regarding the experimental setup, an *Instron* universal machine was used, and the specimens were gripped on both sides, in a length of approximately 40 mm. The displacements were obtained through a system of video-extensometry that recorded the displacements of the black dots marked in the specimens. Figures 3.2 (a) and (b) show a specimen being tested, before and after failure occurred.

#### Results

Representative results of both tensile tests are shown in Figure 3.3, and Table B.1 summarises the results (*cf.* Appendix B). The stress was calculated by dividing the load by the nominal cross-sectional area of each specimen. Moreover, the strain results presented after the ultimate load was achieved are not



**Figure 3.2:** Experimental setup of tensile test from I152-CP-W: (a) initial setup; (b) failure mode of a longitudinal specimen. Source: [44].

reliable, since the specimens' failure resulted in highly inaccurate readings from the video-extensometry system. Additionally, and only for the longitudinal tensile test of the I200-FC material, the Poisson coefficient for the plane 12 was also retrieved, with an average of  $\nu_{12} = 0.24$  and a co-variation of 6.8%. This value is omitted from Table B.1 for simplicity reasons.

For the longitudinal tests, all materials showed a linear behaviour until failure, with ultimate load values between  $\approx 300$  and  $\approx 450$  MPa. The elasticity modulus is similar in all materials, with values around 28 GPa.

For the transverse tests, the specimens showed a greater discrepancy between different materials for both ultimate load and elasticity modulus. These show a more non-linear behaviour than their longitudinal counterparts and the ultimate stresses range from  $\approx 30$  to  $\approx 120$  MPa. This non-linearity is explained by the more important role of the matrix in the structural behaviour of the material in this direction. This phenomenon also leads to greater difficulty in retrieving the elastic modulus  $E_{22}$ . Due to reasons duly explained in Section 4.3.2, these results are obtained in the first linear region, typically around 5 to 10 MPa.

Regarding the failure modes, longitudinal tensile tests registered significant delamination in large areas after the damage initiation phase (Figure 3.2 (b)), while transverse tests presented more localized damaged areas with less delamination (similarly to Figure 3.4 (b)) [44].

### 3.1.3 Compression tests

#### Experimental test

For most materials, the compression tests were performed with a Combined Loading Compression (CLC) test configuration, in accordance to ASTM D6641/D6641M - 09 [53]. This test aims to combine end- and friction-loading in both top and bottom grip lengths of the specimen to introduce a compression load. For longitudinal specimens, a nominal length of 150 mm and width of 16 mm was used, with the

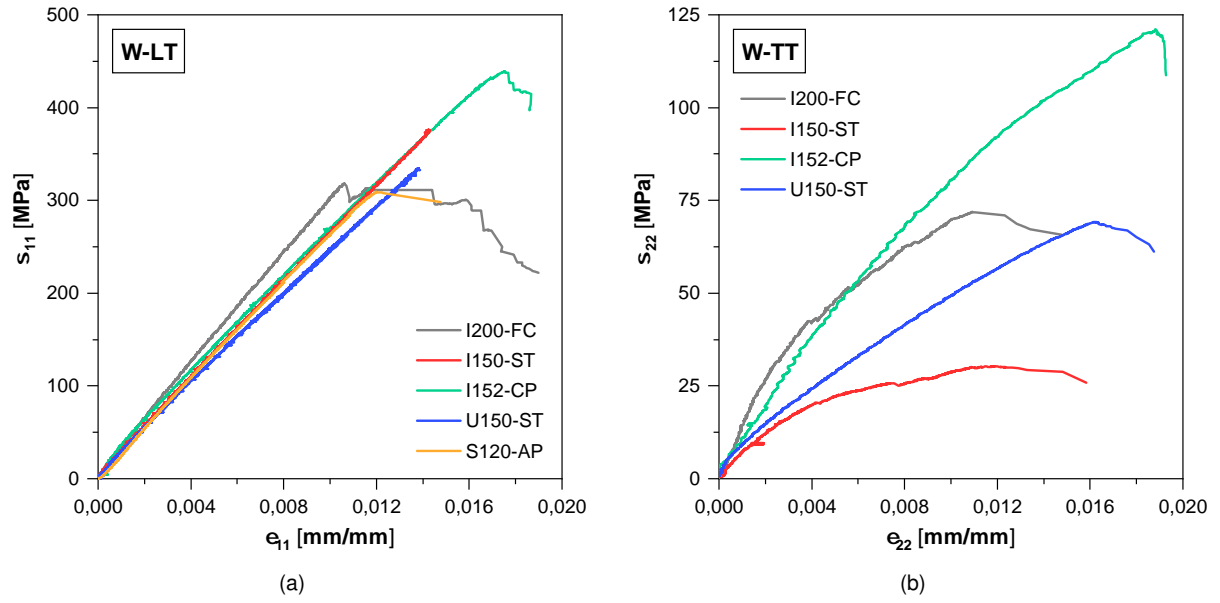


**Figure 3.3:** Representative stress vs. strain curves of experimental tensile tests: (a) longitudinal tension; (b) transverse tension.

thickness depending only on the profiles' geometry (Table 3.1). For the transverse specimens, however, a smaller length of 120 mm was used for the profiles with 150 mm of height. These shorter specimens were loaded only through the friction loading induced by the pressure on their lateral faces. Even so, these results were deemed valid as all failure modes registered experimentally were in conformity with the standard.

Figures 3.4 (a) and (b) show the test configuration before and after a specimen's failure. Similarly to the tensile tests, a video-extensometer was used to measure the displacements of the black dots marked in the specimen, as seen in Figure 3.4 (b). These dots were marked on the 23 mm window of free specimen present in the test setup.

The profile's S120 results, were obtained using a different standard - ASTM D 695-02 [54]. This test, in opposition to the first presented, introduces a compression load only in the bottom plate, as seen in Figure 3.4 (c), and the displacements were obtained directly from the bottom plate's displacement. All specimens were cut with a nominal length of 35 mm and 17.2 mm of width.

In the early study of the damage model, it was shown that the CLC test was able to predict the material behaviour until failure more accurately, allowing for more trustworthy results regarding elastic moduli and maximum stress values [3]. Nonetheless, for the transverse specimens' geometries presented below, the CLC configuration considerably overestimated the residual strength of the material due to its restrictive nature.

## Results

The results obtained in the compressive tests are shown in Figures 3.5 (a) and (b), with only one representative specimen of each material depicted. Table B.1 summarises all these results (*cf.* Appendix B).



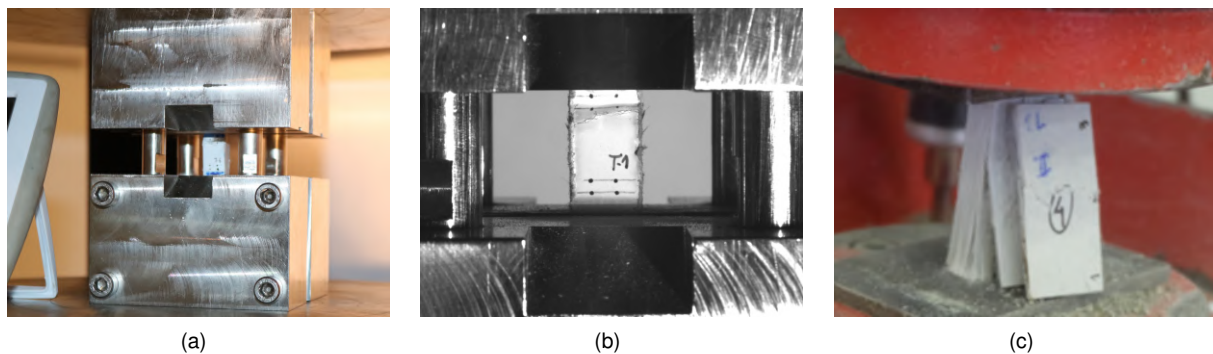


**Figure 3.4:** Experimental setup of compressive tests: (a) initial setup for the CLC configuration; (b) failure mode of a transverse specimen for the CLC configuration; (c) failure of a S120-AP specimen in compression following ASTM D 695-02. Source: [44].

Similarly to the tensile tests, the longitudinal specimens' results exhibit low scatter and present a linear behaviour. The longitudinal elasticity modulus of all specimens is around  $\approx 28$  GPa, almost identical to the tensile results. Their ultimate loads, however, present higher values than the tensile tests, ranging from  $\approx 430$  MPa to  $\approx 550$  MPa.

The transverse compressive results exhibit higher scatter than their longitudinal counterparts, following a similar trend as in the tensile tests. Additionally, these results show that not all materials' behaviour is the same. More specifically, the I200-FC stress vs. strain curve presented in Figure 3.5 (b) shows an almost bi-linear behaviour, the I152-CP and S120-AP curves are practically linear, and the I150-ST material exhibits a distinct exponential behaviour, similar to the transverse tensile test. This leads to increased difficulty in retrieving the elastic moduli in a single range, so these values were obtained from the first linear branch for each material in order to allow for better calibration of the progressive failure model (see Chapter 4), except for the I200-FC, where the second linear stage was considered. It is also important to note that the material S120-AP presents an almost perfect linear behaviour and the smaller elastic modulus. This can be explained by the different standard used to characterise this material, which is expected to underestimate the elastic modulus [55].

As for the failure modes, longitudinal specimens showed significant delamination (similarly to Figure 3.2 (b)) and transverse ones presented a more localized damage area, as seen in Figure 3.4 (b) [44].

### 3.1.4 In-plane shear tests

#### Experimental test

For all materials, *losipescu* shear tests were performed following the specifications of ASTM D5379 / D5379M - 05 [56]. The specimens' geometry was the following: rectangular specimens with 76 mm of length, 20 mm of width, and two  $90^\circ$  v-notches in the center. These were introduced through abrasive tools, resulting in a notch width of 12 mm. All specimens retrieved were aligned in the longitudinal direction.

The setup shown in Figure 3.6 (a) was connected to an *Instron* universal test machine in order to

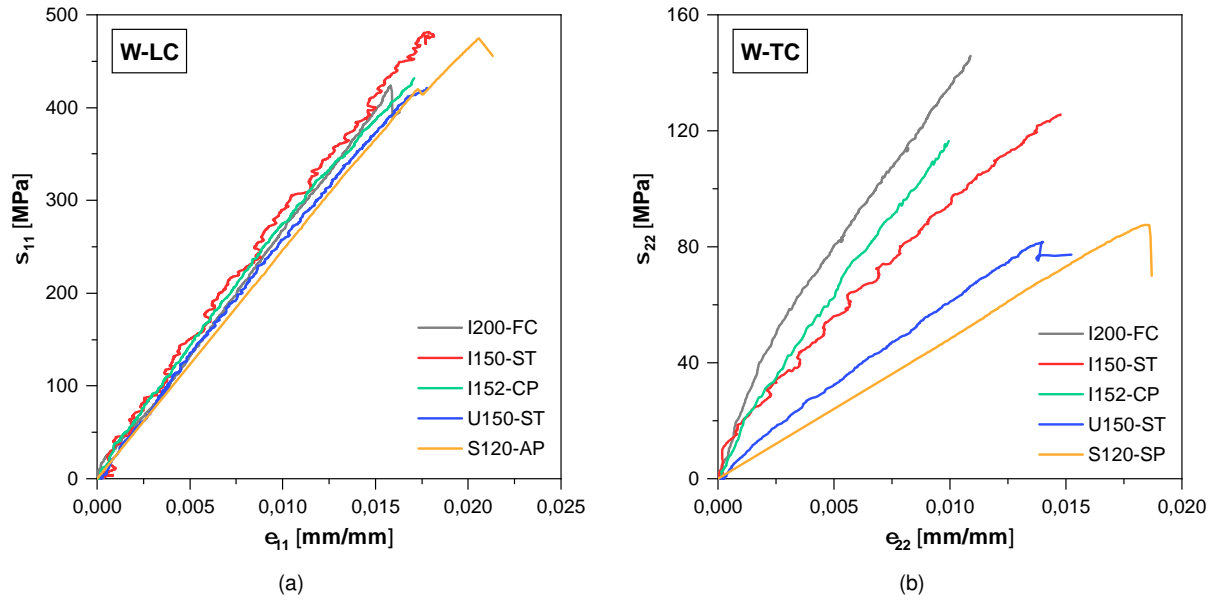


**Figure 3.5:** Representative stress vs. strain curves of experimental compressive tests: (a) longitudinal compression; (b) transverse compression.

apply a load on the right side steel block, pushing it downwards, while the left side steel block remained static. The strain measurements were computed from the displacements of the black dots marked in the center of the specimens at  $\pm 45^\circ$ , which were registered with a video-extensometer, with S120-AP being the only exception - no shear strains were obtained for these specimens.

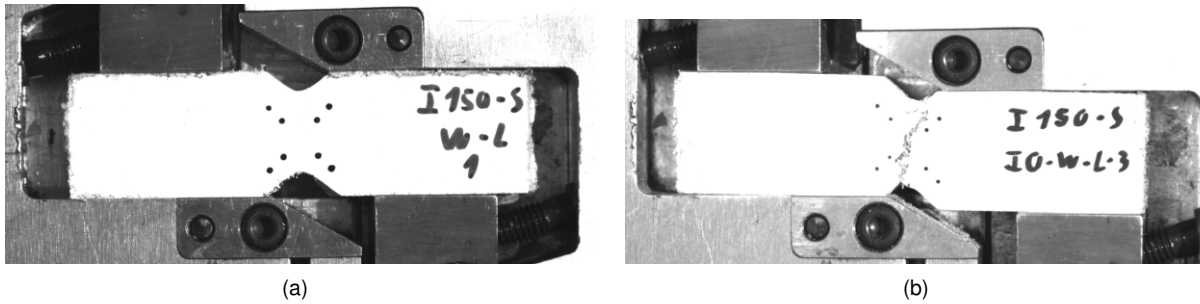


**Figure 3.6:** Experimental setup of a *losipescu* shear test for a longitudinal specimen from I150-ST-W: (a) initial setup; (b) failure mode. Source: [44].

Alternatively, the in-plane shear modulus of the S120-AP profile was determined with a  $10^\circ$  off-axis tensile test, following the recommendations in Hodgkinson [57]. It should be mentioned that these tests tend to underestimate the ultimate shear stress compared to the *losipescu* test, since the stress-state imposed in the specimen is not one of pure shear, but of a combined stress state [57]. Specimens were cut with 250 mm of length and 25 mm of width and the test setup is similar to the one represented in Figure 3.9 (a). A detailed explanation of this test setup will be addressed in Section 3.2.

## Results

Figure 3.7 (a) shows representative results obtained from the *losipescu* test and Table B.1 summarises the results (*cf.* Appendix B). All materials exhibit similar behaviour, with the shear modu-

lus averaging between 2.9 and 4.2 GPa and the ultimate shear stress between 65.3 and 70.8 MPa. The failure modes of this test were mainly by shear in the center of the specimen, as illustrated in Figure 3.6 (b), although some specimens presented some forms of crushing near this zone.

With respect to the OAT test, Figure 3.7 (b) presents the results of 3 specimens taken from the S120-AP material. The average shear modulus and ultimate shear stress are 3.4 GPa and 16.8 MPa, respectively. All specimens presented an oblique fracture in the same direction as the fibre alignment after failure, as depicted in Figure 3.9 (Section 3.2.1).

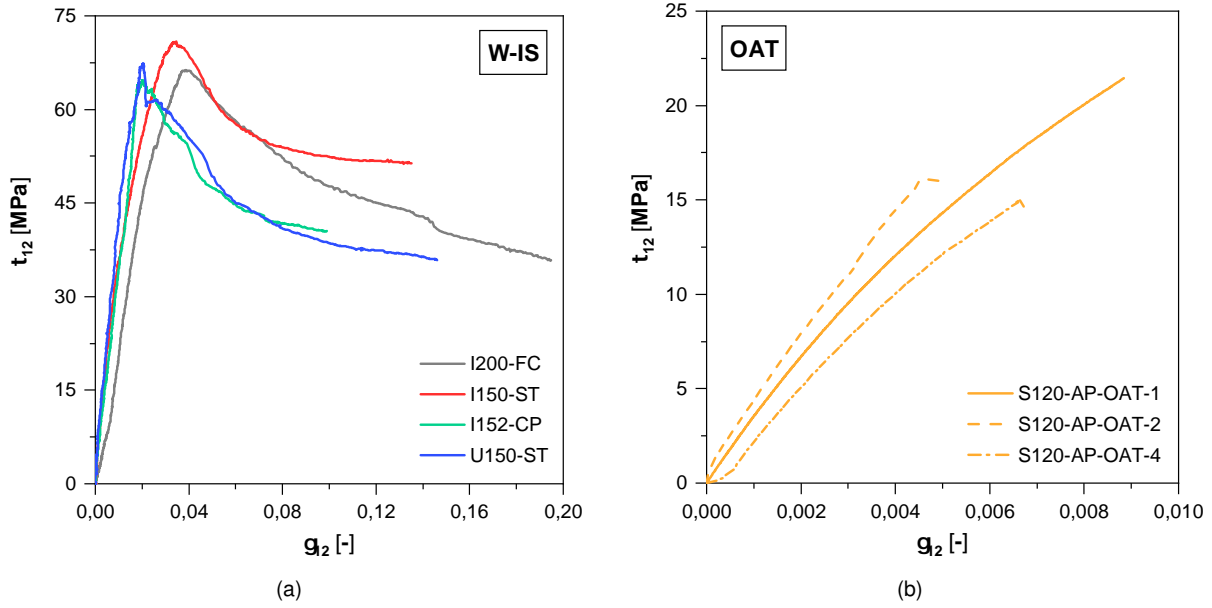


**Figure 3.7:** Representative stress vs. strain curves of experimental in-plane shear tests: (a) *losipescu* tests; (b) 10° off-axis tensile tests.

## 3.2 10° Off-axis tensile test

In the early studies of the damage progression model, the in-plane shear properties were determined by the means of an *losipescu* test. However, due to the experimental setup used, none of the specimens reached a point of complete failure, which lead to the adoption of calibration variables that therefore could not have been calculated:  $\gamma_{12} = 1$  (which translates in an unlimited ultimate strain) and  $\tau_{r_{12}} = 1$  (which means that the residual stress is equal to the ultimate stress) [3].

Hence, to better characterise the material studied in the preliminary work - I150-AP - a 10° Off-Axis Tensile (OAT) test was performed in the present work. This test consists in the application of a uniaxial tension load in a laminate specimen with the longitudinal fibres aligned at 10° with relation to the loading axis. This induces a biaxial stress state on the specimen. The angle of 10° is chosen because it minimises the effects of both longitudinal and transverse stresses and maximises shear strains [57, 58].

This section presents a detailed description of the OAT test performed. Firstly, the experimental setup is presented, followed by the data processing method used and the presentation of the results. Lastly, a comparison of these results with the *losipescu* test already performed in [3] is made.

### 3.2.1 Experimental procedure

For the experimental procedure, the guidelines presented by Hodgkinson were followed, since there are no ISO nor ASTM standards for this test [57]. Specimens were cut from the web from the I150-AP profile with the following dimensions: (i) 250 mm of length, (ii)  $\approx 150$  mm of free length, and (iii) 25 mm of width. This material has a thickness of 8 mm as presented in Table 3.1.

The strains were measured with two different systems: (i) a set of 4 strain gauges placed near the center of the specimen, and (ii) a video-extensometry system that reads the displacements of the blacked dots marked in the center of the specimen. These methods were used in all specimens, with one face of the specimen marked with the black dots and the opposite face with the strain gauges glued.

For the first method, the strain gauges (manufactured by *TML*, type FLKB-6-11-3LJC-F) were positioned with directions of  $0^\circ$ ,  $90^\circ$ , and  $\pm 45^\circ$  with relation to the test direction, as shown in Figure 3.8 (a). All data was gathered with a datalogger (manufactured by *HBM*, model QuantumX) at a rate of 10 Hz and stored in a pc.

For the second method, specimens were sanded and painted with matte white paint to enhance the contrast between the black dots and the specimen and facilitate the video-extensometer readings. The black dots were then marked with angles of  $0^\circ$ ,  $90^\circ$ , and  $\pm 45^\circ$ , with relation to the test direction. Figure 3.8 (b) depicts the final result. After the specimen was mounted in the loading machine, all data was registered with a camera at a rate of 10 Hz, with images being taken at a rate of 0.1 Hz.

For both these methodologies, the specimens were mounted in a universal *Instron* test machine (model 1343, with a maximum load capacity of 250 kN), as shown in Figure 3.9 (a). The gripped areas were pressured with 3 MPa at the beginning of the test, and a displacement rate of 2 mm/min was used. Figure 3.9 (b) displays the end of the test when the specimen has reached failure.

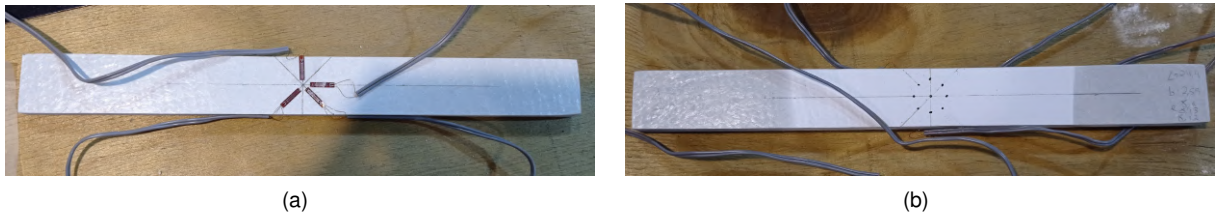


**Figure 3.8:** Experimental specimens used in OAT test with different strain measurement systems: (a) strain gauges; (b) video-extensometry system.

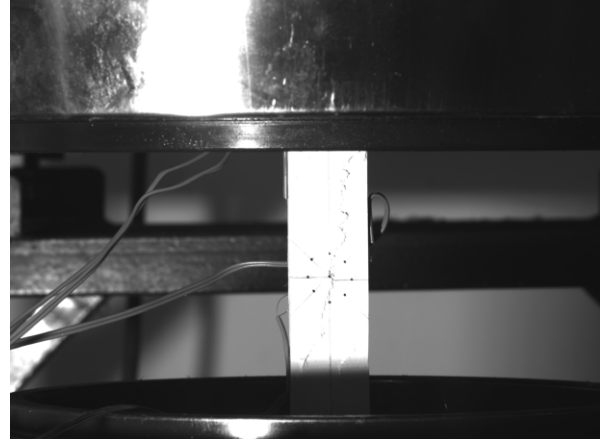
### 3.2.2 Data processing

The data processing phase was also performed according to Hodgkinson [57]. The load measured experimentally can be straightforwardly modified to the stress in the x direction  $\sigma_{xx}$  by dividing it by the cross-section area. Then, using Mohr's circle, it can be shown that:

$$\tau_{12} = \frac{1}{2} \sigma_{xx} \sin(2\theta) \quad (3.1)$$



(a)



(b)

**Figure 3.9:** 10° off-axis tensile test: (a) experimental setup; (b) failure mode.

where  $\theta$  is the angle between the principal direction (1) and the test direction (x), as shown in Figure 3.10 ( $\theta = 10^\circ$ ).

To compute the distortion ( $\gamma_{12}$ ), the first step is to transform the measured strains ( $\epsilon_{xx}$ ,  $\epsilon_{yy}$  and  $\epsilon_{xy}$ , cf. Figure 3.10) in global shear strains ( $\gamma_{xy}$ ) by using equation (3.2):

$$\gamma_{xy} = 2\epsilon_{xy} - \epsilon_{xx} - \epsilon_{yy} \quad (3.2)$$

The shear strain in global coordinates can then be transformed in the local coordinates' distortion using equation (3.3):

$$\gamma_{12} = (\epsilon_{xx} - \epsilon_{yy}) \sin(2\theta) + \gamma_{xy} \cos(2\theta) \quad (3.3)$$

With  $\tau_{12}$  and  $\gamma_{12}$  computed, it is possible to produce the stress vs. strain curves needed in order to retrieve the shear properties needed -  $G_{12}$  and  $S_{12}$ . The shear modulus  $G_{12}$  is obtained by a linear regression between the strain range of 0.05% to 0.25% [57].

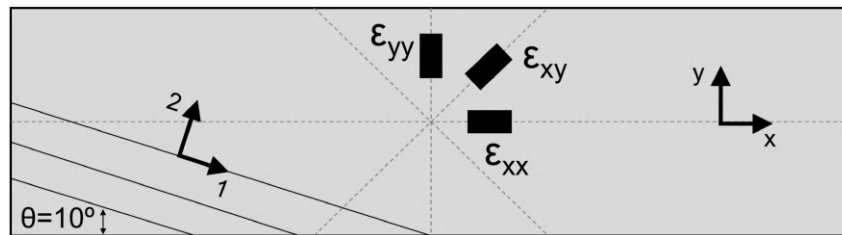


**Figure 3.10:** Schematic representation of a 10° off-axis tensile test specimen.

### 3.2.3 Results and discussion

The results were obtained for both methodologies, however, the video-extensometry system readings exhibited high levels of noise. For this reason, only the strain gauge's results are presented. Moreover,

all specimens exhibited the same failure mode depicted in Figure 3.9 (b), with a fully developed crack propagated from width to width parallel to the fibre direction ( $\approx 10^\circ$ ), after the peak load was reached.

The experimental curves obtained are depicted in Figures 3.11 (a) and (b). All specimens show identical results during the loading phase, with an approximate linear curve and then a slight reduction of stiffness in a second stage. The only exception is specimen number 4, where smaller cracks started to form earlier than its counterparts, resulting in a more accentuated loss of stiffness (Figure 3.11 (a)) and a consequent delay in reaching the maximum load (Figure 3.11 (b)). After failure (*i.e.* after the maximum load), all specimens experienced a sudden drop in stiffness, presenting a residual stress of  $\approx 20\%$  of the maximum load. This phase is omitted from the stress vs. strain curves (Figure 3.11 (a)) due to inaccurate readings of the strain gauges after failure.

Table 3.3 highlights the in-plane shear properties of both the OAT and *losipescu* tests. The shear modulus obtained from the OAT test is  $\approx 50\%$  higher than that obtained with the *losipescu* tests, while the ultimate shear stress is  $\approx 55\%$  lower.

Although some underestimation of the ultimate shear stress was expected due to the biaxial stress state induced in the specimen [57], the relative differences of both results ( $G_{12}$  and  $S_{12}$ ) are very high. The use of straight end tabs may be the main cause of the ultimate shear stress underestimation, as altering them from straight to oblique end tabs may lead to increases in shear stresses up to 37% [59]. Moreover, changing the tab material may also lead to an increase in ultimate shear strength measurements - using composite material tabs produces higher shear strength values compared to aluminium tabs (although steel tabs were used, their nature is similar to aluminium) [59].

Other less relevant factors that may influence the shear stress measurements are: (i) the non-linearity of shear stresses and shear strains across all points of the specimen, (ii) the fact that the fibres are not unidirectional in the material tested, and (iii) the effect of boundary conditions. Regarding the first point, it is important to understand that all formulae used for the data reduction are derived assuming an average stress and not a real stress distribution. Additionally, Ho *et al.* [60] concluded that the shear strain distribution is not uniform along the specimen length and width, with maximum differences of 16% and 4% obtained, respectively. Regarding the second point, it should be stressed that the composite does not have only unidirectional fibres. In fact, as studied by Almeida-Fernandes [44], the material I150-AP has a 78% of fibre weight aligned in the  $0^\circ$  direction, not 100% as expected for unidirectional composites. With relation to the boundary conditions, studies by Pagano and Halpin [61] and later highlighted by Pindera *et al.* [58] show that clamped ends produce additional shear stresses that influence the stress distribution, affecting the results of the shear modulus and ultimate shear stress obtained. The experimental end-constraints, although not fully clamped, may have produced the same effect. Finally, as an additional note, the possible misalignment of the strain gauges may have also contributed to some experimental errors regarding shear strains.

Moreover, the shear modulus difference between the two methods can also be correlated with their respective failure modes. While the *losipescu* failure mode leads to both fibre and matrix failure, the OAT test specimens' register failure only in the matrix, along the main the direction parallel to the fibres (Figure 3.9 (b)). Since the matrix is the main component responsible for the shear strength of GFRP

composites and this failure only occurs in the matrix, the shear modulus may be slightly higher in the OAT test.

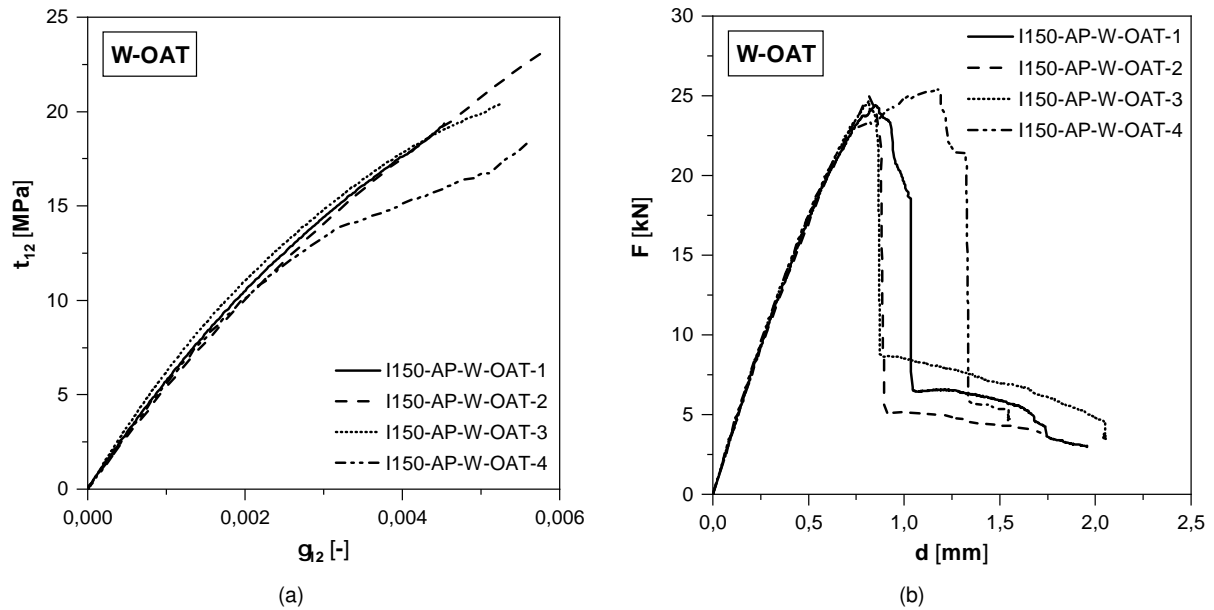


**Figure 3.11:** Experimental curves for all specimens of I150-AP-W: (a) stress vs. strain; (b) load vs. displacement.

Test	N. <sup>o</sup>	$G_{12}$ [GPa]		$S_{12}$ [MPa]	
		Av.	CoV (%)	Av.	CoV (%)
10° Off-axis tensile	4	4.70	2.7	20.4	9.7
<i>losipescu</i>	5	3.01	6.7	46.8	8.5

**Table 3.3:** Average and co-variation of OAT and *losipescu* tests' [3] main results for I150-AP-W.

### 3.3 Application tests

In this section, several experimental application tests are described. These tests are of the utmost importance as they allow to understand if the failure model correctly predicts reality. For this reason, different tests with distinct characteristics were assessed: (i) Compact Tension (CT) tests, (ii) Wide Compact Tension (WCT) tests, (iii) Compact Compression (CC) tests, (iv) Web-Crippling (WC) tests, and (v) Double-Lap (DL) tests.

The CT and WCT tests are mainly characterised by the highly concentrated transverse tensile stresses near the notch tip that lead to crack opening and propagation phenomena, while CC tests are similar but with transverse compressive stresses. The crack propagation in compact compression tests is also of a different nature, originating more complex failure modes. Web-crippling tests are mainly characterised by the propagation of transverse compressive stresses in the web section, but in different conditions to those of the compact compression test due to its geometry. Lastly, in-plane shear stresses are the most important aspect involving the double-lap tests.

### 3.3.1 Experimental programme and nomenclature

The profiles and materials used in the application tests are the same as previously studied in the experimental mechanical characterisation section and the experimental programme available is shown in Table 3.4. The nomenclature used follows the same logic, with the first term referring to the profile's geometry and the second to the manufacturer. Since all specimens were retrieved from the web plate of the profile (except for the web-crippling test, for which the specimen is the entire profile), this term was omitted.

Material	CT		WCT		CC		WC			DL					
	30	35	30	40	40	45	ITF-100	ETF-15	ETF-100	15	25	35	37	70	2B
I200-FC	3	3	5	5	5	1	3	3	-	-	-	-	-	-	-
I150-AP*	-	-	-	-	-	-	-	-	-	3	4	3	-	4	4
I150-ST	3	3	5	6	3	3	3	3	-	-	-	-	-	-	-
I152-CP	3	3	1	4	4	-	2	-	3	-	-	-	-	-	-
U150-ST	3	3	5	6	4	1	3	-	3	-	-	-	-	-	-
S120-AP	-	-	-	-	-	-	-	-	-	-	-	-	6	6	-

**Table 3.4:** Experimental programme available and number of tested specimens for application tests.

\* These double-lap tests were performed with plates with the same fibre architecture and matrix as I150-AP [51].

The third term now accounts for the test itself. The fourth term is a specific metric for each test: (i) for CT, WCT and CC tests, it represents the notch length of the specimen (*i.e.* I200-FC-CT-30 refers to a specimen with a 30 mm notch), (ii) for WC tests, it represents the web-crippling setup used, with both Internal Two Flanges (ITF) and External Two Flanges (ETF) being studied, and (iii) for DL tests, it represents the distance between the bolt and the edge (*i.e.* I150-AP-DL-15 refers to a specimen with a distance of 15 mm between the edge and the bolt). Additionally, web-crippling tests have a fifth term which indicates the bearing length used, in millimeters.

### 3.3.2 Compact tension tests

#### Experimental test

For the compact tension tests, specimens were cut in an approximately square shape, with 60 mm of nominal width and 58 mm of nominal height. Two holes were cut with a diameter of 12 mm as depicted in Figure 3.12 (a), and the notch was machined with a 2 mm thick circular saw blade, except for the last 5 mm of the notch length, which were cut with a 0.6 mm thick saw blade. This results in 25+5 mm for notch lengths of 30 mm and 30+5 mm for 35 mm notch lengths. Both holes of the specimen were fitted with a steel pin as shown in Figure 3.12 (a), with the bottom pin fixed and the top pin subjected to a displacement rate of 0.5 mm/min in the upwards direction. The load was applied through an *Instron* universal test machine with a maximum capacity of 250 kN.

Figure 3.12 (b) shows the displacement points used (Crack Mouth Opening Displacement (CMOD) circled in red), which were measured with a video-extensometry system, similarly to the process de-



scribed for the experimental mechanical characterisation. These CMOD points are in the same vertical axis as the center of the holes and present an initial distance of  $\approx 4$  mm.

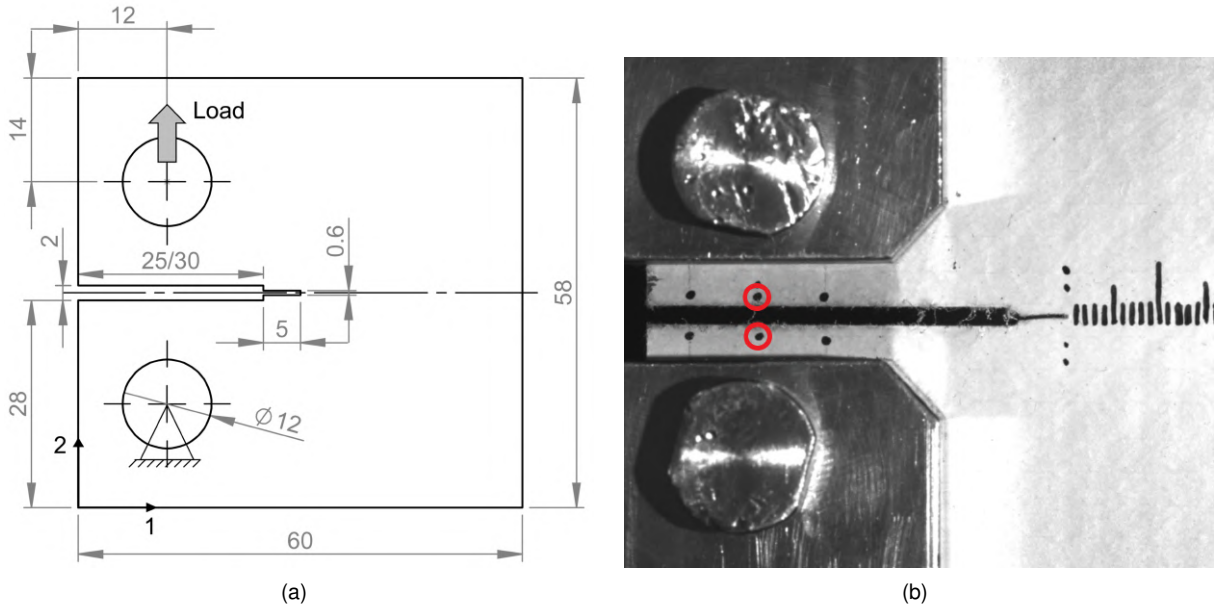


**Figure 3.12:** Compact tension tests - experimental setup: (a) schematic setup and dimensions (in mm); (b) CMOD points. Adapted from [46].

## Results

Figure 3.13 (a) shows representative results of the load vs. CMOD graphs obtained for each material and notch length and Table B.2 (*cf.* Appendix B) presents the experimental results deemed important for this study: (i) the stiffness ( $K$ ), measured between 10% and 20% of the maximum load, which was always a linear section, and (ii) the maximum load ( $F_{\max}$ ) reached in the test.

Regarding the load vs. CMOD curves (Figure 3.13 (a)), all materials show a similar trend - linear behaviour followed by a stiffness reduction until the maximum load is reached, ending with a softening stage. The different results for each material can be directly correlated with their aforementioned mechanical properties: (i) I200-FC presents a higher stiffness value since it exhibits the highest elastic modulus in tension for the transverse direction ( $E_{22}^+$ ), while the I150-ST and U150-ST have similar stiffness, and (ii) I152-CP has the highest transverse ultimate strength in tension ( $S_{22}^+$ ), hence the higher maximum load in this test. Moreover, an increased notch length results in a decrease in both stiffness and maximum load behaviour.

There was one main failure mode observed in this test - a crack opening that initiated in the notch tip and propagated transversely to the load direction (similarly to Figure 3.15 (b), *cf.* Section 3.3.3). This crack resulted from the tensile stresses present in this section of the specimen. However, specimens taken from I152-CP failed due to compressive stresses on the opposite side of the notch, causing delamination, as seen in Figure 3.13 (b). This different failure mode may be triggered by the fact that I152-CP was the only material which presented higher ultimate strength in tension than in compression.

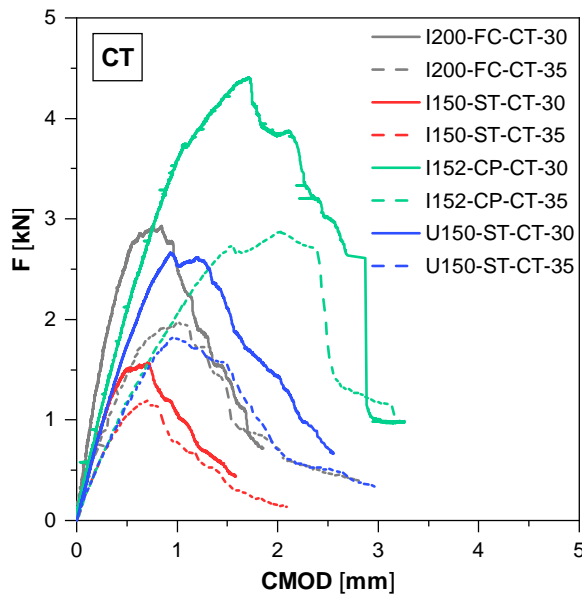


**Figure 3.13:** Compact tension tests - experimental results: (a) representative load vs. CMOD curves; (b) delamination due to compressive stresses in a I152-CP specimen. Source: [44].

### 3.3.3 Wide compact tension tests

#### Experimental test

The wide compact tension test setup is similar to the aforementioned CT test, except for the following: (i) a displacement rate of 1mm/min was used, and (ii) some specimens were subjected to load/unload cycles after reaching the maximum load.

Regarding the geometry, specimens were cut with 120 mm and 60 mm of nominal length and height, respectively, as shown in Figure 3.14. Moreover, the notches were cut with the same 2 mm thick saw blade, but the notch tip was sharpened with a 0.3 mm diameter wire saw. Notches of 30 mm and 40 mm were used (without considering the additional 0.3 mm).

#### Results

Figure 3.15 (a) shows representative load vs. CMOD curves obtained, and Table B.2 summarises the results (*cf.* Appendix B). For the specimens presented, only I150-ST-WCT-30 and both I152-CP specimens were not subjected to load/unload cycles. It can be seen that WCT tests follow the same trend described with detail in the CT results', except for the I152 profiles, which reached lower ultimate loads than the I200's. These specimens failed earlier than expected due to: (i) failure in the load application holes for notch lengths of 30 mm, and (ii) buckling coupled with failure in the load application holes for notch lengths of 40 mm. All other profiles failed due to crack propagation caused by tensile stresses (Figure 3.15 (b)).

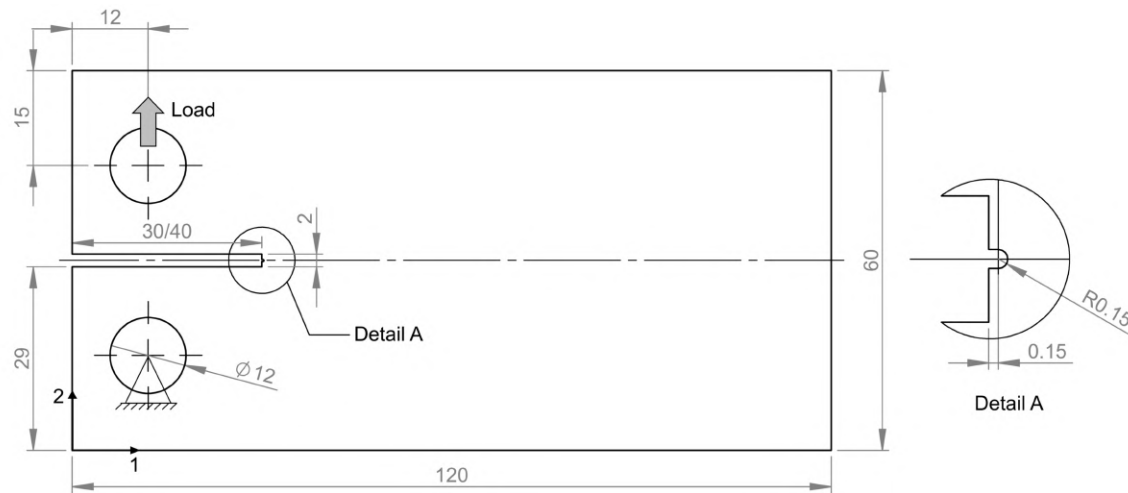


**Figure 3.14:** Wide compact tension tests - experimental schematic setup and dimensions (in mm).

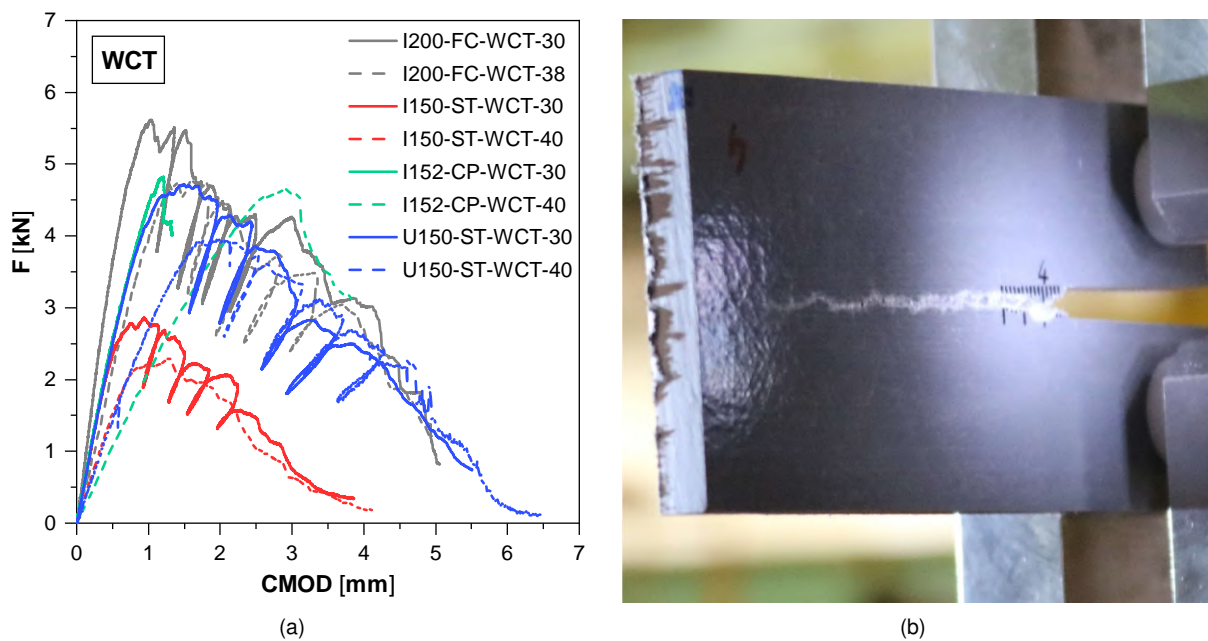


**Figure 3.15:** Wide compact tension tests - experimental results: (a) representative load vs. CMOD curves; (b) crack propagation (typical failure mode). Source [44].

### 3.3.4 Compact compression tests

#### Experimental test

Figure 3.16 (a) shows the specimens' geometry for this configuration. Even though this geometry corresponds to a scaled-up CC test, it will be referred to as a CC test for simplification. Specimens are square-shaped, with a side of 120 mm, and two holes cut with 12 mm of diameter. The notch has a triangular shape and a nominal horizontal length of 40 mm or 45 mm, ending with a semi-circular corner with a 2 mm radius.

The compact compression test setup is also similar to the CT test, however, the load is applied in the opposite direction, pushing the pin downwards at a displacement rate of 1 mm/min. The displacement points (Crack Mouth Closing Displacement (CMCD)) depicted in Figure 3.16 (b) were placed in the same

axis as the center of the holes and have a distance of approximately 11 mm between each other.

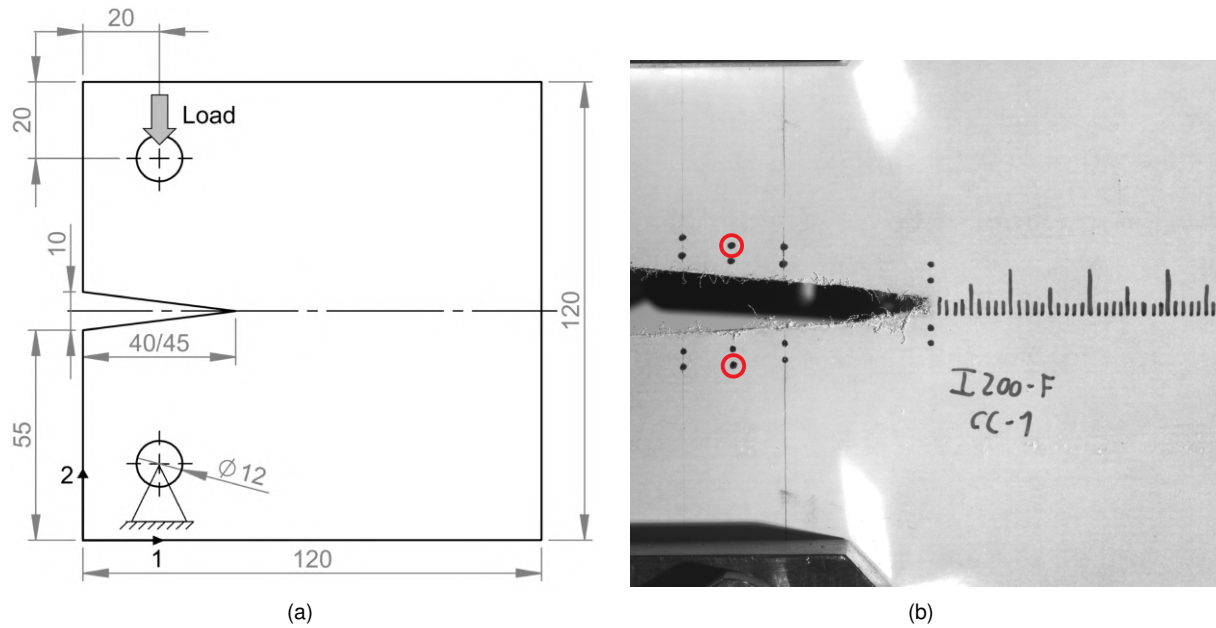


**Figure 3.16:** Compact compression tests - experimental setup: (a) schematic setup and dimensions (in mm); (b) CMCD points. Source: [47].

## Results

Representative results for the load vs. CMCD curves are shown in Figure 3.17 (a) and Table B.2 summarises all results (*cf.* Appendix B). It should be noted that no data regarding specimens with notch length of 45 mm was available for the I152-CP profile.

The curves show a similar behaviour except for I200-FC, with a linear slope until the maximum load, and a softening stage after. For the I200-FC, all specimens presented a slight drop in load after the linear branch, followed by a nonlinear behaviour until the peak load. This effect was attributed to the delamination of the material, which is more relevant in thicker profiles, as is the I200-FC [47].

As for the failure modes, there were two major types of ultimate failure, both registered during the softening stage: (i) specimens from I200-FC and I150-ST reached brittle tensile failure on the opposite side to the notch, as depicted in Figure 3.17 (b), and (ii) specimens from I152-CP and U150-ST presented buckling failure. These two modes were always preceded by the formation of a kink band originated due to compressive stresses that started in the notch tip and propagated along the longitudinal direction of the specimen.

### 3.3.5 Web-crippling tests

#### Experimental test

Both configurations used in web-crippling tests, Internal Two Flanges (ITF) and External Two Flanges (ETF), are exemplified in Figures 3.18 (a) and (b), with a compressive load being applied transversely to the web profiles.

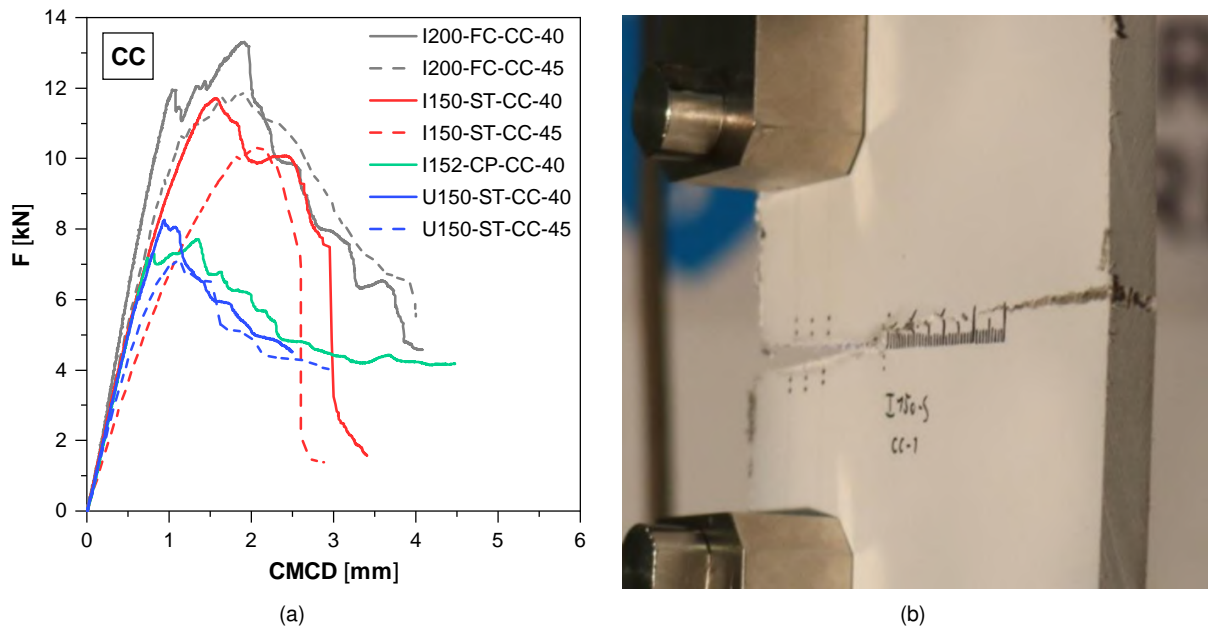


**Figure 3.17:** Compact compression tests - experimental results: (a) representative load vs. CMCD curves; (b) tensile failure mode on the opposite side to the notch. Source: [47].

For both ITF and ETF configurations, different bearing lengths were used in the experimental tests, namely, 15, 50, and 100 mm. However, this study will focus only on (i) the ITF-100 and ETF-15 for the materials I200-FC and I150-ST, since they represent the most extreme configurations, with ITF-100 representing a case where stresses are evenly introduced and may spread in both directions of the specimen, while ETF-15 represents a case with a higher concentrated load with limited spreading stresses in only one direction [16], and on (ii) the ITF-100 and ETF-100 configurations for the materials I152-CP and U150-ST, due to their different failure mode characteristics (highlighted in the results below).

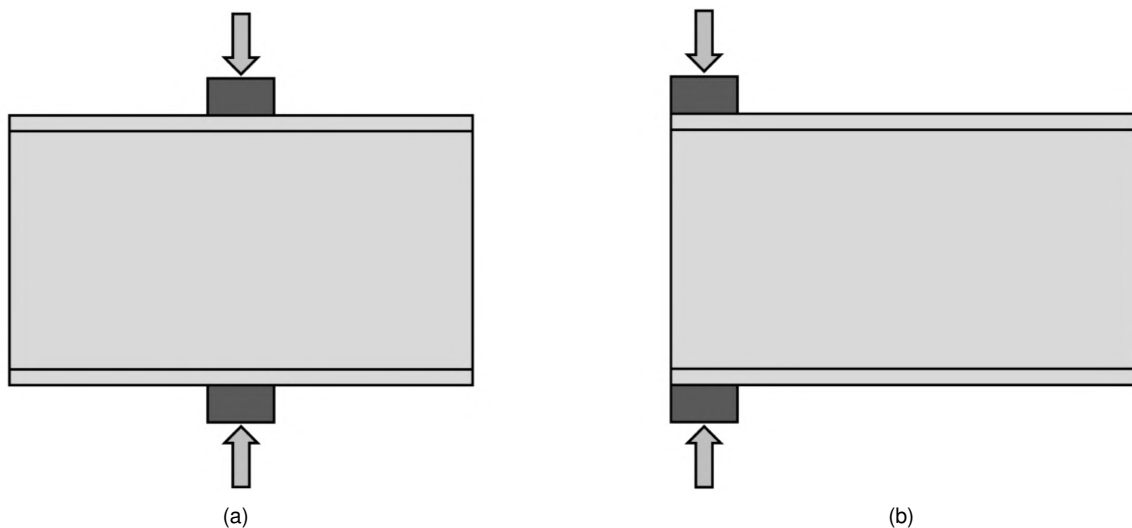


**Figure 3.18:** Web-crippling tests - schematic configurations of: (a) Internal Two Flanges; (b) External Two Flanges.

The specimens used for this tests are the entire profiles, with their cross-sectional geometry detailed in Table 3.1 and a length equal to two times their height ( $l=2h$ ). Tests were performed using the same

*Instron* machine to load the specimens and a displacement rate of 0.01 mm/s was used. As for the displacements, two different sets were registered: (i) cross-head displacement of the test machine, and (ii) displacement of the black dots marked in the specimens with a video-extensometer system. These points are specified with red circles in Figures 3.19 (a) and (b) and are located in the centre of the specimen for the ITF configuration, and at a distance of  $\approx 5$  mm from the edge for the ETF configuration.

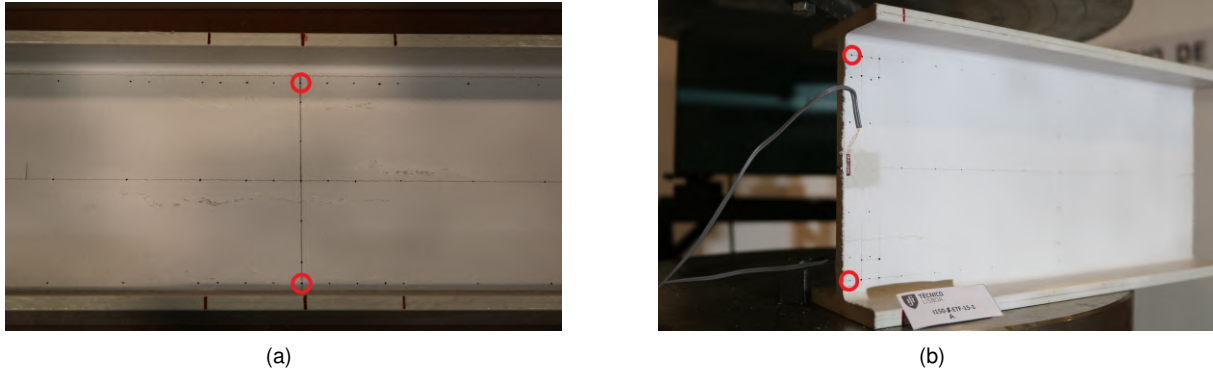


**Figure 3.19:** Web-crippling tests - location of the points used to measure the displacements in both configurations: (a) ITF; (b) ETF. Adapted from [44].

## Results

Figures 3.20 (a) and (b) show representative results obtained for both configurations, and Table B.2 summarises those results (*cf.* Appendix B). It should be stressed that, for better comparison with further numerical results, the load-displacement curves displayed are relative to the cross-head displacement of the test machine, since the video-extensometer readings are inaccurate after failure occurs. However, the experimental stiffness is computed using the displacements measured by the video-extensometer system because the cross-head displacement comprises other sources of flexibility [16].

For all bearing lengths and materials except for U150-ST, both configurations show a similar behaviour regarding the load-displacement curves, with a linear phase until the maximum load is reached, followed by an accentuated drop to a residual load level. As expected, the specimens tested under the ITF configuration presents higher failure loads than their ETF counterparts, and for the same configuration and bearing length, these web-crippling results follow a similar trend to the transverse compressive tests performed in Section 3.1.3 (*cf.* Figure 3.5 (b)).

Furthermore, the U150-ST material shows the same linear trend until the maximum load, however, due to its different cross-section profile and buckling failure mode addressed below, the loss in stiffness for both configurations is much less accentuated, resulting in a horizontal plateau, as depicted in Figures 3.20 (a) and (b).

As for the failure modes, the results may be summarised in two different categories: (i) web-crushing, where the failure is mainly concentrated in the web-flange junctions, as depicted in Figure 3.21 (a), and (ii) web-buckling, characterised by out-of plane displacements, as shown in Figure 3.21 (b). Web-crushing failure was registered in both ITF-100 and ETF-15 configurations of the I200-FC and I150-ST profiles, while I152-CP-ETF-100 showed clear signs of web-buckling failure. Moreover, some combina-



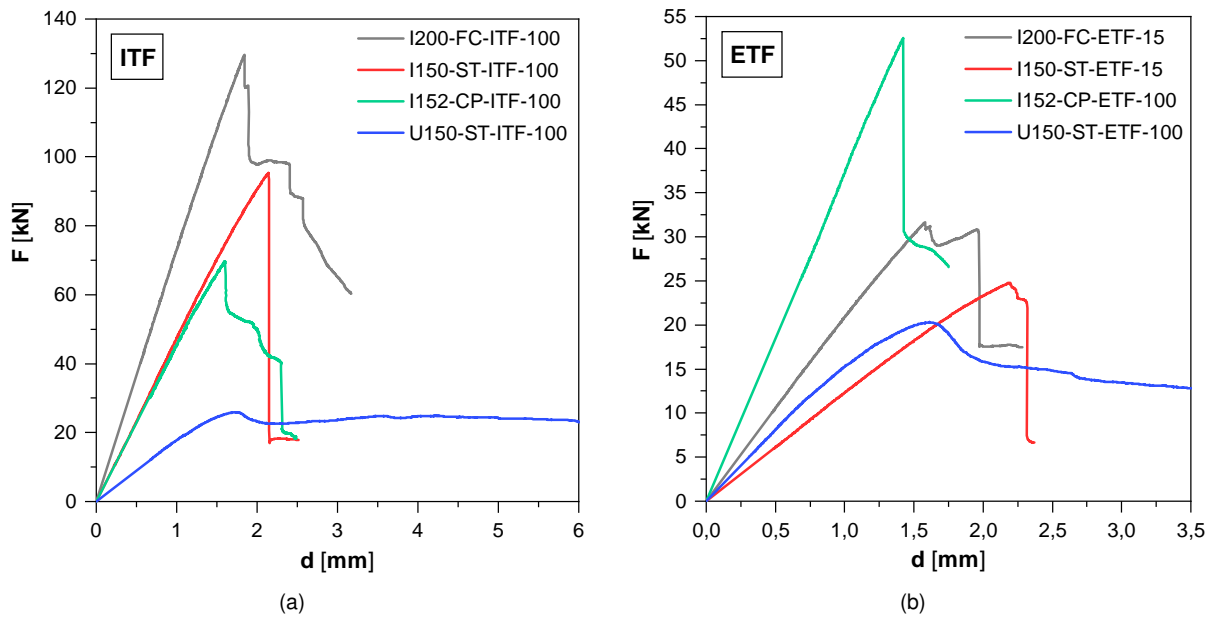


**Figure 3.20:** Web-crippling tests - representative load vs. displacement curves from experimental results for: (a) ITF-100 configuration; (b) ETF-15 and ETF-100 configurations.

tions of profile and test configuration presented a mixed failure mode (both web-crushing and buckling), namely I152-CP-ITF-100, U150-ST-ITF-100 and ETF-100. Whereas in I152-CP-ITF-100 this mixed failure mode was characterised by an initial phase of web-crushing near web-flange junction and, in a later stage when buckling occurred, the U150-ST profile presented a relatively steady-state failure mode, with both web-crushing and out-of plane displacements developing during the experimental tests.

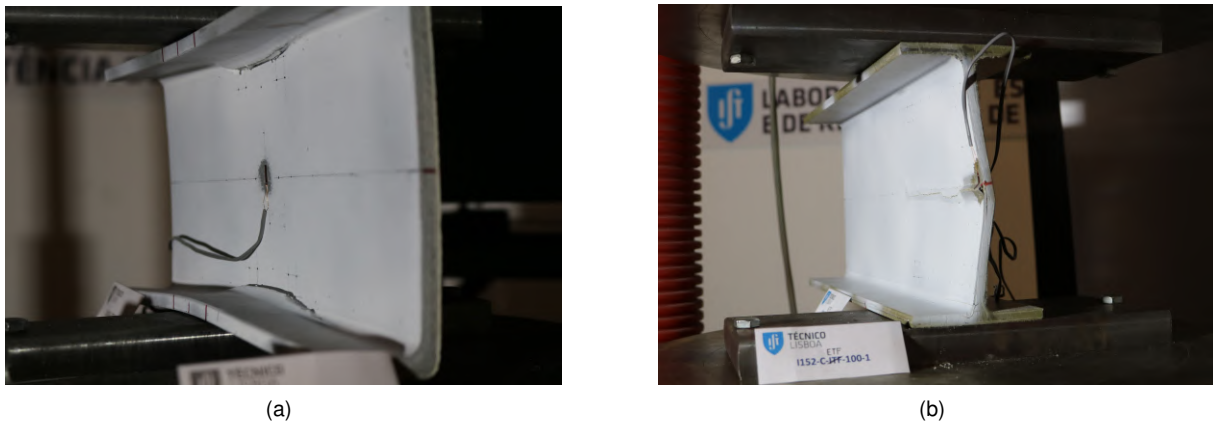


**Figure 3.21:** Web-crippling tests - main failure modes registered in experimental tests (a) web-crushing (U150-ST-ITF); (b) web-buckling (I152-CP-ETF). Adapted from [44].

### 3.3.6 Double-lap tests

#### Experimental test

Figure 3.22 illustrates the double-lap test configuration adopted. GFRP specimens' with 350 mm of length and 40 mm of width were cut from plates with the same fibre architecture and matrix as I150-AP

and from the material S120-AP. Additionally, for I150-AP, a hole with 8 mm of diameter was drilled at different edge distances for each specimen, namely: (i) 15 mm (DL-15), (ii) 25 mm (DL-25), (iii) 35 mm (DL-35), (iv) 70 mm (DL-70), and (v) two bolts with edge distance and inner spacing of 35 mm (DL-2B). As for S120-AP, the edge distances used were: (i) 37 mm, and (ii) 70 mm.

The GFRP plates were bolted to two steel plates, as seen in Figures 3.22 (b). The 8 mm diameter bolts (DIN931 M8 × 65) were not threaded in the contact with the plates and the steel plates were placed with a clearance of 2 mm in order to not produce any friction with the specimens. All tests were performed with an *Instron* universal testing machine, and a displacement rate of 2 mm/min was used. The displacements were measured with two displacement transducers (*TML*, model CDP-50) placed in the sections A and B, as depicted in Figure 3.22 (b).

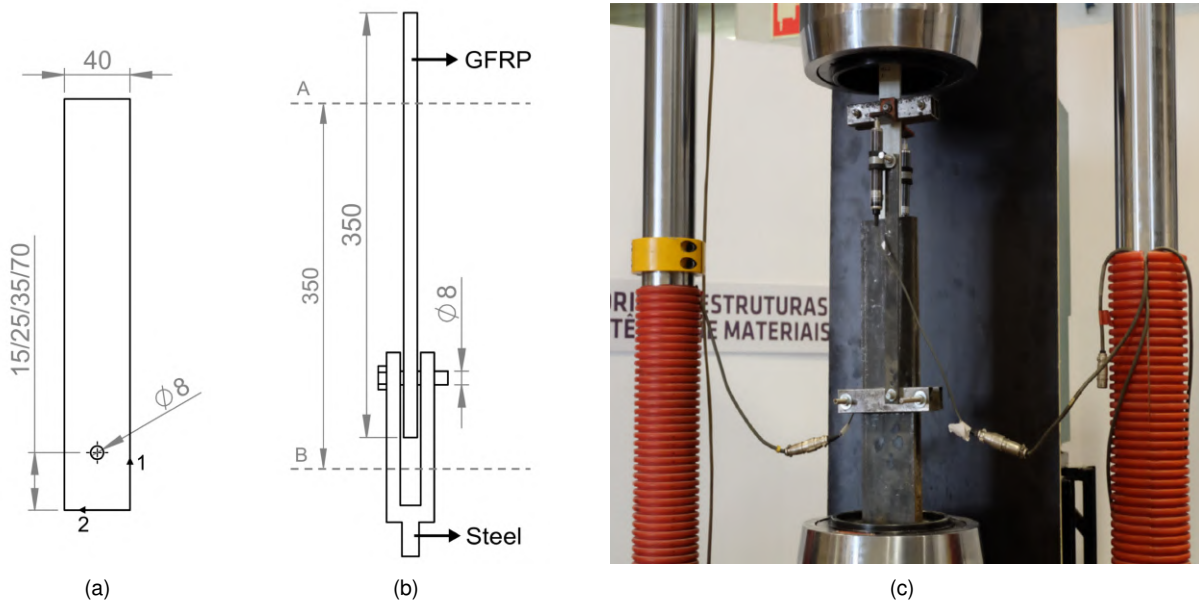


**Figure 3.22:** Double-lap tests - experimental setup: (a) schematic GFRP plate dimensions (in mm); (b) schematic setup; (c) experimental setup. Source: [51].

## Results

For the double-lap test, two different failure modes were registered: (i) shear-out failure, which occurred in DL-15, DL-25 and DL-35 tests for the material I150-AP, as depicted in Figure 3.23, and DL-37 of S120-AP, and (ii) bearing failure, which occurred in DL-70 tests for I150-AP and S120-AP (Figure 3.23) [50, 51]. This latter failure mode was followed by shear-out in all specimens. As for the DL-2B configuration, both types of failure were registered, but it was not possible to identify which one occurred first [51].

The results obtained regarding load vs. displacement curves are shown in Figures 3.24 (a) and (b), while the stiffness and failure loads are summarised in Table B.3 (*cf.* Appendix B). For I150-AP specimens where shear-out was the only failure mechanism registered (Figure 3.24 (a)), curves present always the same trend, with a linear response until a maximum load is reached, followed by a sudden drop in stiffness and a final stage of a constant, but significantly lower, load. For S120-AP, an interme-



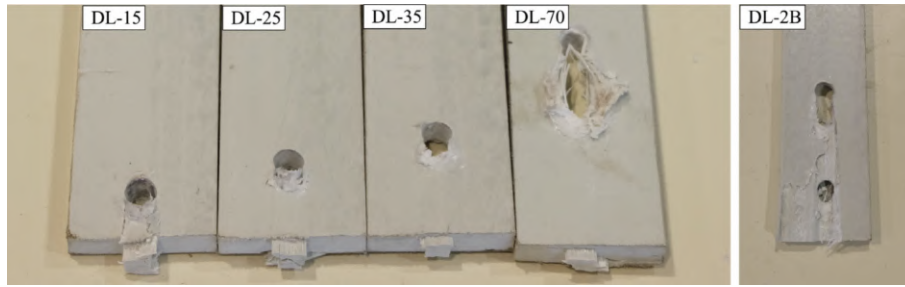


**Figure 3.23:** Double-lap tests - failure modes of I150-AP specimens for all configurations. Source: [51].

mediate stage after the first failure where the load increases with a more reduced stiffness than the first one until a second failure load is attained was also registered, ending with the same lower constant load. This latter stage of constant load is when the material is being removed from the specimen's initial geometry. Both stiffness and failure load increase with the bolt-edge distance.

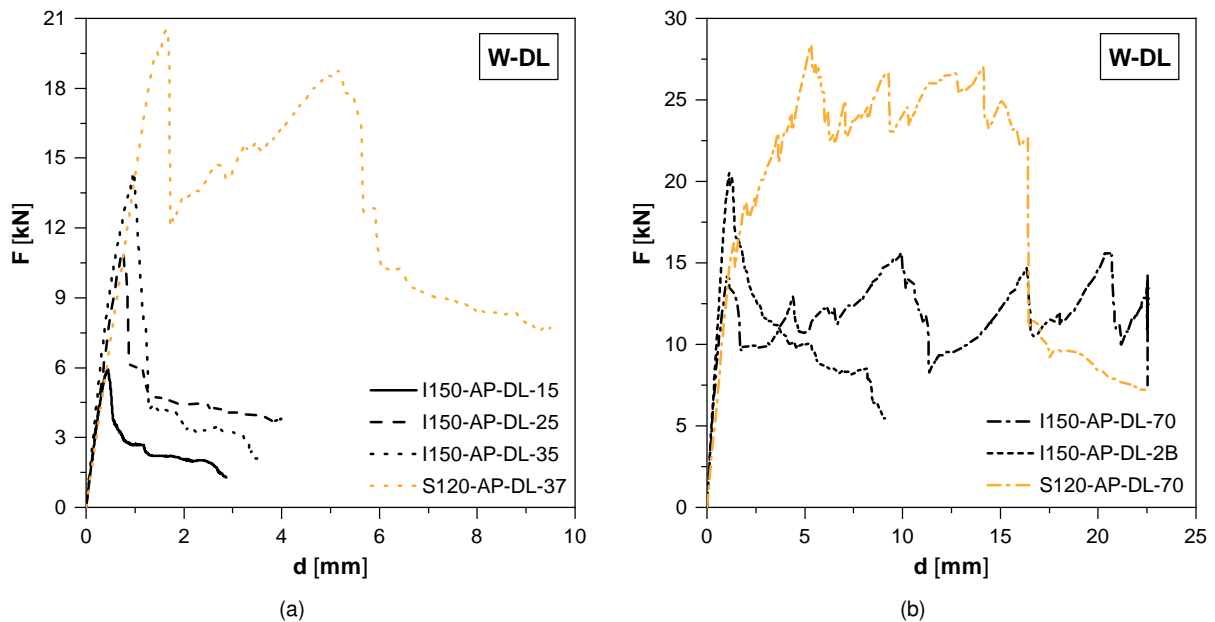


**Figure 3.24:** Double-lap tests - Representative load vs. displacement curves from experimental results: (a) Shear-out failure mode; (b) shear-out and bearing failure modes.

As for the specimens which presented combined bearing and shear-out failure, the experimental curves also show a linear behaviour until the maximum load is reached, however, instead of a sudden drop in stiffness, these specimens exhibit load fluctuations around an almost horizontal plateau, until an ultimate load drop occurred, when shear-out began. These load fluctuations coincide with the bearing failure phase. The only exception is the DL-2B test, where instead of a horizontal plateau, the load slowly decreases until ultimate failure occurs. This test presents an intermediate behaviour of both DL-35 and DL-70 tests, which can be explained by the specimen's geometry.

## Chapter 4

# Calibration of the model for new materials

In this chapter, all steps regarding the numerical calibration of the damage progression model are addressed. The calibration process is done by comparing (i) the numerical and experimental elastic moduli and ultimate stresses, and (ii) the shape of numerical and experimental curves. This process is performed for every combination of test and material addressed in Sections 3.1 and 3.2, and for the CT test (*cf.* Section 3.3.2). For this purpose, the ABAQUS FEA software package [21] was used, and all simulations were performed using the UMAT developed by Gonilha *et al.* [3].

The first section is focused on the finite element models used, their geometric characteristics, boundary conditions and simplifications with relation to the experimental tests, and general mesh and step configurations. Section 4.2 addresses the calibration process by explaining in a more empirical approach the effect of every input in the stress vs. strain curves, and a mesh study that included element size and numerical parameters' sensitivity analysis. In the third section, the main calibration results are presented and discussed, namely (i) the calibration inputs for every material and test, (ii) the numerical vs. experimental elastic moduli and ultimate stresses, (iii) the shape agreement between numerical and experimental curves, and (iv) the numerical failure modes obtained compared to the experimental data (only for *Iosipescu*, OAT, and CT tests).

### 4.1 Description of FE models

The Finite Element (FE) models can be divided into two main groups regarding their stress distributions, namely those with (i) uniform stress states, which is the case for tensile and compressive tests, and those with (ii) non-uniform stress states, which comprise both in-plane shear tests (*Iosipescu* and 10° off-axis tensile test) and the compact tension test. Nonetheless, for an accurate FE model description, it is easier to classify the models by their overall geometry, therefore, this section comprises the following subsections: (i) tensile tests comprising of longitudinal, transverse, and 10° OAT tests; (ii) compressive tests; (iii) *Iosipescu* tests; and finally (iv) compact tensions tests. These subsections

are preceded by some general considerations about all FE models.

#### 4.1.1 General considerations

Since one of the main objectives of the damage model developed is to minimise the computational costs while also accurately simulating the real behaviour of the material, some simplifications were made. Symmetry conditions and simplifications regarding the experimental tests' boundary conditions were used whenever possible.

Furthermore, regarding the mesh properties, C3D8R elements (8-node brick element with reduced integration) were used in every model, always with "enhanced hourglass control". To avoid the possible influence of the mesh regularisation factor on the results and given its dependency on the elements' specific length ( $L_e$ ), "mesh controls" were always assigned with the main priority of generating a regular cuboid-element mesh [3].

Moreover, the displacement steps' maximum and minimum increment sizes were set to 1% and  $1 \times 10^{-8}\%$  of the total displacement, respectively, for all tensile and compressive models, and decreased to 0.2% and  $1 \times 10^{-10}\%$  for the *losipescu* and compact tension test, due to convergence difficulties. Implicit analysis were conducted for all models allowing for a maximum residual flux norm of 1%, except for severe discontinuity iterations, for which that value was increased to 5% [3].

Finally, the loads were obtained using reference points which were coupled to the loaded faces in each test. Furthermore, the displacements were measured in the same location as the experimental specimens, with partitions being created when needed in the correspondent locations to ensure this was always the case.

#### 4.1.2 Tensile tests

For tensile test specimens', triple symmetry boundary conditions were used, meaning each dimension of the specimen was reduced to half of the specified in Section 3.1.2. Additionally, to force the failure to occur in the centre of the specimen, a "weak region" with  $1 \text{ mm}^2$  of area and through the entire thickness was introduced. This region was modelled with the same material as the rest of the specimen, except for the limit strains ( $\epsilon_{ii,u}^{\pm}$  and  $\gamma_{ij,u}$ ), which were reduced to 90% of the original values. A tie constraint between this weaker region and the rest of the specimen was used in order to ensure a realistic behaviour. A numerical model is shown in Figure C.1 (a) (*cf.* Apendix C).

As for the OAT test, the only relevant differences compared to other tensile tests are (i) the use of only one symmetry boundary condition in the z plane, (ii) the introduction of a coordinate system rotated  $10^\circ$  with relation to the length as indicated earlier in Figure 3.10, with the material's orientation defined by this coordinate system, and (iii) the non-existence of a weaker region in the center of the model, since, in this case, a non-uniform stress state is introduced and, therefore, the numerical failure does not start in the center of the specimen but near the edges [60], as will be discussed in Section 4.3.6.

### 4.1.3 Compressive tests

Regarding the compressive tests obtained with the CLC configuration, the FE model adopted simulated only the free window of the specimen with 23 mm of length (see Figures 3.4 (a) and (b)). Therefore, as a simplification, the load was modelled with a simple compressive displacement in one end of the specimen, as opposed to the combined end- and shear-loading present in the experimental specimen (*cf.* Section 3.1.3).

Furthermore, only a double symmetry boundary condition was used (for the transverse and thickness directions), as the use of half of the 23 mm of length resulted in an undesirable failure mode that started on the end boundary conditions (fixed and loaded faces). Since this model also contains a weak region imposed in the center of the specimen, failure onset should be in that location. Figure C.1 (b) (*cf.* Appendix C) shows a numerical model for a compressive test.

For the S120-AP, where the experimental results were obtained from a different standard, the same conditions were used.

### 4.1.4 *Iosipescu* tests

For the *Iosipescu* test's modelling, symmetry boundary conditions were applied only at mid-thickness, and in addition to the reference points applying the load and the fixed boundary conditions on the top right and bottom left faces, respectively (Figure C.2 (a), *cf.* Appendix C), two steel parts were added ( $E_s = 200$  GPa and  $\nu_s = 0.3$ ) on the top left and bottom right faces, as in the experimental setup (*cf.* Figure 3.6), in order to avoid the development of unrealistic tensile stresses at these zones [3]. The interaction between the steel parts and the GFRP material was set with a normal behaviour of "hard contact", and a "penalty" formulation with a friction coefficient of 0.1. Moreover, this contact was defined with a "finite sliding" formulation, and a contact stabilization factor of  $1 \times 10^{-4}$  was used.

### 4.1.5 Compact tension tests

The compact tension FE models were modelled accordingly with Figure 3.12 (a) presented earlier. Only one symmetry boundary condition at mid-thickness was used, and the same contact formulation as in the *Iosipescu* test was applied between the steel pins and their respective coaxial surface of the specimen. Moreover, to lower the computational costs of the mesh sensitivity analysis, the area near the notch where the stress distributions were expected to be more intricate was meshed independently of the remainder of the specimen. Figure C.2 (b) (*cf.* Appendix C) shows the boundary conditions's view of the numerical model used.

## 4.2 Preliminary calibration study

### 4.2.1 Calibration process

As explained in Section 3.1, the starting point for calibrating the damage model is the obtainment of 18 variables associated with the mechanical properties of the material, namely, elastic and shear moduli, Poisson coefficients and ultimate strengths, in all directions. The assumptions made regarding some of these variables were also mentioned in Section 3.1. Nevertheless, an additional assumption is made to facilitate the implementation of the damage model - due to the proximity of the elastic moduli between tensile and compressive tests, only one modulus is used for each direction ( $E_{11}$  and  $E_{22}$ , instead of  $E_{11}^+$ ,  $E_{11}^-$ ,  $E_{22}^+$  and  $E_{22}^-$ ). For this study, the author decided to use the elastic moduli retrieved from the tensile tests, since, for some of the compressive experimental tests, not all guidelines were thoroughly followed (cf. Section 3.1.3).

The next calibration steps are to define (i) the residual strength control inputs (ultimate strains and residual strengths) in each direction, which are also retrieved from the experimental coupon tests characterised earlier, (ii) the damage progression inputs (maximum damage allowed and exponential damage evolution control variables) through a curve fitting process, and (iii) the regularisation coefficients (mesh and viscous regularisation factors).

#### Residual strength control inputs

The computation of these variables is straightforward, with the ultimate strains ( $\epsilon_{ii,u}^\pm$  and  $\gamma_{ij,u}$ ) being calculated in two different ways: (i) ratio between maximum stress and the elastic modulus (equation 4.1), for linear behaviour tests; and (ii) directly from the stress vs. strain curves, for non-linear behaviour tests. The residual strength ( $r_{ii}^\pm$  and  $r_{ij}$ ) are the fraction between the residual stress (constant stress phase after failure) and the maximum stress (equation 4.2).

$$\epsilon_{ii,u}^\pm = \frac{S_{ii}^\pm}{E_{ii}^\pm} \quad \vee \quad \gamma_{ij,u} = \frac{S_{ij}}{G_{ij}} \quad (4.1)$$

$$r_{ii}^\pm = \frac{\sigma_{r_{ii}}^\pm}{S_{ii}^\pm} \quad \vee \quad r_{ij} = \frac{\tau_{r_{ij}}}{S_{ij}} \quad (4.2)$$

These results are only obtained for the experimental tests performed in Chapter 3, with values for other directions being extrapolated from the I150-AP material and the literature, as previously mentioned [3].

#### Damage progression control inputs

The calibration process then consists in calibrating the damage progression control value inputs ( $d_{i,max}^\pm$  and  $m_i^\pm$ ) through a curve fitting process, for every test performed. In a simplified way, the maximum damage control variable ( $d_{i,max}^\pm$ ) is approximately 0 for linear curves, and can be increased until it equals 1, although never reaching it, for curves that present a significant loss of stiffness in

the region near the ultimate failure. Furthermore, the exponential evolution variable ( $m_i^\pm$ ) controls the rate at which damage occurs in the material, with lower values resulting in an earlier damage onset, subsequently presenting a more exponential curve. Contrarily, greater  $m_i^\pm$  values lead to a delay in the damage onset, resulting in a numerical curve shape that will only be influenced by the maximum damage control variable.

These variables are also calibrated for every experimental test performed in Chapter 3, and analogous simplifications to the ones mentioned in Section 3.1 were adopted.

## Regularisation coefficients

The last variables needed to calibrate the damage progression model are the numerical calibration inputs, namely (i) 1 mesh regularisation parameter ( $\alpha$ ), and (ii) 9 viscous regularisation coefficients ( $\eta_i^\pm$ ). The mesh regularisation parameter is a dimensional parameter that aims to smoothen the transition between the damage progression and the constant stress phase of the damage model 2.6 (*cf.* Section 2.3). This is a necessary approach since mesh sensitivity issues may occur where strong discontinuities exist [62], such as contacts, corners, or cracks. This parameter is computed using the compact tension test, as will be latter addressed in Section 4.2.3.

Additionally, the viscous regularisation parameters are introduced in order to avoid severe convergence difficulties in implicit analysis. These coefficients should be set to the highest possible value so they do not influence the numerical results (or the lowest that do not result in convergence problems).

## 4.2.2 Mesh sensitivity analysis

This preliminary study regarding the mesh sensitivity analysis, which aims to find a mesh that achieves a better compromise between the computational costs and the proximity with the experimental data, was performed for the I200-FC-W material for each test (except for the OAT test, for which the material I150-AP-W was used). With that in mind, meshes of (i) 1 mm, 0.5 mm, and 0.25 mm, for longitudinal and transverse tensile and compressive tests (Figure 4.1), (ii) 2 mm, 1 mm, and 0.5 mm for the *Iosipescu* test (Figure 4.2), and (iii) 3 mm, 1.5 mm, and 0.75 mm for the OAT test were used (similar to Figure 4.1 but with larger elements and without the “weak” region, as described in Section 4.1.2). Additionally, for the compact tension test, the mesh sensitivity analysis is only performed in the notch area, with meshes of 0.6 mm, 0.3 mm and 0.15 mm being used, as shown in Figure 4.3 (b). The remainder of the specimen is constituted by approximately cubic elements with 2.5 mm, which corresponds to half the thickness used in FE models in the case of the I200-FC-W material (Figure 4.3 (a)).

Figures 4.4 to 4.7 show the experimental and numerical results of the calibration process, and Table 4.1 summarises the main results. These results were obtained using the final calibration parameters of the material, which will be duly addressed in Section 4.3. All figures present grossly the same pattern - the use of a finer mesh results in a slightly higher maximum load (or analogously, higher maximum stress), which is a consequence of the smoother transition between the damage progression and the residual stress phase of the model. Moreover, refining the mesh practically does not influence

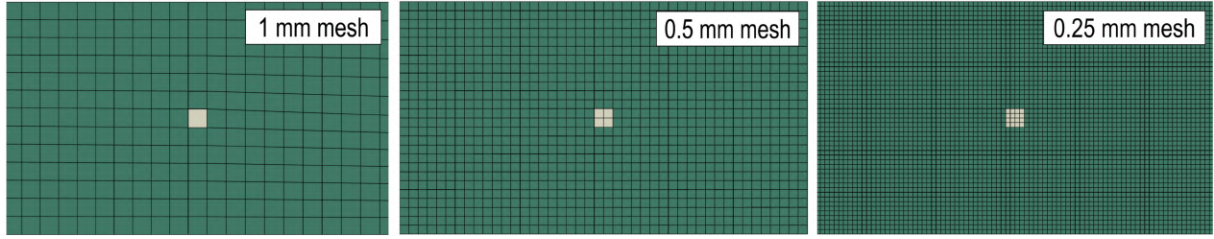


**Figure 4.1:** Mesh detail view near the weak region with different mesh sizes for a tensile test.

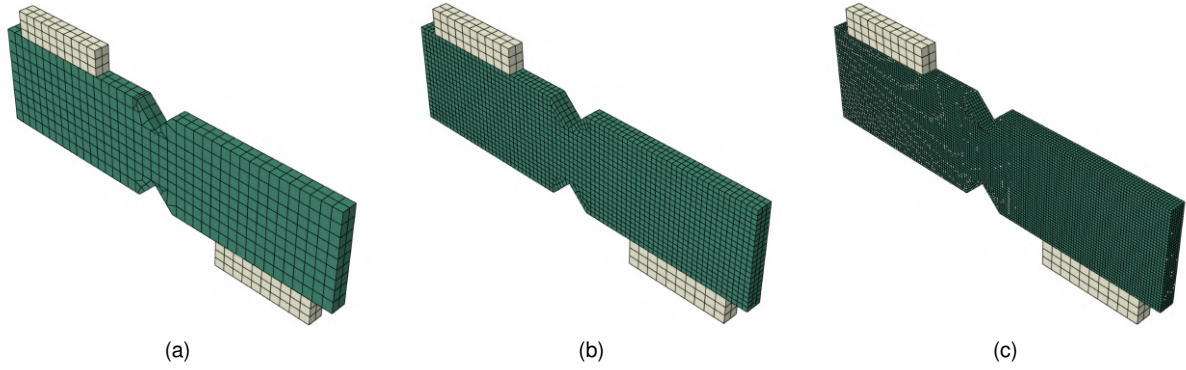


**Figure 4.2:** Different mesh sizes for a *losipescu* test: (a) 2 mm mesh; (b) 1 mm mesh; (c) 0.5 mm mesh.

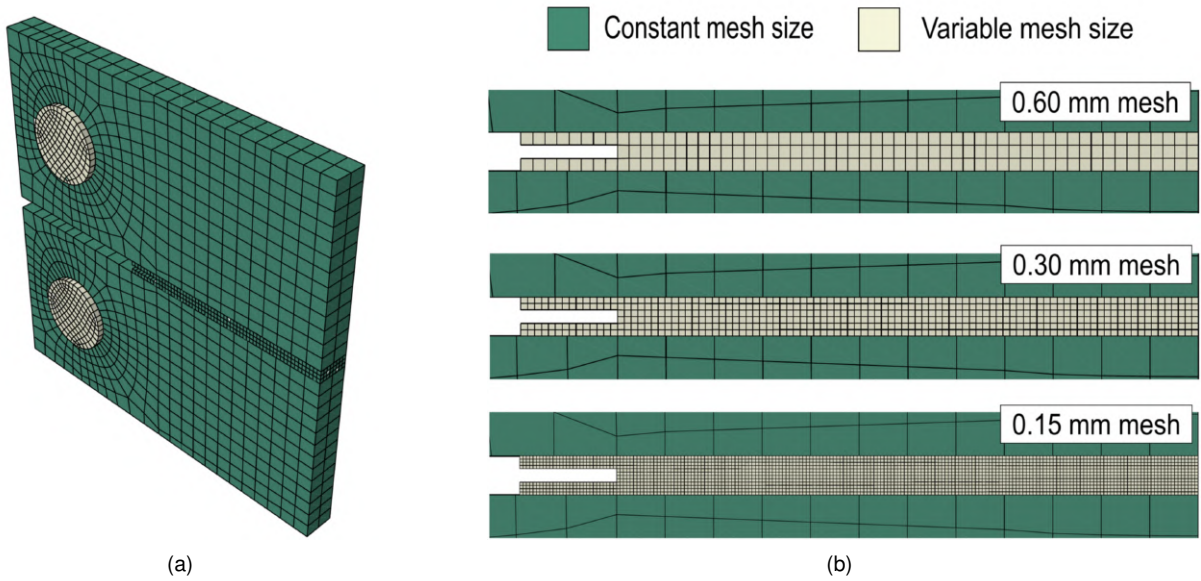


**Figure 4.3:** Different mesh sizes for a compact tension test: (a) general model overview; (b) mesh detail view.

the stiffness (elastic and shear moduli) of the numerical results for all tests, which proves that even the coarser meshes chosen are able to correctly characterise the material and test behaviour.

For both tensile tests, the maximum relative difference between the experimental average and the numerical results for the ultimate stress ( $S_{11}^+$  and  $S_{22}^+$ ) is -0.9% (registered for a mesh of 1 mm), as shown in Table 4.1. The 0.5 mm mesh for TT test presented convergence problems, therefore, the ultimate stress was not reached. Regarding the elastic moduli, all meshes produce a negligible relative difference to the experimental value for longitudinal tests, while for transverse tests, although the difference is

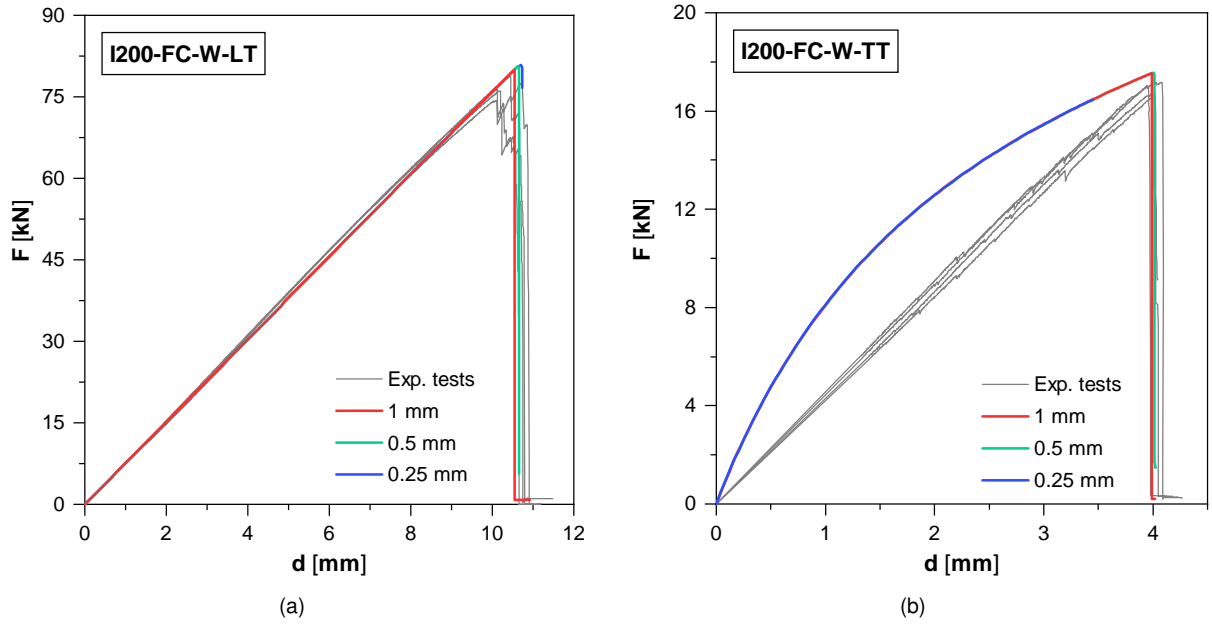


**Figure 4.4:** Experimental and numerical results of load vs. displacement curves of tensile tests for the I200-FC-W material with different mesh sizes: (a) longitudinal tension; (b) transverse tension.

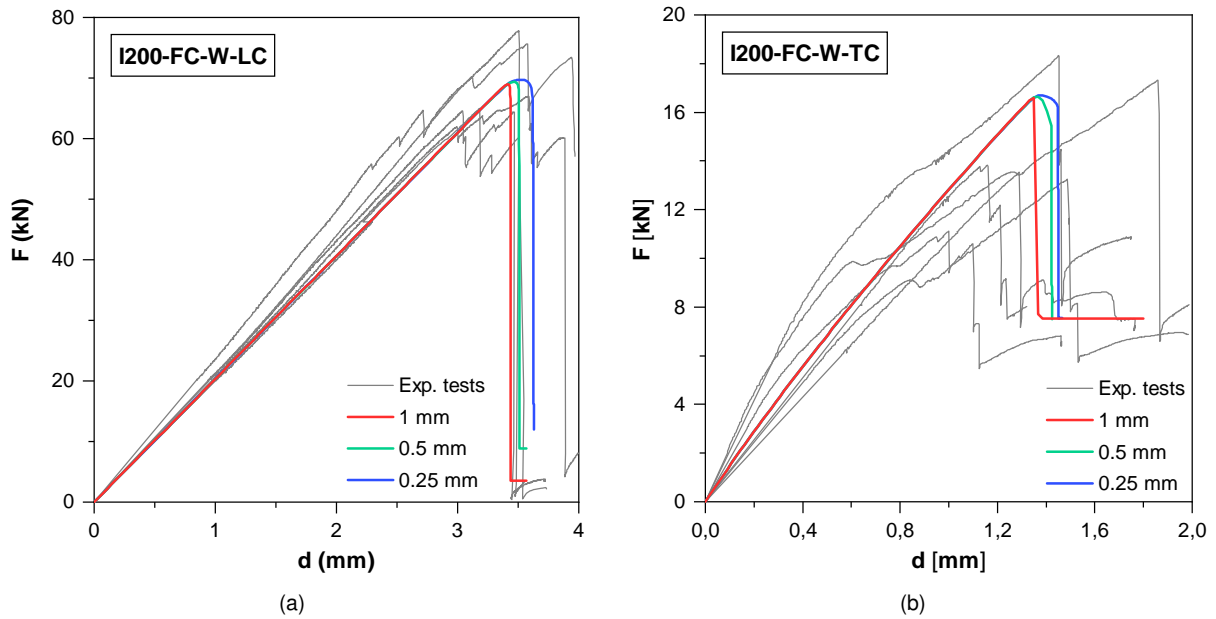


**Figure 4.5:** Experimental and numerical results of load vs. displacement curves of compressive tests for the I200-FC-W material with different mesh sizes: (a) longitudinal compression; (b) transverse compression.

higher than others (*cf.* Section 4.3.2), a maximum difference of 0.3 percentage points was registered. These results show that, for these tests, any mesh considered may be deemed satisfactory, although only the 1 mm mesh model is able fully capture the constant stress stage.

Concerning compressive results, Figures 4.5 (a) and (b) remarkably depict a greater difference in behaviour between meshes regarding the mesh regularisation stage compared to their tensile counterparts. This larger difference is associated with the size of the specimens, which means that changing the



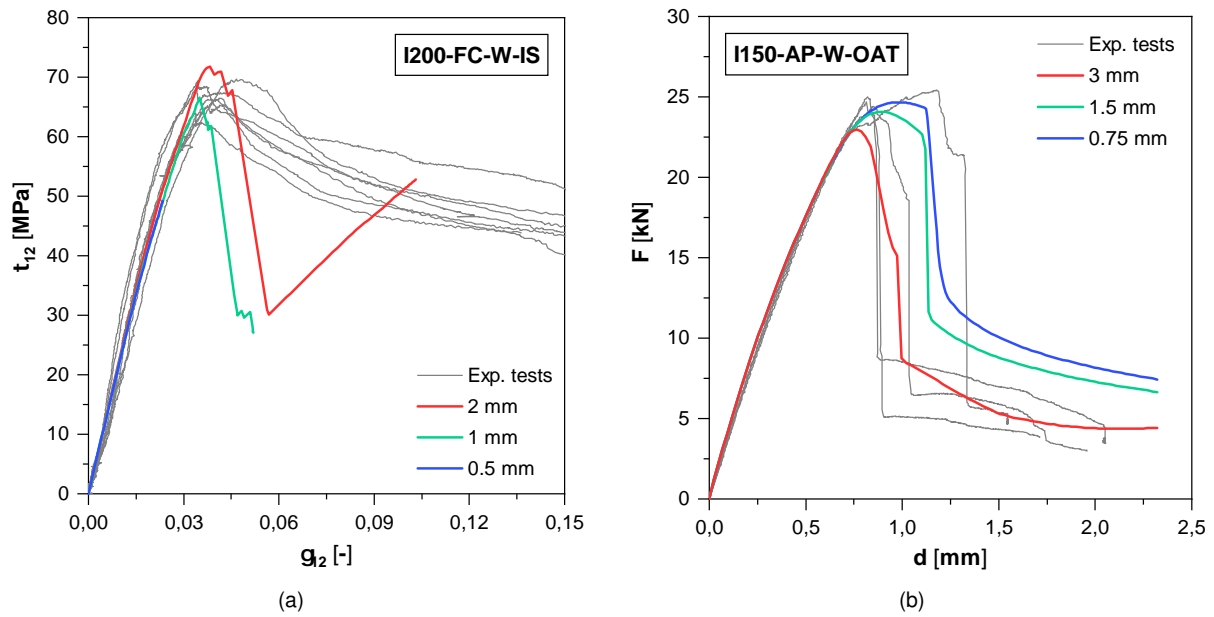


**Figure 4.6:** Experimental vs. numerical curves of in-plane shear tests with different mesh sizes: (a) stress vs. strain curve for I200-FC-W *Iosipescu* test; (b) load vs. displacement curve for I150-AP-W OAT test.

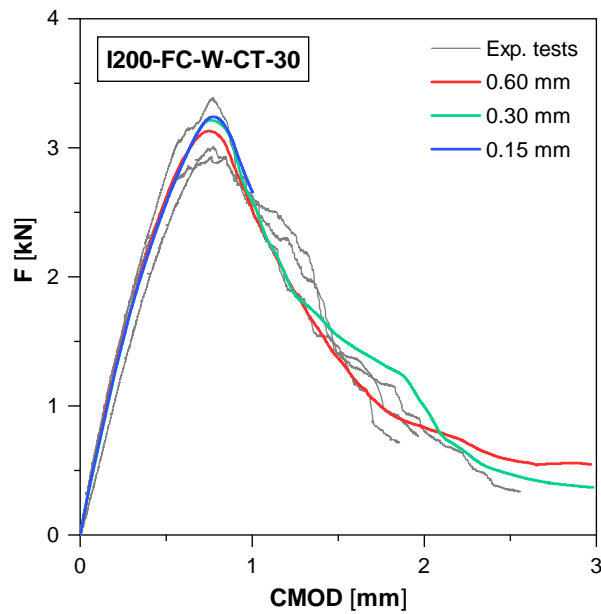


**Figure 4.7:** Experimental vs. numerical curves of compact tension tests with different mesh sizes.

mesh size from 1 to 0.5 mm is a greater change percentage-wise in a compressive test (specimens with 23 mm of free length) compared to a tensile one (specimens with  $\approx 200$  mm of free length). Table 4.1 again shows that refining the mesh produces a negligible influence in the numerical elastic moduli. As for the ultimate stresses, the relative difference for the LC test varies from -2.4% (1 mm mesh) to -1.3% (0.25 mm mesh) and from 13.6% (1 mm mesh) to 14.3% (0.25 mm mesh) in the TC test, representing changes of 1.1 and 0.7 percentage points, respectively, and demonstrating that, for these meshes, the element size presents very little influence in the final result.

For the *Iosipescu* test, the difference in numerical shear modulus ( $G_{12}$ ) obtained for the different meshes is also negligible, with a maximum of 1.3 percentage points registered between the coarser and the finer mesh used. Nonetheless, the results present a considerable relative difference when compared to the experimental ( $\approx 20\%$ ) and this will be addressed in Section 4.3.5. Regarding the ultimate shear stress ( $S_{12}$ ), a higher variability between meshes was registered. While a 2 mm mesh presents a relative difference of 7% relative to the experimental data, a 1 mm mesh only registers a -0.8% difference, representing a difference of 7.8 percentage points. Additionally, the finer mesh of 0.5 mm presented convergence problems, as exhibited in Figure 4.6 (a), thus not reaching failure. Nevertheless, the author considered that the difference between a 0.5 mm and a 1 mm mesh would not produce a significant change in the ultimate stress result, and therefore, a mesh of 1 mm was considered sufficiently accurate.

The  $10^\circ$  off-axis tensile test's results are summarised in Figure 4.6 (b) and Table 4.1. As in other tests, the difference between meshes regarding the shear modulus is negligible. As for the ultimate shear strength, altering the mesh from 3 mm to 1.5 mm produces a relative difference of 4.6 percentage points, and refining it to a further 0.75 mm decreases this difference to 2.5 percentage points. In view of these results, a mesh of 1.5 mm was deemed accurate enough.

Test	Property	1 mm mesh		0.5 mm mesh		0.25 mm mesh	
		Value	$\Delta$ (%)	Value	$\Delta$ (%)	Value	$\Delta$ (%)
Longitudinal tension	$E_{11}$ [GPa]	29.6	0.0	29.6	0.0	29.6	0.0
	$S_{11}^+$ [MPa]	319.7	-0.9	322.3	-0.1	323.3	0.2
Transverse tension	$E_{22}$ [GPa]	16.3	-7.5	16.2	-7.7	16.2	-7.8
	$S_{22}^+$ [MPa]	70.1	-0.9	70.2	-0.7	-*	-
Longitudinal compression	$E_{11}$ [GPa]	29.8	0.6	29.8	0.6	29.8	0.6
	$S_{11}^-$ [MPa]	431.0	-2.4	433.6	-1.8	435.8	-1.3
Transverse compression	$E_{22}$ [GPa]	15.3	-13.3	15.3	-13.3	15.3	-13.3
	$S_{22}^-$ [MPa]	138.2	13.6	138.7	14.1	139.1	14.3
<i>Iosipescu</i>	2 mm mesh			1 mm mesh		0.5 mm mesh	
	$G_{12}$ [GPa]	2.33	-19.4	2.30	-20.3	2.29	-20.7
	$S_{12}$ [MPa]	71.8	7.0	66.6	-0.8	-*	-
	3 mm mesh			1.5 mm mesh		0.75 mm mesh	
$10^\circ$ Off-axis tensile	$G_{12}$ [GPa]	4.59	-2.5	4.59	-2.4	4.59	-2.5
	$S_{12}$ [MPa]	19.7	-3.5	20.6	1.1	21.1	3.6
Compact tension	0.6 mm mesh			0.3 mm mesh		0.15 mm mesh	
	$K$ [kN/mm]	6.10	5.9	6.04	5.0	5.99	4.1
	$F_{\max}$ [kN]	3.13	0.6	3.21	3.3	3.24	4.4

**Table 4.1:** Main results of I200-FC-W (and I150-AP-W for OAT test) and relative difference to the experimental average for different meshes.

\* Failure was not reached.

Finally, regarding the compact tension test, the results depicted in Figure 4.7 and summarised in Table 4.1 show again that the stiffness fluctuation between meshes is negligible. As for the maximum load, a 0.6 mm mesh produces a value of 3.13 kN, only 0.6% higher than the experimental average, while mesh sizes of 0.3 and 0.15 mm produce relative differences of 3.3% and 4.4%, respectively. Refining the mesh, although increasing the difference to the experimental average, decreases the relative difference

between numerical results, as expected. Since these differences are small and coarser meshes allow for better convergence, a mesh size of 0.6 mm was considered adequate.

With this in mind, all results presented hereafter were always obtained using a mesh of (i) 1 mm for tensile (except the OAT), compressive and *Iosipescu* tests, (ii) 1.5 mm for 10° off-axis tensile tests, and (iii) 0.6 mm for compact tension tests.

### 4.2.3 Regularisation coefficients sensitivity analysis

As duly described in [3], the mesh and viscous regularisation parameters are implemented in order to guarantee a correct use of the damage progression model in an FE analysis. However, even if these inputs have only a numerical application and do not carry any physical meaning, their introduction may also produce different results for the same material (*i.e.* for the same mechanical properties introduced in the model). For this reason, and as a confirmation of the early studies [3, 16], the author decided to perform a short analysis on the implications these variables may have on the calibration curve fitting process. For this purpose, the longitudinal tensile and compact tension tests of the I200-FC-W material were chosen, with the results obtained presented in Figures 4.8 and 4.9.

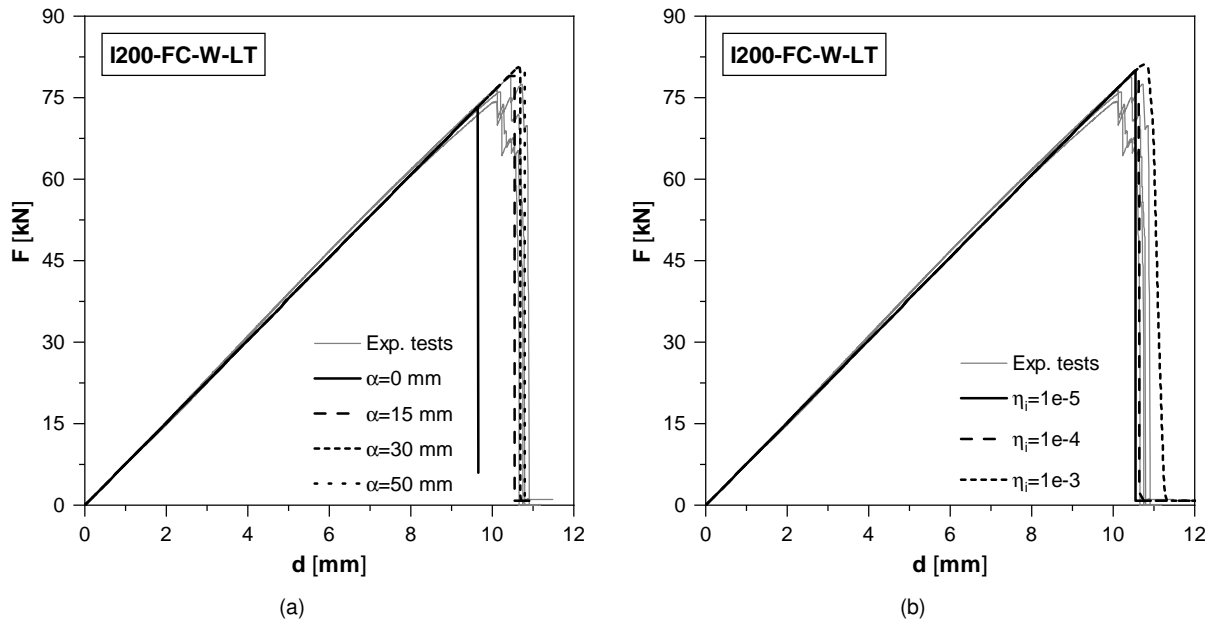


**Figure 4.8:** Sensitivity analysis of regularisation factors for I200-FC-W-LT test: (a) varying  $\alpha$  with fixed  $\eta_i = 1 \times 10^{-5}$ ; (b) varying  $\eta_i$  with fixed  $\alpha = 15$  mm.

Regarding the longitudinal tensile test, Figure 4.8 (a) shows that the adoption of a null mesh regularisation factor ( $\alpha = 0$ ) decreases significantly the predicted failure load of the numerical analysis, as expected [3]. Nonetheless, the effect of varying this coefficient between 15 mm and 50 mm only produces a slight delay (and consequent increase) in reaching the failure load, which can be neglected. As such, for Sections 4.3.1 to 4.3.6 of the calibration phase of this study, a mesh regularisation factor of  $\alpha = 15$  mm will be used, assuming the differences for other tests follow the same trend.

However, for the compact tension test, due to the existence of sharp corners that lead to a high

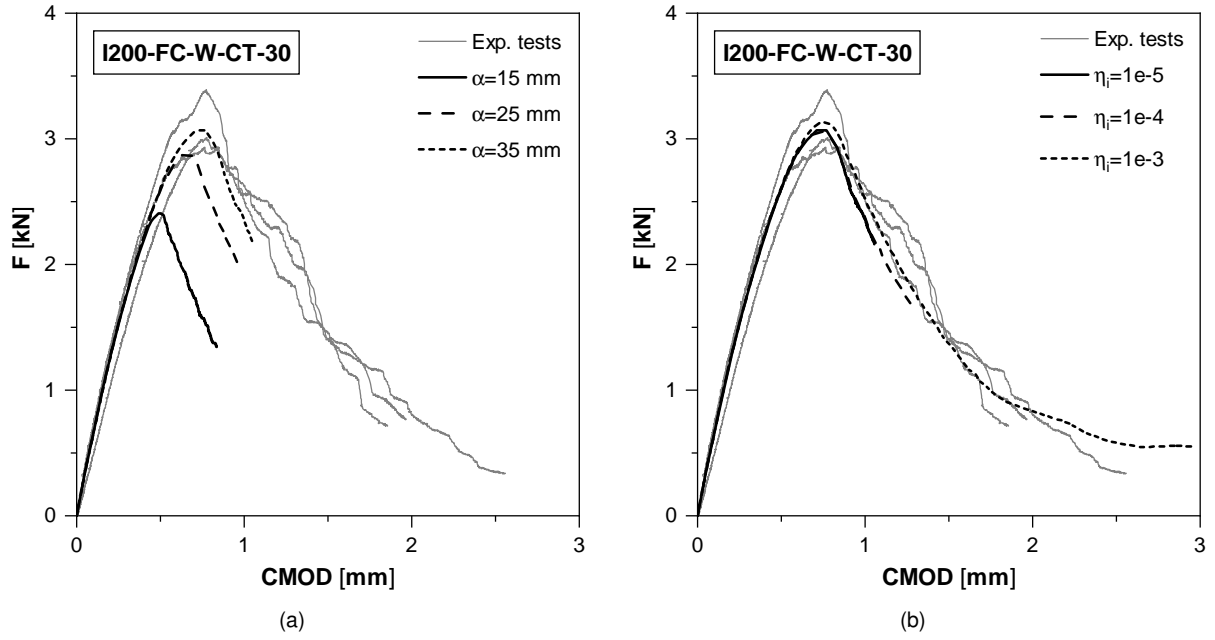


**Figure 4.9:** Sensitivity analysis of regularisation factors for I200-FC-W-CT-30 test: (a) varying  $\alpha$  with fixed  $\eta_i = 1 \times 10^{-5}$ ; (b) varying  $\eta_i$  with fixed  $\alpha = 30$  mm.

concentration of stresses in the notch region, the effect of varying the mesh regularisation parameter is more noticeable, as shown in Figure 4.9 (a). For this reason, the author decided to include the compact tension test as an additional test required for the calibration of the damage model (*cf.* Section 4.3.7) in order to correctly calibrate the mesh regularisation input  $\alpha$ , unlike what was done in [3, 16].

With relation to the viscous regularisation factor ( $\eta_i$ ), Figures 4.8 (b) and 4.9 (b) depict its influence on the results. For the longitudinal tensile test, varying this factor between  $1 \times 10^{-5}$  and  $1 \times 10^{-4}$  produces an almost negligible change while increasing it further to  $1 \times 10^{-3}$  leads to a similar effect to increasing the mesh regularisation factor - a delay in reaching the failure load. Additionally, the transition between this stage and the constant stress stage is also visibly delayed for an  $\eta_i = 1 \times 10^{-3}$ . With this in mind, and because it was considered important to accurately depict the behaviour of the mechanical characterisation calibration tests, the smaller value of  $\eta_i = 1 \times 10^{-5}$  was adopted for the early calibration phase.

As for the compact tension test, the variation of  $\eta_i$  produces the same effect regarding the maximum load, but has a greater influence on the results after in the softening stage. Figure 4.9 (b) highlights that, even though for  $\eta_i = 1 \times 10^{-5}$  the load vs. CMOD curve contains all the necessary information to understand the numerical test's behaviour, using a parameter  $\eta_i = 1 \times 10^{-3}$  allows for higher displacements to be reached, resulting in a more complete numerical failure mode (*cf.* Section 4.3.7) while having much less computational cost. For this reason, the compact tension test (and all application tests of the same nature, such as wide compact tension and compact compression tests) was modelled with a viscous regularisation parameter of  $\eta_i = 1 \times 10^{-3}$ .

## 4.3 Results and discussion

The numerical results obtained for every test and material are compared with experimental data in two forms: (i) in stress vs. strain curves the behaviour until failure is analysed and the main values are compared, and (ii) in load vs. displacement graphics, the failure and post-failure behaviour is compared. This method is adopted because of the irregular experimental strain readings after failure region, as already mentioned in Chapter 3. Additionally, in the load vs. displacement curves, the curves' slope is adjusted for an easier interpretation since only the failure and post-failure behaviour is being compared in this graphics. Moreover, to better summarise the information presented in all graphics, the experimental results were presented in a scatter form where the two curves that defined the upper and lower bounds of the experimental data were used (occasionally, when needed, three curves were used instead of two). As a further note, since the S120-AP material has no web and flange distinction, its results were presented in graphics related to web plates.

The final calibration parameters are also shown in tables for every test and material. Since for the flange materials most test data was unavailable, the calibration inputs used for the web plates were adopted. Furthermore, when failure modes are presented, the entire specimens are shown by replicating the results over the symmetry planes.

### 4.3.1 Longitudinal tensile tests

As verified earlier in the experimental chapter, longitudinal tensile tests are characterised by a simple linear behaviour. When the ultimate load is reached, the material experiences brittle failure with a sharp decrease in load and a final stage of very low residual stress.

With this in mind, the damage progression control inputs for the longitudinal tensile properties were set to  $d_{1,max}^+ = 0.001$  and  $m_1^+ = 10$  for all materials. Moreover, the residual control inputs were straightforwardly computed using equations 4.1 and 4.2. These values are summarised in Table 4.2.

Figure 4.10 show a good agreement between the experimental data and the numerical simulations. For all materials, the numerical curves are within or very near the bounds of the experimental scatter. Furthermore, the elastic modulus  $E_{11}$  and ultimate stress  $S_{11}^+$  values obtained with the numerical models and their relative difference to the experimental average are also compiled in Table 4.2. For all materials, the difference between numerical and experimental elastic modulus for this test is negligible, and for the ultimate stress, a maximum relative difference of 7.2% for S120-AP was obtained. The flange plate curves are omitted since they are similar to the results of the web.

### 4.3.2 Transverse tensile tests

Transverse tensile tests, contrarily to their longitudinal counterparts, present a bi-linear behaviour, as explained in Section 3.1.2. For this reason, and to facilitate the curve-fitting process, two decisions were made: (i) the transverse elastic modulus ( $E_{22}$ ) should be retrieved from the curve's first linear branch (the experimental results presented in Table B.1 already have this into consideration), and (ii) the input

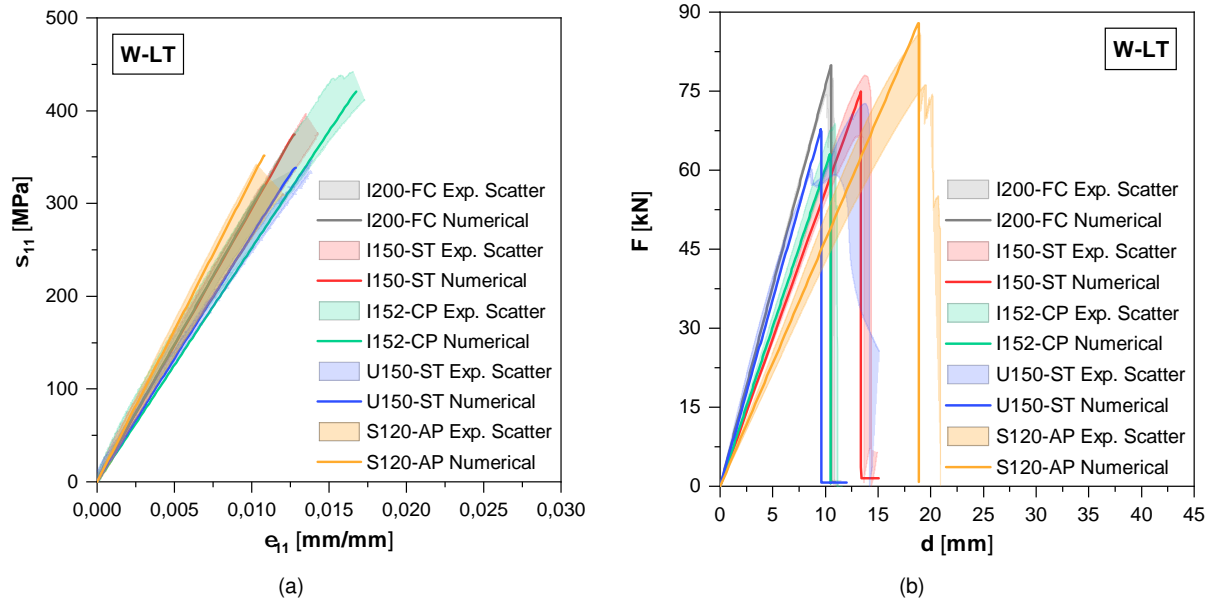


**Figure 4.10:** Longitudinal tensile tests - experimental and numerical results for web plates: (a) stress vs. strain curves; (b) load vs. displacement curves.

Material		$d_{1,max}^+$	$m_1^+$	$\epsilon_{11,u}^+$	$r_{11}^+$	$E_{11}$ [GPa]		$S_{11}^+$ [MPa]	
						Value	$\Delta$ (%)	Value	$\Delta$ (%)
I200-FC	W	0.001	10	0.011	0.01	29.6	0.0	319.7	-0.9
	F			0.009		35.3	0.0	311.4	-1.7
I150-ST	W	0.001	10	0.013	0.02	29.4	0.0	374.4	-0.5
	F			0.012	0.01	33.9	0.0	397.3	3.1
I152-CP	W	0.001	10	0.017	0.01	25.2	0.0	420.6	-1.3
	F			0.018		26.8	0.0	472.9	1.3
U150-ST	W	0.001	10	0.013	0.01	26.6	0.0	338.7	-2.4
	F			0.014		27.3	0.0	374.0	0.1
S120-AP	W	0.001	10	0.011	0.01	32.7	0.0	349.8	7.2

**Table 4.2:** Longitudinal tensile tests - calibration inputs and summary of main results.

$S_{22}^+$  used should not be the ultimate stress values shown in Table B.1 (*cf.* Appendix B) but the stress corresponding to the end of the first linear branch of the material response (*i.e.* transverse tensile “yield” stress corresponding to the end of the proportionality limit  $S_{22,y}^+$  [3]). This “yield” stress was computed as the intersection between the two linear curves that fit the initial and final stage of the bi-linear transverse tensile test curves. Nevertheless, the ultimate stress  $S_{22}^+$  is still used for experimental vs. numerical comparisons. Table 4.3 summarises the results obtained for each material. It should also be mentioned that using the ultimate stresses as input should also lead to similar results, but the author experienced difficulties in applying this process for one of the materials studied and decided to use this approach instead.

Taking all this into consideration, the damage progression control inputs were duly calibrated, resulting in values between 0.6 and 0.8 for  $d_{2,max}^+$  and 0.8 and 1 for  $m_2^+$ , reflecting the more exponential behaviour when comparing to the longitudinal tensile test. Furthermore, the limit strains ( $\epsilon_{22,u}^+$ )

were retrieved directly from the stress vs. strain curves as explained earlier, and the residual strength inputs ( $r_{22}^+$ ) range from 0.01 to 0.05. Table 4.3 presents all calibration inputs used.

The stress vs. strain numerical curves obtained show good agreement with the experimental data, as shown in Figure 4.11 (a). By analysing the main results summarised in Table 4.3, it can be seen that the numerical ultimate stress has a maximum deviation of 1.6% relative to the experimental average, registered for I152-CP material. As for the transverse elastic modulus, the higher relative differences (a maximum of -13% was registered, for I150-ST) can be attributed to the high sensitivity to small deviations of the interval for which these values were retrieved, both experimentally and numerically. Additionally, Figure 4.11 (b) also depicts good agreement regarding the sudden drop in stiffness after (brittle) failure and the constant stress stage.

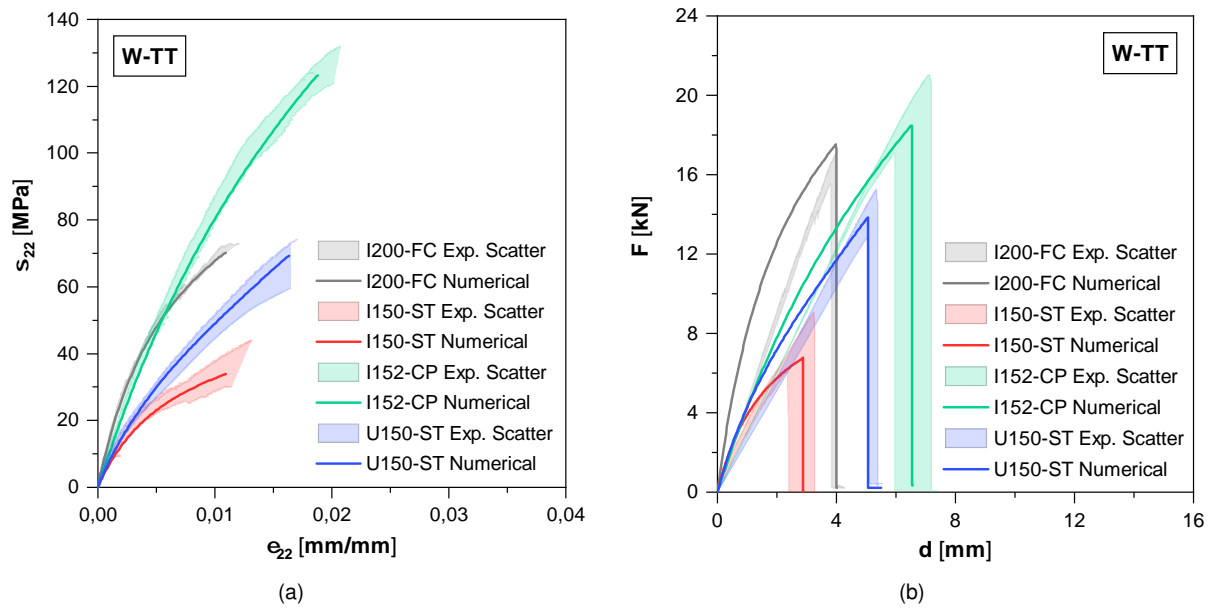


**Figure 4.11:** Transverse tensile tests - experimental and numerical results for web plates: (a) stress vs. strain curves; (b) load vs. displacement curves.

Material	$S_{22,y}^+$ [MPa]	$d_{2,max}^+$	$m_2^+$	$\epsilon_{22,u}^+$	$r_{22}^+$	$E_{22}$ [GPa]		$S_{22}^+$ [MPa]	
						Value	$\Delta$ (%)	Value	$\Delta$ (%)
I200-FC-W	41.3	0.8	0.8	0.011	0.02	16.7	-5.2	70.1	-0.9
I150-ST-W	20.0	0.8	0.8	0.011	0.01	7.3	-13.0	33.9	0.1
I152-CP-W	69.6	0.6	1	0.019	0.03	10.5	-3.1	123.2	1.6
U150-ST-W	21.6	0.6	0.8	0.017	0.05	8.2	-6.5	69.2	-0.4

**Table 4.3:** Transverse tensile tests - calibration inputs and summary of main results.

### 4.3.3 Longitudinal compressive tests

Longitudinal compressive tests follow the same trend as their tensile counterparts, with a linear behaviour until brittle failure occurs, followed by a low constant stress stage.

Given this behaviour, Table 4.4 presents all calibration input variables, with damage progression control inputs set to  $d_{1,max}^- = 0.001$  and  $m_1^- = 10$ , and limit strains and residual strengths computed with equations 4.1 and 4.2, respectively.

The results obtained are summarised in Figures 4.12 (a) and (b) and Table 4.4. Once again, numerical results show an excellent agreement with experimental data, with the stress vs. strain curves being inside the envelope defined by the experimental scatter (Figure 4.12 (a)), except for S120-AP, and the residual stress being correctly predicted (Figure 4.12 (b)). Moreover, excluding S120-AP, the maximum relative difference between the experimental average and the numerical prediction was 4% for the ultimate stress and 4.9% for the elastic modulus, registered for I150-ST-W.

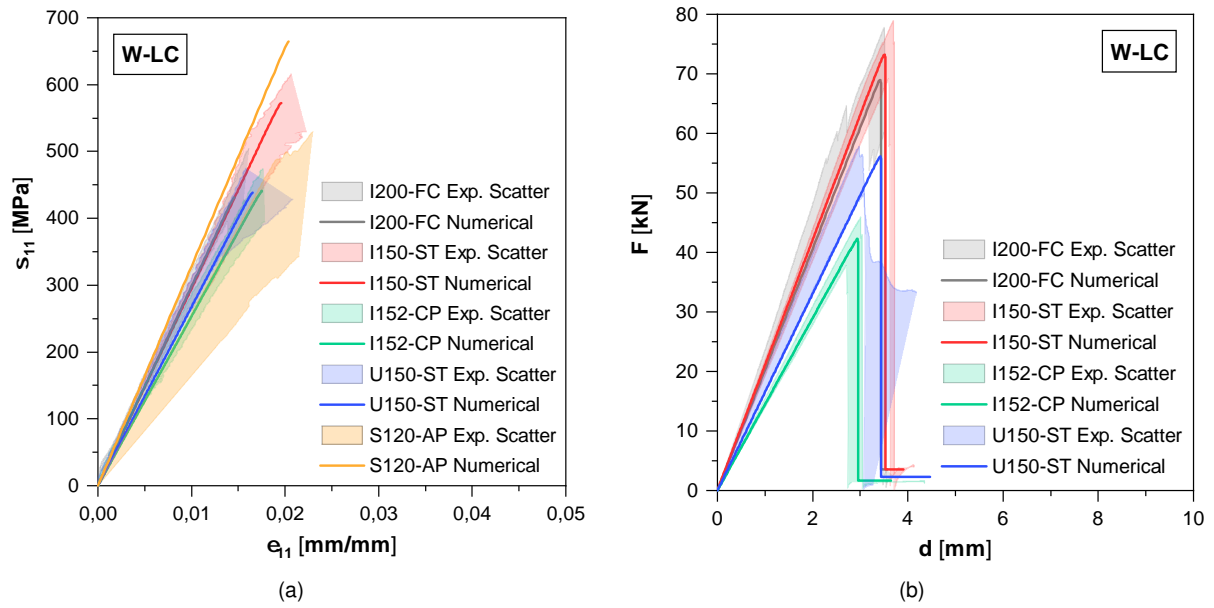


**Figure 4.12:** Longitudinal compressive tests - experimental and numerical results for web plates: (a) stress vs. strain curves; (b) load vs. displacement curves.

Material	$d_{1,max}^-$	$m_1^-$	$\epsilon_{11,u}^-$	$r_{11}^-$	$E_{11}$ [GPa]		$S_{11}^-$ [MPa]	
					Value	$\Delta$ (%)	Value	$\Delta$ (%)
I200-FC-W	0.001	10	0.015	0.05	29.8	-0.1	431.0	-2.4
I150-ST-W	0.001	10	0.020	0.05	29.5	4.9	572.3	4.0
I152-CP-W	0.001	10	0.018	0.04	25.3	2.9	440.7	0.9
U150-ST-W	0.001	10	0.017	0.04	26.7	3.8	438.4	-2.7
S120-AP	0.001	10	0.021	0.05	32.8	54.9	664.7	52.8

**Table 4.4:** Longitudinal compressive tests - calibration inputs and summary of main results.

As for S120-AP, the high relative differences compared to experimental data of 55% and 53% for  $E_{11}$  and  $S_{11}^-$ , respectively, are associated with the combination of (i) the damage progression model only considering one elastic modulus for both tensile and compressive stress states (*cf.* Section 4.2.1), and (ii) the different standard used to obtain the experimental results. As explained in Section 3.1.3, this different test standard produced less trustworthy results than CLC tests, resulting in an underestimation



of the longitudinal compressive modulus, a higher difference between tensile and compressive elastic moduli and consequently higher relative differences between numerical and experimental results.

#### 4.3.4 Transverse compressive tests

The transverse compressive tests exhibit the most intricate experimental results. As described in Section 3.1.3, some materials presented linear behaviour, while others exhibited a more exponential curve, until brittle failure occurred. After failure, and due to the CLC setup used, the constant stress stage is higher than other tests. Figures 4.13 (a) and (b) show the experimental vs. numerical results and Table 4.5 summarise the main results obtained as well as the calibration parameters used in each material and discussed below.

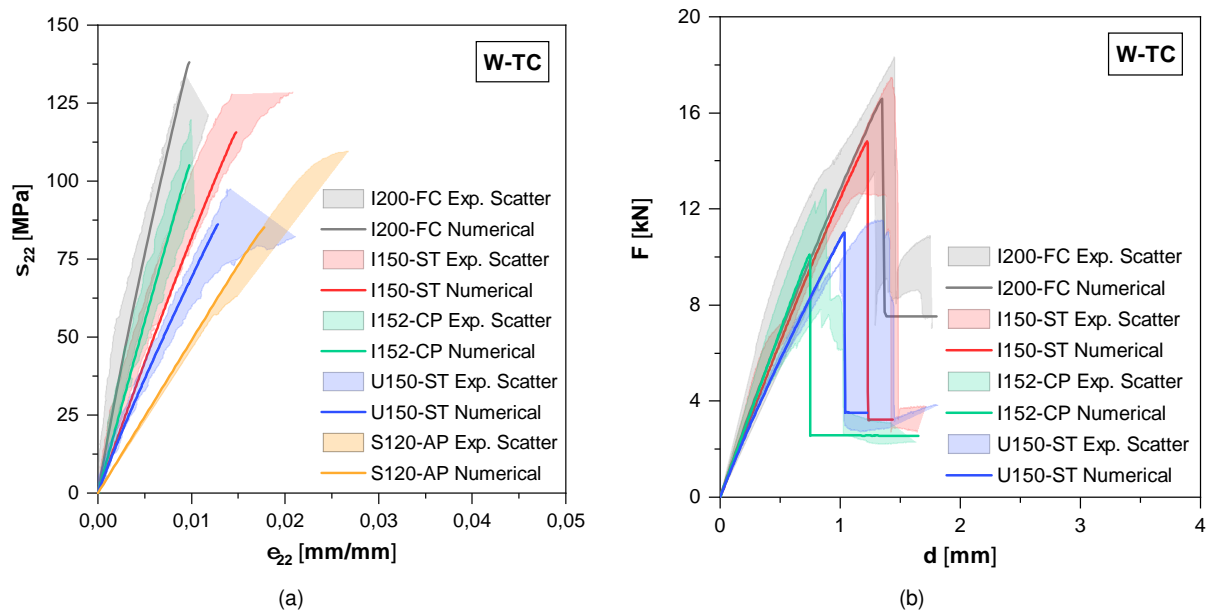


**Figure 4.13:** Transverse compressive tests - experimental and numerical results for web plates: (a) stress vs. strain curves; (b) load vs. displacement curves.

Material	$d_{2,max}^-$	$m_2^-$	$\epsilon_{22,u}^-$	$r_{22}^-$	$E_{22}$ [GPa]		$S_{22}^-$ [MPa]	
					Value	$\Delta$ (%)	Value	$\Delta$ (%)
I200-FC-W	0.4	0.7	0.010	0.50	15.3	40.7	138.2	13.6
I150-ST-W	0.4	2	0.015	0.20	8.4	-34.6	115.7	-5.9
I152-CP-W	0.2	5	0.010	0.25	11.0	-2.9	105.1	0.9
U150-ST-W	0.4	0.5	0.013	0.32	7.4	5.3	86.1	3.1
S120-AP	0.5	10	0.018	0.20	4.9	1.1	85.1	-4.3

**Table 4.5:** Transverse compressive tests - calibration inputs and summary of main results.

For the I200-FC material both bi-linear and linear behaviour was registered experimentally, as seen by the upper and lower bounds, respectively, represented in Figure 4.13 (a). Furthermore, since the second linear stage's slope of the bi-linear specimens was similar to the linear curves' slope, the

author decided to use this section of the curves to compute the experimental transverse compressive elastic modulus ( $E_{22}^-$ ), as explained in Section 3.1.3. However, this increased the difference between the experimental transverse elastic modulus in tension and compression ( $E_{22}^+ = 17.6$  GPa and  $E_{22}^- = 10.9$  GPa, Table B.1, *cf.* Appendix B), leading to a necessity in calibrating the damage control input variables in such a way that the main numerical results (*i.e.*  $E_{22}$  and  $S_{22}$ ) would not be entirely compromised, resulting in a slight more exponential numerical curve than ideal. Overall, the final damage progression control inputs were set to  $d_{2,max}^- = 0.4$  and  $m_2^- = 0.7$  leading to relative differences of 41% for the transverse elastic modulus and 14% for the ultimate transverse stress. Moreover, this material registered a very high residual strength, as shown in Figure 4.13 (b), with this input being set to  $r_{22}^- = 0.50$  (Table 4.5).

For I150-ST, with experimental results predominantly exponential, the experimental transverse compressive elastic modulus was retrieved in the initial phase of the curve, resulting in a higher difference between tensile and compressive elastic moduli ( $E_{22}^+ = 8.41$  GPa and  $E_{22}^- = 12.9$  GPa, Table B.1, *cf.* Appendix B). This led to a compromise in the damage calibration inputs, with  $d_{2,max}^- = 0.4$  and  $m_2^- = 2$  values adopted, resulting in a slightly more linear numerical curve than the experimental ones. The final results registered relative differences of -35% and -5.9% for elastic modulus and ultimate stress, respectively.

The calibration of I152-CP and U150-ST was more straightforward since the experimental tensile and compressive elastic moduli of these materials were less discrepant. While I152-CP presented a consistently linear behaviour, U150-ST exhibited a slightly exponential experimental curve. For this reason, the damage progression control inputs were set to  $d_{2,max}^- = 0.2$  and  $m_2^- = 5$  for I152-CP, and  $d_{2,max}^- = 0.4$  and  $m_2^- = 0.5$  for U150-ST. The highest relative difference was registered for U150-ST, with 5.3% elastic modulus deviation.

Finally, the calibration of the S120-AP material was performed using the experimental transverse compressive modulus as input ( $E_{22}$ ) instead of the tensile modulus, due to the nonexistent experimental data regarding a transverse tensile test. The damage progression control inputs were set to  $d_{2,max}^- = 0.5$  and  $m_2^- = 10$ , resulting in small relative differences of 1.1% for the elastic modulus and -4.3% for the ultimate strength.

#### 4.3.5 *Iosipescu* tests

As mentioned earlier in Section 3.1.4, most materials' in-plane shear properties were determined using *Iosipescu* tests. The experimental stress vs. strain curves scatter is presented for web and flange plates in Figures 4.14 (a) and (b), respectively, along with the numerical curves, while the main results and calibration parameters are summarised in Table 4.6.

The calibration inputs for this test were similar for all materials, with  $d_{4,max}$  varying between 0.90 and 0.99, and an  $m_4 = 5$  being adopted. Due to the limitations of the test setup, ultimate failure was not reached. Thereafter, both residual strength control inputs were set to  $r_{12} = 1$ , that is, the residual strength stage does not occur in the numerical modelling.

Figures 4.14 (a) and (b) show a similar behaviour between the experimental scatter and the numerical results for all materials tested. However the shear moduli are constantly underestimated, with relative differences between -20% and -36% for I200-FC and U150-ST, respectively. This discrepancy is irrespective of the calibration parameters used, since the shear modulus is obtained for very low strains where the curve is linear and there is no input influence. This difference is probably associated with the experimental methodology followed to compute the shear moduli, which was replicated in the numerical simulation. As for the ultimate shear strength, the relative differences obtained are small, except for I150-ST, which presents the higher difference of 8.7% for the flange plate. The numerical ultimate shear strength could not be lowered any further due to convergence problems for higher inputs of  $d_{4,max}$ .

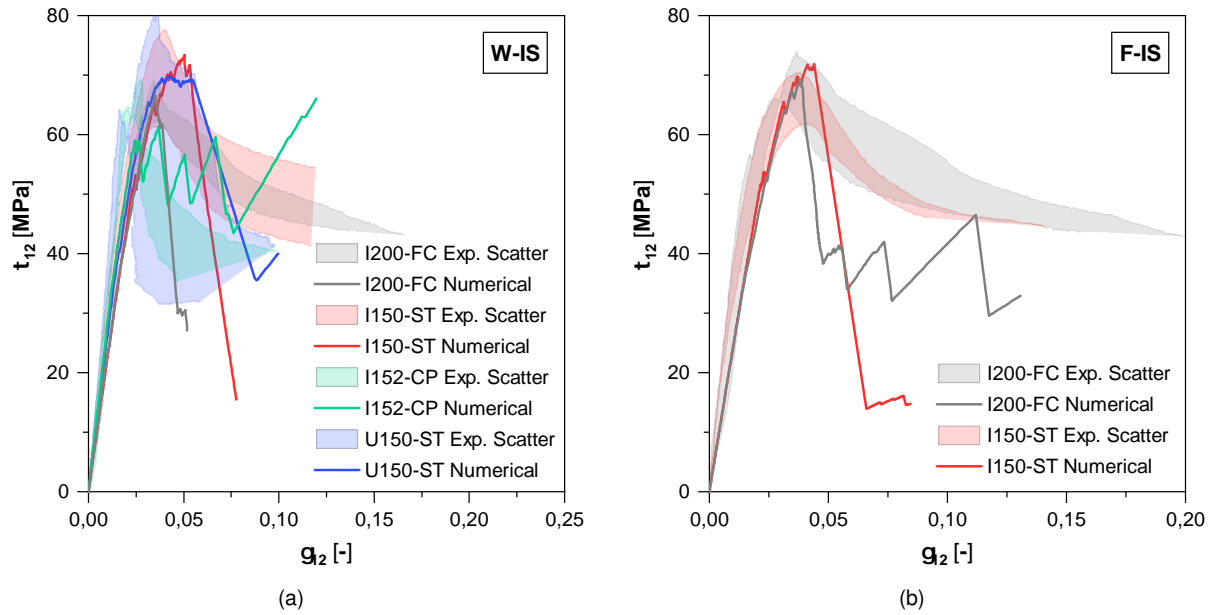


**Figure 4.14:** *losipescu* tests - stress vs. strain curves of experimental and numerical results: (a) web plates; (b) flange plates.

Material		$d_{4,max}$	$m_4$	$\gamma_{12,u}$	$r_{12}$	$G_{12}$ [GPa]		$S_{12}$ [MPa]	
						Value	$\Delta$ (%)	Value	$\Delta$ (%)
I200-FC	W	0.95	5	1	1	2.30	-20.3	66.6	-0.8
	F					2.44	-20.0	69.3	0.0
I150-ST	W	0.99	5	1	1	2.25	-29.1	73.3	5.0
	F	0.98				2.45	-29.9	71.9	8.7
I152-CP-W		0.90	5	1	1	2.82	-33.5	66.0	1.0
U150-ST-W		0.95	5	1	1	2.68	-35.7	69.9	-1.3

**Table 4.6:** *losipescu* tests - calibration inputs and summary of main results.

The main failure mode of the *losipescu* test is the formation of a crack along the narrower section of the specimen due to shear stresses. However, some specimens also show signs of crushing in the v-notch sections, as explained in Section 3.1.4. Numerical analysis shows that the model is able to reproduce both types of failure. Figures 4.15 (a) and (b) show the failure modes from the web plates for materials I200-FC and U150-ST, respectively. While the failure of the first is exclusively due to shear

stresses, U150-ST depicts significant degradation of the transverse compressive modulus due to compressive stresses in the loaded and fixed regions of the specimen (right top and bottom left, respectively) with this degradation starting near the v-notch and propagating through the principal direction. This latter failure mode's behaviour is also captured in the stress vs. strain curve in Figure 4.14 (a), with the U150-ST curve exhibiting a stage where the load is practically constant (and at its peak) for strains between approximately 0.04 and 0.06, then followed by the shear failure with the decrease in shear stress. Furthermore, I152-CP and I150-ST present a mixed case, with more relevant shear failure than compressive failure, but the latter is also present.

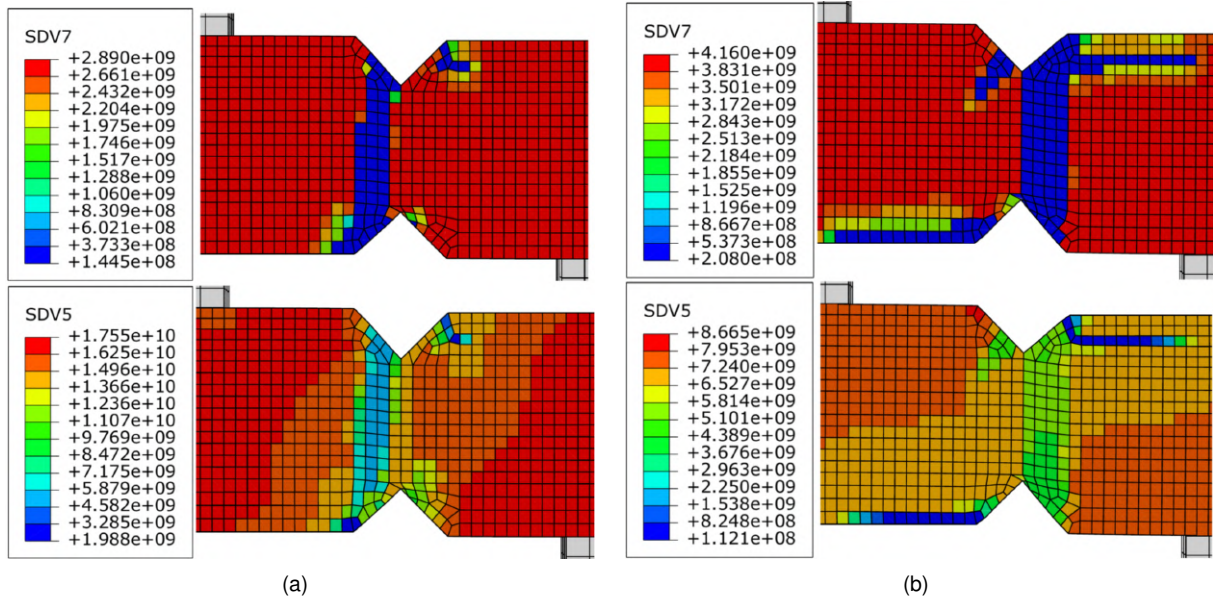


**Figure 4.15:** Failure of a numerical *losipescu* test and degradation of main variables -  $G_{12}$  (SDV7) and  $E_{22}$  (SDV5) in Pa for: (a) I200-FC-W; (b) U150-ST-W.

### 4.3.6 10° Off-axis tensile tests

The 10° Off-axis tensile test was performed for the I150-AP material as an alternative to the *losipescu* test, as mentioned in Section 3.2. Additionally, data for this test was also available for the S120-AP material, with its shear modulus obtained exclusively from the OAT test and not the *losipescu*, contrarily to I150-AP. Figures 4.16 (a) and (b) show the experimental and numerical curves obtained, and Table 4.7 summarises the main results and the calibration inputs used.

Both stress vs. strain curves are similar, with an initial linear curve that progressively decreases in slope, becoming more exponential. For this reason, a similar maximum damage parameter ( $d_{A,max}$ ) to the *losipescu* test was used, with values of 0.95 for I150-AP and 0.97 for S120-AP. However, the exponential control input had to be set to lower values of 0.4 and 0.3 for I150-AP and S120-AP, respectively, in order to correctly depict the curves' behaviour. The relative differences obtained registered a maximum of -2.4% for the shear modulus and 1.1% for the ultimate shear stress.

Even though these calibration inputs allow for a good numerical results regarding stress vs. strain curves (Figure 4.16 (a)), there is an overestimation of the residual stress in the after failure behaviour

stage, as exhibited in Figure 4.16 (b). This overestimation, although present in both materials, is clearly more visible in S120-AP and occurred because the experimental test was stopped immediately after failure, not allowing for the residual stage to develop. In the numerical models, the parameter  $r_{12}$ , although set to 0.01, leads to a residual strength of  $\approx 40\%$  for both materials. This effect can be associated with the lack of degradation of the elastic moduli in other directions, such as the longitudinal direction, which also plays a role in failure. Moreover, the accentuated decrease in stiffness near the maximum load and before total failure shows that the damage progression control inputs used may be over estimated (higher  $d_{4,max}$  and lower  $m_4$ ).

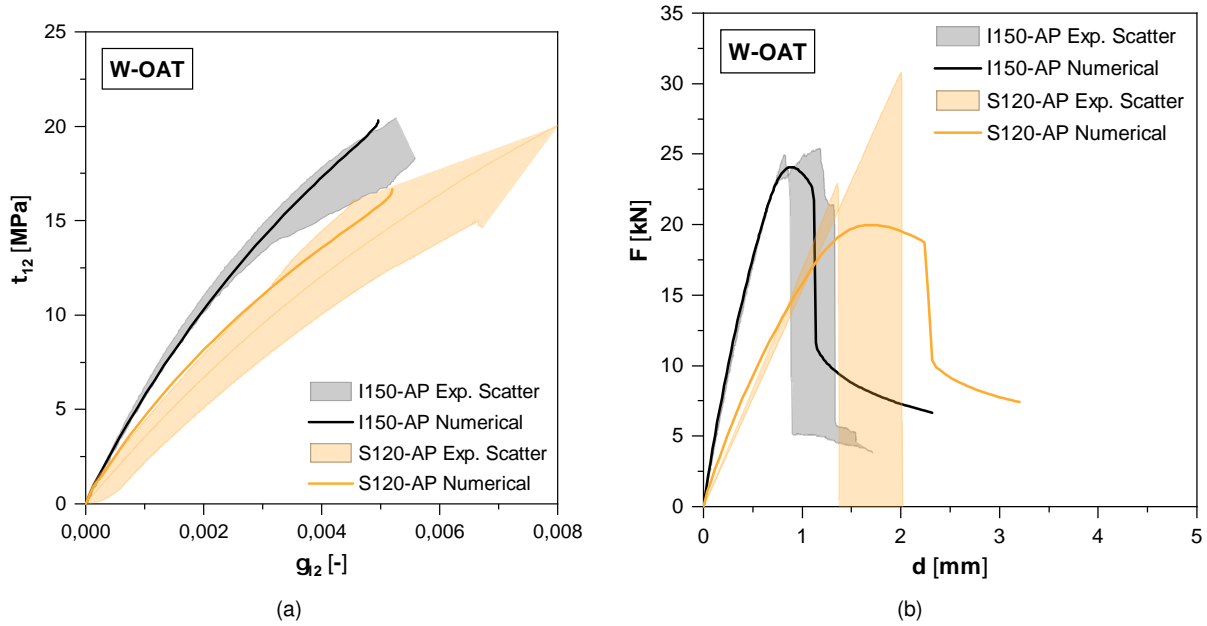


**Figure 4.16:** 10° Off-axis tensile tests - experimental vs. numerical results for web plate: (a) stress vs. strain curves; (b) load vs. displacement curves.

Material	$d_{4,max}$	$m_4$	$\gamma_{12,u}$	$r_{12}$	$G_{12}$ [GPa]		$S_{12}$ [MPa]	
					Value	$\Delta$ (%)	Value	$\Delta$ (%)
I150-AP-W	0.95	0.4	0.024	0.01	4.59	-2.4	20.6	1.1
S120-AP	0.97	0.3	0.030	0.01	3.52	2.0	16.7	-0.7

**Table 4.7:** 10° Off-axis tensile tests - calibration inputs and summary of main results.

Figures 4.17 show the numerical simulation in different phases. The damage starts near the edges, as predicted by Ho *et al.* [60] and propagates through the width of the specimen with a 10° angle. Additionally, and due to the small  $m_4$  input adopted (Table 4.7), the shear modulus  $G_{12}$  is reduced to  $\approx 50\%$  of its initial value in the entire specimen even for half the ultimate shear strain.

Overall, the main advantage of the 10° off axis tensile test compared to the *losipescu* is the obtainment of both residual strength control inputs ( $\gamma_{12,u}$  and  $r_{12}$ ). However, it is not possible to have numerical curves that are in good agreement with experimental data for both tests using the same damage progression control inputs. For this reason, there is no particular conclusion in which test better

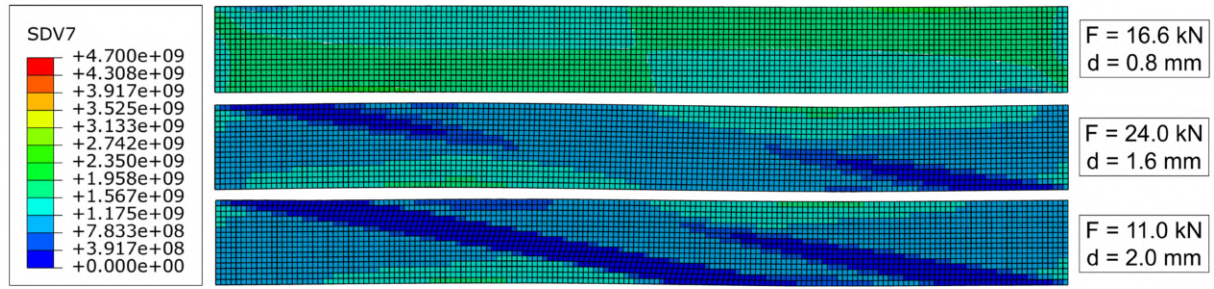


**Figure 4.17:** Failure progression of a numerical 10° off-axis tensile test and degradation of  $G_{12}$  (SDV7) in Pa.

characterises the material, with the additional possibility of combining inputs between both tests. These combinations will be addressed later in the next chapter (*cf.* Section 5.3.4).

### 4.3.7 Compact tension tests

As described earlier, the compact tension test was considered as an additional calibration test in order to fully calibrate the damage model by obtaining the mesh regularisation parameter  $\alpha$  that best suits each material. This parameter was obtained by a curve-fitting process between experimental and numerical load vs. CMOD curves for the 30 mm notch compact tension test (CT-30), and then verified for a notch length of 35 mm (CT-35). The only exception was the I152-CP material, for which the calibration was performed for the CT-35 test due to convergence problems for a notch length of 30 mm. Figures 4.18 (a) and (b) show the final numerical curves obtained and Table 4.8 summarises those results.

## Results

Overall, the numerical curves show very good agreement with experimental data by correctly capturing the initial linear behaviour, the stiffness reduction until the maximum load and the softening stage. For a notch length of 30 mm, with the exception of I152-CP, maximum relative differences of 8% for the stiffness and 4.6% for the maximum load were registered, both for the U150-ST material. As for the I152-CP, a significant underestimation of the maximum load of -23.8% occurred due to convergence problems which can be associated with (i) the high mesh regularisation parameter ( $\alpha = 50$  mm) needed to reach a good agreement between the experimental and numerical maximum loads, and (ii) the nature of the failure mode which in this case is characterised by delamination induced by compressive stresses instead of a simpler crack growth, as discussed below. Nevertheless, the numerical stiffness is well depicted for this material.

Using the same inputs for a 35 mm notch length results in a slight decrease in the relative difference's absolute value, as shown in Table 4.8. Nevertheless, the differences are not significant, allowing the author to conclude that, for differences up to 5 mm in the notch length, the mesh regularisation parameter calibration is practically independent of the notch length. The only exception registered was the I200-FC material, for which significant relative differences between experimental and numerical results were ob-



tained. When computing the stiffness ratio between notch lengths for the same material ( $k = K_{30}/K_{35}$ ), all materials registered the same ratio, as expected, except for I200-FC, leading to believe that these discrepancies are associated with experimental and not numerical errors.

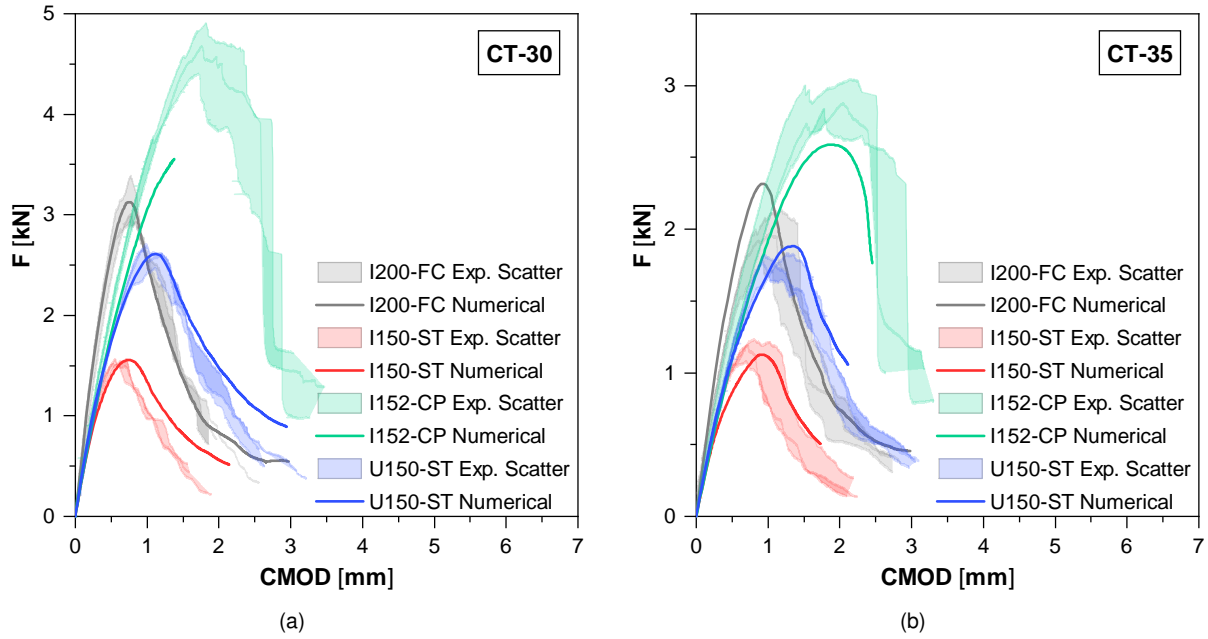


**Figure 4.18:** Compact tension tests - experimental and numerical load vs. CMOD results for web plate: (a) notch length of 30 mm; (b) notch length of 35 mm.

Material	$\alpha$ [m]	Notch length = 30 mm				Notch length = 35 mm			
		$K$ [kN/mm]		$F_{\max}$ [kN]		$K$ [kN/mm]		$F_{\max}$ [kN]	
		Value	$\Delta$ (%)	Value	$\Delta$ (%)	Value	$\Delta$ (%)	Value	$\Delta$ (%)
I200-FC	0.030	6.10	5.9	3.13	0.6	3.96	46.3	2.32	18.0
I150-ST	0.040	4.07	-1.9	1.56	0.5	2.30	-12.5	1.13	-3.8
I152-CP	0.050	3.94	-4.4	-	-	2.34	-8.7	2.59	-11.4
U150-ST	0.030	4.13	8.0	2.73	4.6	2.56	5.2	1.88	4.0

**Table 4.8:** Compact tension tests - calibration input and summary of main results.

## Failure modes

The agreement between experimental and numerical failure modes is also very important to address the quality of the damage progression model. Figures 4.19 and 4.20 show the evolution of the numerical failure modes obtained for I200-FC and I152-CP, respectively.

As expected, the numerical failure modes for materials I200-FC and I150-ST were the same and identical to the experimental data described in Section 3.3.2. For this reason, only the I200-FC is shown. The crack growth is depicted by the complete loss of stiffness in the transverse direction (Figure 4.19 (a)) and by the transverse stresses distribution evolution (Figure 4.19 (b)).

Regarding I152-CP, and even though the numerical models presented convergence problems, the

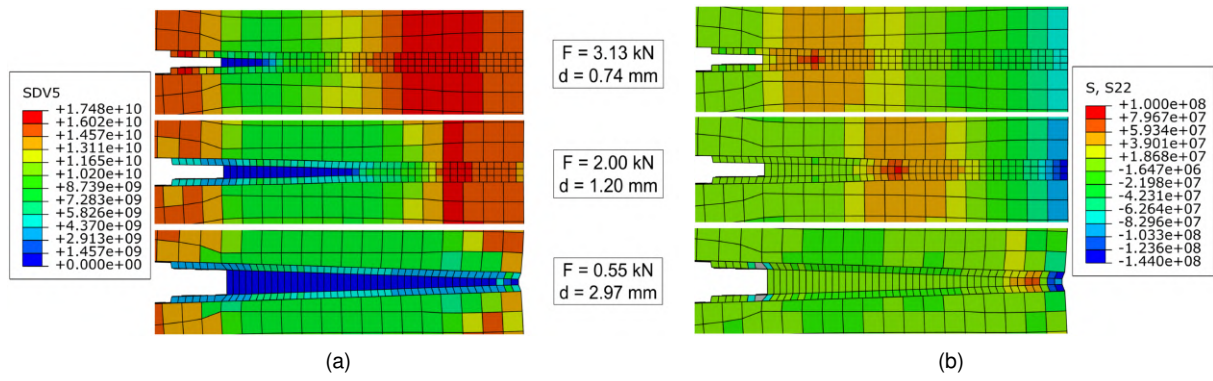


**Figure 4.19:** Compact tension tests - detailed view of failure progression and variable degradation of a numerical simulation for I200-FC-CT-35: (a)  $E_{22}$  (SDV5) in Pa; (b)  $\sigma_{22}$  (S22) in Pa.

final calibration with a 35 mm notch length correctly depicted the experimental behaviour, as shown in Figures 4.20 (a) to (c). The crack growth evolution is represented with the same variables ( $E_{22}$  and  $\sigma_{22}$ ), and in this case, clear signs of out-of-plane displacements during the softening stage were registered, with a maximum of  $\approx 0.7$  mm (Figure 4.20 (c)). These results show that, although the damage progression model considers the GFRP composite material as homogeneous, the experimental out-of-plane displacements are still depicted, even if they cannot be readily attributed to a delamination effect.

Finally, for the U150-ST material, the proximity between the tensile and compressive transverse ultimate strengths ( $S_{22}^+$  and  $S_{22}^-$ ) lead to more prominent compressive damage on the opposite side of the notch in the numerical models than expected, since experimentally this material presents an identical failure mode to I200-FC and I150-ST. This damage is similar to the I152-CP numerical result in Figure 4.20 (c), but with less pronounced out-of-plane displacements (maximum of 0.04 mm, around half of the value registered for I152-CP).

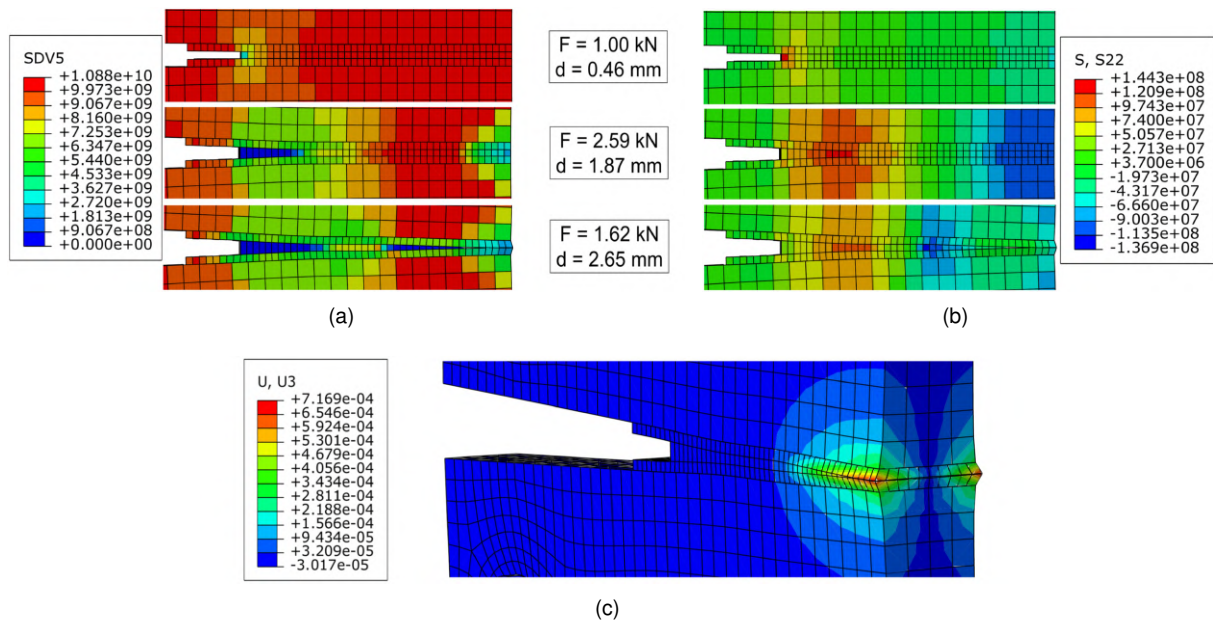


**Figure 4.20:** Compact tension tests - detailed view of failure progression and variable degradation of a numerical simulation for I152-CP-CT-35: (a)  $E_{22}$  (SDV5) in Pa; (b)  $\sigma_{22}$  (S22) in Pa; (c) out-of-plane displacements (U3) in mm.



## Chapter 5

# Application of the model

In this chapter, 4 different application tests are tested in order to evaluate the damage progression model performance. These tests comprise of (i) wide compact tension tests, (ii) compact compression tests, (iii) web-crippling tests, and (iv) double-lap tests. Each test has different characteristics that allow for a better comprehension of the damage progression model capabilities, not only regarding the calibration performed in Chapter 4 by the comparison of load vs. displacement curves intrinsic to each test, but also by examining the numerical failure modes obtained and correlating them with the experimental data presented in Chapter 3.

Firstly, the description of the FE models used for each test is made, followed by a mesh study that aims to understand the effect that both mesh element size and the viscous regularisation parameter (the latter is not performed for every test) in the results. Lastly the results are presented and discussed by comparing the numerical curves, the main properties of each test (stiffness and maximum load), and failure modes with experimental data.

### 5.1 Description of FE models

All models followed the same general considerations as previously mentioned in Section 4.1.1. C3D8R elements were used for the mesh, the contact formulation was similar to that used to model the *Iosipescu* test (*c.f.* Section 4.1.4), and the displacement steps' maximum and minimum increment sizes were set to 0.2% and  $1 \times 10^{-10}\%$  of the total displacement. Moreover, and as in the previous chapter, implicit analyses were conducted for all models allowing for a maximum residual flux norm of 1%, except for severe discontinuity iterations, for which that value was increased to 5% [3].

#### 5.1.1 Wide compact tension tests

The finite element model used to obtain the numerical simulations is based on the experimental wide compact tension test specimen presented earlier in Figure 3.14, with both notch lengths of 30 mm and 40 mm being modelled. Symmetry boundary conditions were applied in the thickness direction, reducing the specimen to half. Additionally, the fixed and displacement boundary conditions were applied in

reference points coupled with the end faces of the respective steel pins, as shown in Figure 5.1 (a), and the contact formulation mentioned above was used to establish the interaction between the steel pins and the GFRP specimen.

Regarding the mesh details, the model was divided in the same manner as the compact tension test (c.f. Section 4.1.5) to facilitate the mesh refinement analysis. Two elements in the thickness directions were used in the coarser meshed sections (which corresponds to 2.5 mm for I200-FC, 2 mm for I150-ST and U150-ST and 1.5 mm for I152-CP), while the notch zone was meshed with nominal element sizes of 1 mm, 0.5 mm and 0.25 mm, as depicted in Figure 5.1 (b). Near the rounded part of the notch, the mesh was always more irregular, not producing the exact same sized elements as the remainder of this section.

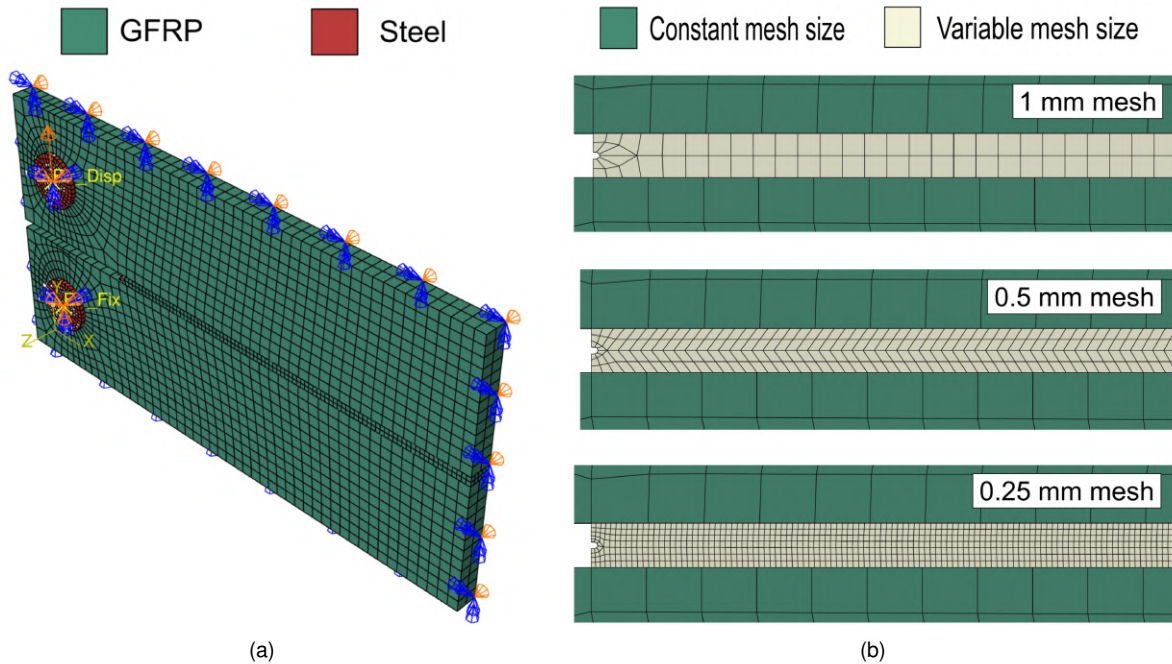


**Figure 5.1:** Wide compact tension test - main characteristics of a numerical model for I200-FC-WCT-30: (a) Boundary conditions and general mesh overview; (b) mesh refinement detailed view.

### 5.1.2 Compact compression tests

The compact compression models were also modelled as depicted earlier in Figure 3.16. However, due to limited experimental results on the 45 mm notch specimens, only the 40 mm notch specimens were modelled. Moreover, an initial study comparing semi-circular notch tip with a sharp notch tip was made, and as registered in [47], the former induced earlier damage propagation resulting in lower ultimate loads. For this reason, a sharp notch tip geometry was adopted.

Symmetry boundary conditions were again applied at mid-thickness as shown in Figure 5.2 (a), and the steel pins interacted with the GFRP specimen through the same contact formulation. The mesh detailed section was also utilised, with mesh element sizes of 2 mm, 1 mm and 0.5 mm used (Figure 5.2 (b)), while the coarser regions were also meshed with two elements in the thickness direction.

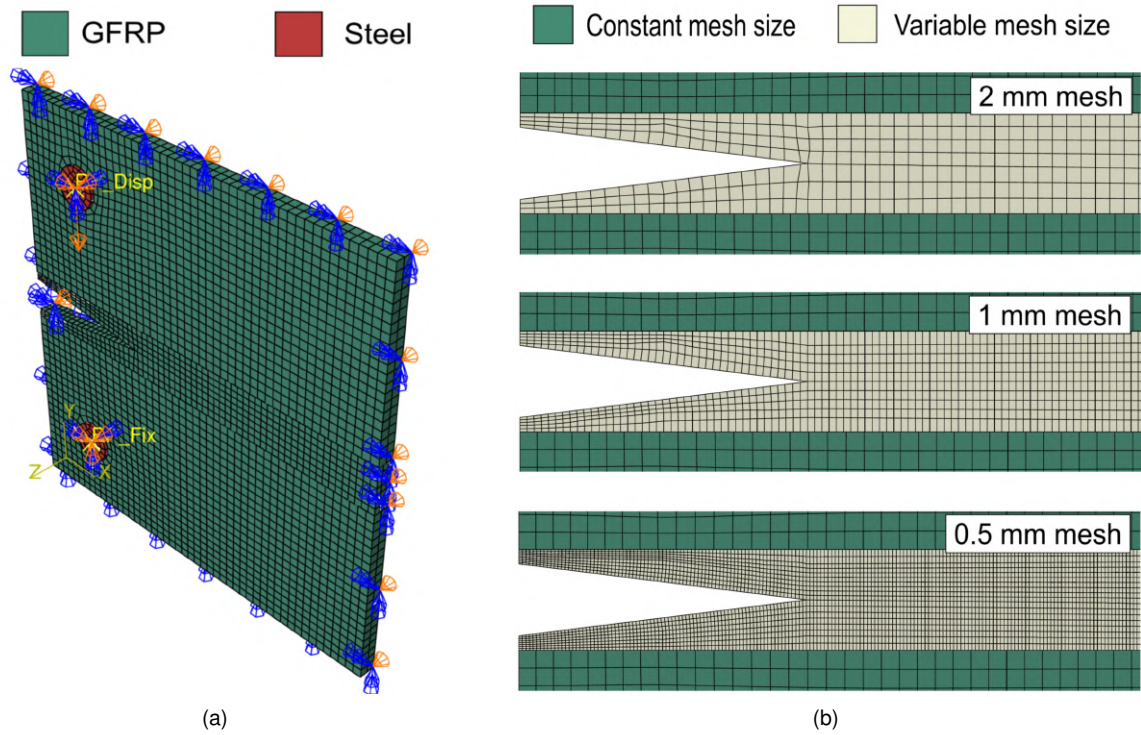


**Figure 5.2:** Compact compression test - main characteristics of a numerical model for I200-FC-CC-40: (a) Boundary conditions and general mesh overview; (b) mesh refinement detailed view.

### 5.1.3 Web-crippling tests

Web-crippling test models were divided in two categories, according to the failure modes registered experimentally: (i) simplified models, which were used to model profiles that failed due to crushing only, and (ii) complete models, utilised for profiles that presented a buckling or mixed failure mode. The former were used for materials I200-FC and I150-ST, and the latter for I152-CP and U150-ST, for both ITF and ETF configurations in each case.

For all cases, the main geometric features were modeled according to the dimensions presented in Table 3.1 (when using symmetry, the dimensions were adjusted accordingly). As a simplification, the web-flange junctions were modelled with the web material properties, since there was no detailed information regarding these zones, which are known to be potentially weaker [63–65]. The displacement was induced through steel blocks with the specific bearing length of each test, and the interaction between these and the flanges was formulated as other contacts. Moreover, the mesh refinement was also performed in specific zones to reduce the total computational cost. These regions included the bearing length and the adjacent region where stress distributions are slightly non-uniform. A coarser mesh size of half-thickness, which is material dependent (*cf.* Table 3.1), was used for all models, with a further decrease in size to a quarter and an eighth of the thickness for the mesh study (in the specific regions). Figure 5.3 (a) shows a complete model's boundary conditions and mesh example, and Figure (b) depicts the mesh refinement study, both made for the ITF-100 configuration of I152-CP. Other materials and configurations followed the same method, varying only in the geometry.

Regarding the simplified models, the ITF geometry allowed the use of triple symmetry boundary

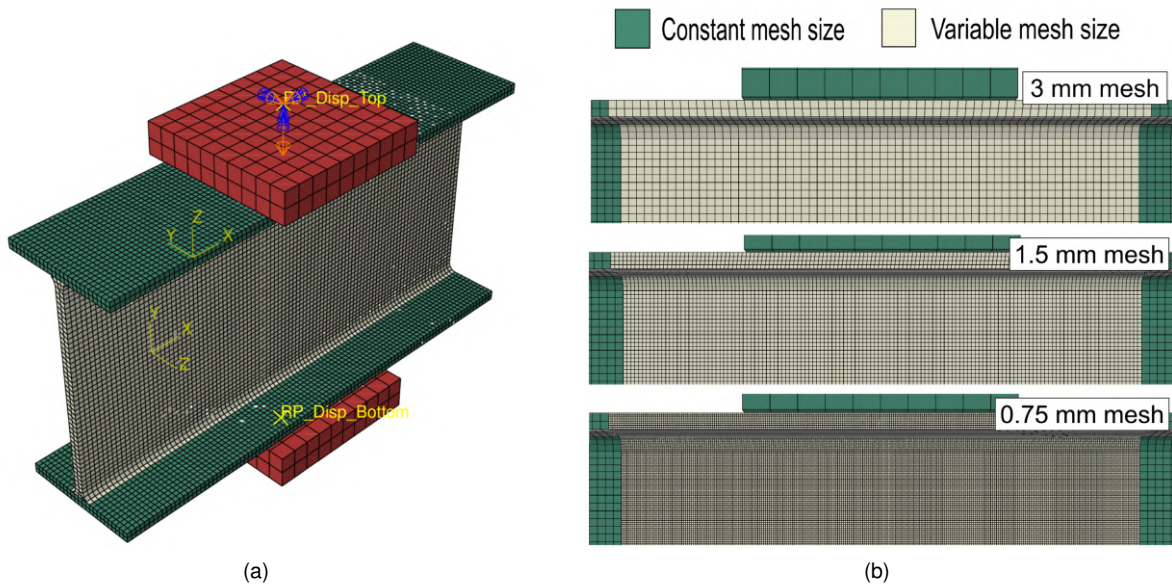


**Figure 5.3:** Web-crippling test - main characteristics of a complete numerical model for I152-FC-WC-ITF-100: (a) Boundary conditions and general mesh overview; (b) mesh refinement detailed view.

conditions, with dimensions reduced to half. However, the ETF configuration only allowed for double symmetry to be used, with the length being fully modelled.

As for the complete models, non-linear geometric analyses were conducted, since the web's out-of plane displacements were one of the effects that led to failure of the specimens. Additionally, an initial imperfection with 0.01 mm of amplitude [44] correspondent to the critical buckling mode was considered for both configurations of I152-CP and U150-ST.

#### 5.1.4 Double-lap tests

For the double-lap numerical models, the setup presented earlier in Figure 3.22 was considerably simplified. The steel support was discarded and the fixed boundary conditions were applied on the bolt's surface corresponding to the steel support's thickness, as exemplified in Figure 5.4 (a). Symmetry boundary conditions were used in the y and z directions, reducing the width and thickness to half, respectively, and the displacement was applied on the end face of the model. The usual contact formulation was used in the interaction between the steel bolt and the GFRP composite.

As for the mesh, Figure 5.4 depicts the mesh refinement process that was performed. The region between the end face (opposite to the loaded end) and the centre of the bolt plus 15 mm was considered for this study, with meshes of 2 mm, 1 mm and 0.5 mm being used. The remaining part was meshed with coarser 4 mm sized elements since the stress field in this section is practically irrelevant.

Moreover, even though Figure 5.4 is relative to the DL-35 configuration, other models with different edge differences followed exactly the same methodology.



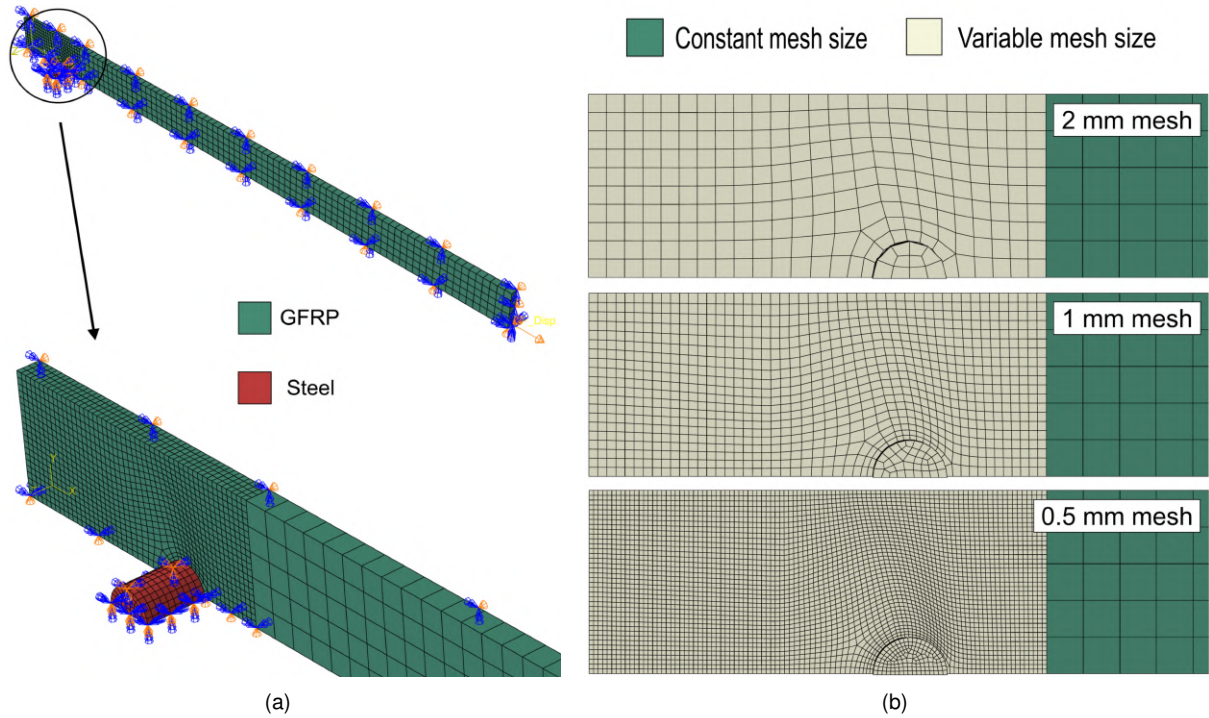


**Figure 5.4:** Double-lap test - main characteristics of a DL-35 numerical model for: (a) Boundary conditions and general mesh overview; (b) mesh refinement detailed view.

## 5.2 Mesh study

This section focuses on the mesh study performed on application tests. The material I200-FC was chosen for this study for all tests, except for the double-lap where the I150-AP was used. Figures 5.5 and 5.6 present the experimental data and the numerical load vs. displacement curves obtained, and Table 5.1 summarises the main results, namely the stiffness ( $K$ ) and the maximum load ( $F_{\max}$ ) of each test and mesh combination.

### 5.2.1 Wide compact tension tests

For wide compact tension tests, the mesh study presented only considers the 30 mm notch geometry as the 40 mm notch results' were similar. As shown in Table 5.1, using a 1 mm mesh in the detailed section shown in Figure 5.1 (b) results in relative differences of 18.5% and 2.6% for the stiffness and maximum load, respectively. Further refinements with meshes of 0.5 mm and 0.25 mm result in a decrease from 18.5% to 17.3% and 16.4%, corresponding to 1.2 and 0.6 percentage points differences, regarding stiffness values. More importantly, these decreases in relative differences for the maximum load are of 9.1 and 0.6 percentage points, showing that the difference between a 0.5 mm and a 0.25 mm mesh is much lower than from 1 mm to 0.5 mm. This effect may also be seen in the load vs. CMOD curves presented in Figure 5.5 (a).

In view of these results, all wide compact tension tests' results presented hereafter are obtained with a 0.5 mm mesh in the notch region.

## 5.2.2 Compact compression tests

Regarding the mesh study results for the compact compression tests, Table 5.1 highlights stiffness relative differences between meshes of 2, 1 and 0.5 mm of 21.2%, 20.3% and 19.8%, respectively, with respect to experimental data. As for maximum load, the relative differences are of 27.5%, 24.5% and 24.0%. Although considerably overestimated (this is duly addressed in Section 5.3.2, along with the numerical difficulties regarding the post-linear phase behaviour), these results show that refining the mesh produces a decrease in the change between relative differences, for both stiffness (0.9 to 0.5 percentage points) and maximum load (3.0 to 0.5 percentage points). It should be stressed that the maximum load registered corresponds to the end of the linear stage, as will be further addressed in Section 5.3.2.

These results follow the same pattern as wide compact tension tests, with the middle mesh size already presenting a steady value and the model's simulation being considerably quicker than the most finer mesh. For this reason, all other compact compression tests results are obtained with a 1 mm mesh in the notch region.

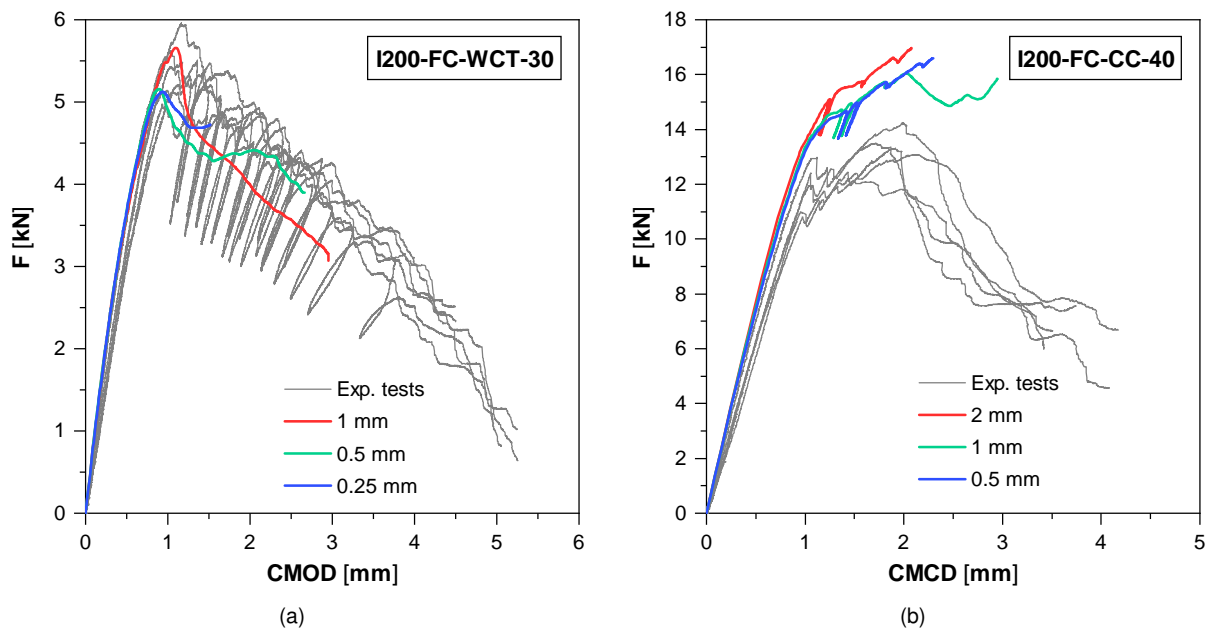


**Figure 5.5:** Experimental and numerical results of load vs. displacement curves of application tests with different mesh sizes: (a) I200-FC-WCT-30; (b) I200-FC-CC-40.

## 5.2.3 Web-crippling tests

The web-crippling tests for an ITF-100 configuration of the I200-FC material are presented in Figure 5.6 (a) and Table 5.1. Regarding the stiffness, a coarser mesh size of 5 mm results in an over-estimation of 20.0%, while 2.5 mm and 1.25 mm meshes result in relative differences of 19.7% and 19.4%, respectively. Figure 5.6 (a) also depicts a gradual stiffness loss in the later loading stage with more refined meshes that is not depicted in stiffness values since they were retrieved between 10% to 20% of the maximum load. As for the maximum load, the mesh refinement from 5 mm to 2.5 mm and

to a further 1.25 mm results in changes of 13.9 and -0.2 percentage points, indicating that for a mesh of 2.5 mm (corresponding to a quarter of the profile's thickness) the results are already stabilized.

Additionally, studies on the viscous regularisation parameter inputs (Figure 5.6 (a)) and on other configurations of web-crippling tests (ETF-15 and ETF-100) and profiles (U section) produced the same conclusions. With these results in mind, a mesh size of quarter-thickness (2.5 mm for I200-FC, 2 mm for I150-ST and U150-ST, and 1.5 mm for I152-CP) and a viscous regularisation parameter of  $\eta_i = 1 \times 10^{-3}$  were used for all web-crippling simulations.

## 5.2.4 Double-lap tests

The results obtained for the double-lap mesh study are presented in Table 5.1 and Figure 5.6 (b). Since there were doubts regarding the experimental stiffness measured in these tests and the setup information available in [50] and [51] is not sufficient to accurately compare experimental and numerical displacements, the numerical load vs. displacement stiffnesses were adjusted to the experimental data. For this reason, the stiffness results presented in Table 5.1 are purposely obtained to minimise the relative differences and are not valid to establish any comparison, hence only the maximum load values are relevant for this mesh study. Moreover, the numerical curves presented were obtained using the  $10^9$  off-axis tensile test properties (*cf.* Table 4.7), with further discussion on this topic in Section 5.3.4.

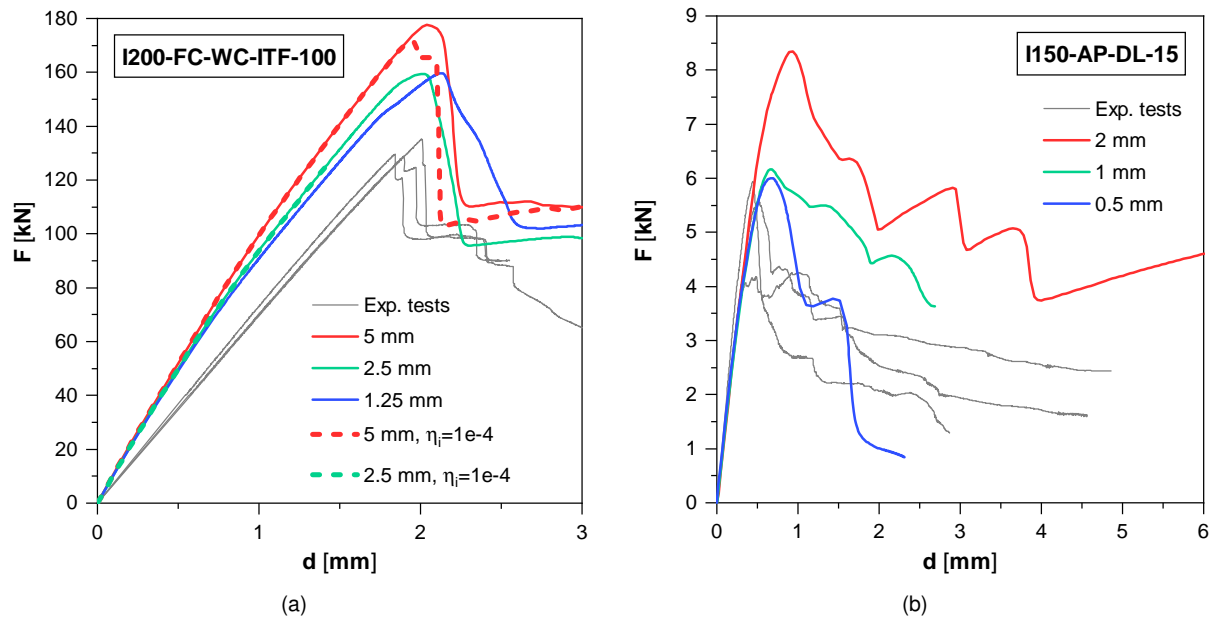


**Figure 5.6:** Experimental and numerical results of load vs. displacement curves of application tests with different mesh sizes: (a) I200-FC-WC-ITF-100; (b) I150-AP-DL-15.

Utilising a mesh of 2 mm in the relevant region mentioned in Section 5.1.4 leads to an overestimation of the maximum load in 58.9%. Decreasing the element size to 1 mm decreases this difference by 41.6 percentage points, and a further refinement to 0.5 mm leads to a change in 3 percentage points (compared to the 1mm sized mesh), showing that the two latter mesh sizes already produce consistent maximum load predictions. However, when analysing the numerical curves in Figure 5.6 (b), it can

be seen that a 0.5 mm mesh exhibits a more accurate behaviour regarding the stiffness loss after the maximum load and the final residual stress stage. For this reason, a 0.5 mm mesh was used in the region highlighted in Figure 5.4 (b) for all double-lap tests' configurations.

Test	Property	1 mm mesh		0.5 mm mesh		0.25 mm mesh	
		Value	$\Delta$ (%)	Value	$\Delta$ (%)	Value	$\Delta$ (%)
Wide compact tension - 30	$K$ [kN/mm]	8.52	18.5	8.43	17.3	8.39	16.7
	$F_{\max}$ [kN]	5.66	2.6	5.16	-6.5	5.11	-7.1
Compact compression - 40	$K$ [kN/mm]	2 mm mesh		1 mm mesh		0.5 mm mesh	
	$F_{\max}$ [kN]	15.63	21.2	15.50	20.3	15.44	19.8
Web-crippling - ITF-100	$K$ [kN/mm]	15.08	27.5	14.73	24.5	14.67	24.0
	$F_{\max}$ [kN]	5 mm mesh		2.5 mm mesh		1.25 mm mesh	
Double-lap - 15	$K$ [kN/mm]	147.9	20.0	147.5	19.7	147.1	19.4
	$F_{\max}$ [kN]	177.7	35.4	159.4	21.5	159.7	21.7
Double-lap - 15	$K$ [kN/mm] *	2 mm mesh		1 mm mesh		0.5 mm mesh	
	$F_{\max}$ [kN]	14.4	0.8	14.1	-1.7	14.5	1.3
		8.34	58.9	6.16	17.3	6.00	14.3

**Table 5.1:** Main application tests' results of I200-FC (and I150-AP for DL test) and relative difference to the experimental average for different meshes.

\* Stiffness values are not valid for comparison with experimental data.

## 5.3 Results and discussion

### 5.3.1 Wide compact tension tests

#### Results

The results obtained are summarised in Figures 5.7 (a) and (b), and Table 5.2. As shown, for materials I200-FC, I150-ST, and U150-ST, the load vs. CMOD curves are in good agreement with the experimental data, with both the linear behaviour until the maximum load and the following softening stage correctly depicted. The maximum load registers the highest relative difference of 13.5% for the I152-CP-WCT-40 specimen, with all others being below 10%. As for the stiffness, although the numerical curves seem coincident with experimental data in Figures 5.7 (a) and (b), Table 5.2 highlights that for I200-FC and U150-ST, there is a relative difference of  $\approx 20\%$ . This difference may be emphasised by the small interval (between approximately 10% and 20% of  $F_{\max}$ ) for which the stiffness was computed.

As for I152-CP, the final calibration simulations presented convergence problems for both notch lengths, following the same trend as in compact tension tests (*cf.* Section 4.3.7). This led to non-reliable maximum load results, even though stiffness results are in very good agreement with experimental values, with a maximum relative difference of 7.9% for I152-CP-WCT-40.

Due to the buckling effect registered for 40 mm notch length tests' failure mode of I152-CP (see Section 3.3.3), two additional simulations with no symmetric boundary conditions and considering a non-linear geometric analysis were performed - one with these conditions only, and another considering an



initial deformation correspondent to the first buckling failure mode, with an amplitude of 0.01 mm. The results for these simulations were the same, most likely because of the high buckling load of 44.2 kN. Even so, the load vs. CMOD curves show a similar behaviour until the maximum load compared to the original simulation, but do not present convergence problems and allow the development of the softening stage, as seen in Figure 5.7 (b).

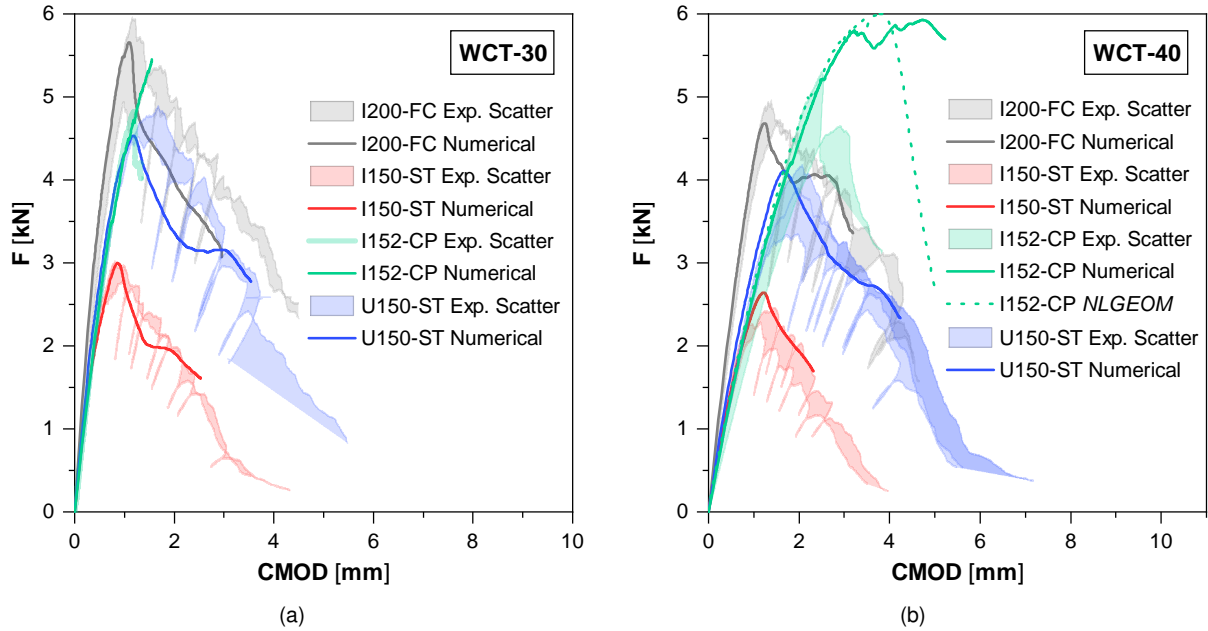


**Figure 5.7:** Wide compact tension test - experimental and numerical load vs. displacement curves for: (a) 30 mm notch length; (b) 40 mm notch length.

Material	Notch length = 30 mm				Notch length = 40 mm*			
	$K$ [kN/mm]		$F_{max}$ [kN]		$K$ [kN/mm]		$F_{max}$ [kN]	
	Value	$\Delta$ (%)	Value	$\Delta$ (%)	Value	$\Delta$ (%)	Value	$\Delta$ (%)
I200-FC	8.43	17.3	5.16	-6.5	5.01	19.2	4.68	-1.7
I150-ST	5.79	11.8	3.00	7.1	3.28	5.4	2.64	13.5
I152-CP	5.35	-2.3	-	-	2.83	7.9	-	-
NLGEOM	-	-	-	-	2.80	6.7	6.00	23.7
U150-ST	6.35	26.6	4.53	-2.9	3.43	17.7	4.11	8.5

**Table 5.2:** Wide compact tension test - summary of main results.

\* For I200-FC, the notch length is 38 mm.

## Failure modes

The failure modes registered for most materials including I200-FC, I150-ST and U150-ST and both notch lengths were similar to the aforementioned compact tension tests and in agreement with experimental data. Figure 5.8 shows the crack propagation evolution for an I150-ST-WCT-30 numerical simulation, highlighting both stiffness degradation and the propagation of transverse stresses for different displacements.

Contrarily, and as mentioned in Section 3.3.3, I152-CP experimental data exhibited (i) failure in the load application holes for notch lengths of 30 mm, and (ii) buckling coupled with failure in the load application holes for notch lengths of 40 mm. Numerically, and although the maximum load prediction was not accurate, both configurations exhibited degradation in the load application holes in addition to the initial crack growth. Furthermore, regarding the 40 mm notch lengths numerical results, the out-of-plane displacements that occurred experimentally due to buckling were not registered in any numerical simulation, even when accounting for non-linear effects. Moreover, it should be noted that for the only case where the numerical simulation successfully converged (I152-CP-WCT-40-NLGEOM), crack propagation occurred in parallel with the hole damage (although less prominently) in the same way as other materials.

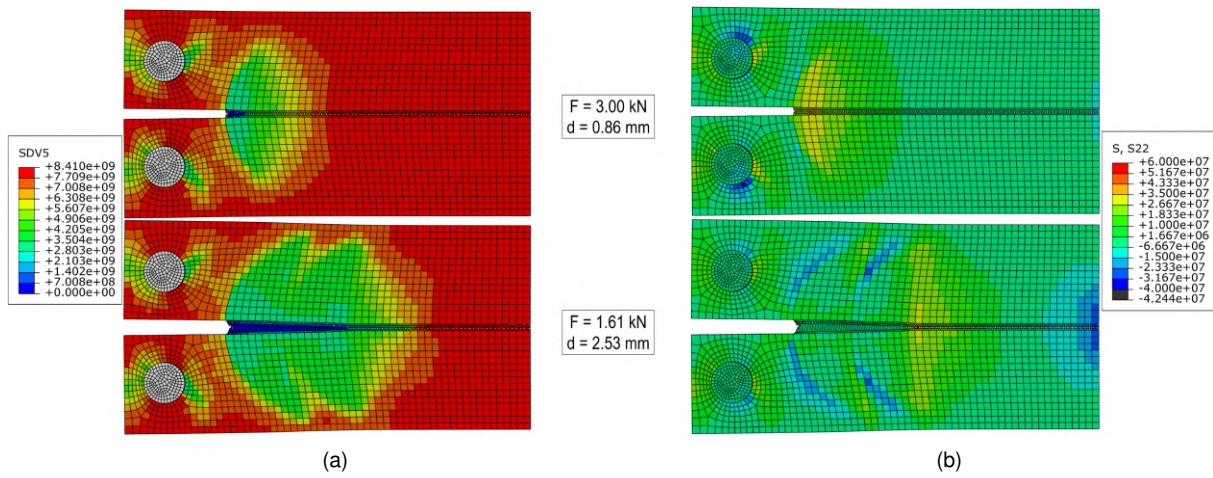


**Figure 5.8:** Wide compact tension test - failure progression and variable degradation of a numerical simulation for I150-ST-WCT-30: (a)  $E_{22}$  (SDV5) in Pa; (b)  $\sigma_{22}$  (S22) in Pa.

These results show that, for wide compact tensions tests, the damage model correctly predicts load vs. CMOD curves and the failure modes for most materials, with only I152-CP presenting some difficulties due to convergence problems. Nonetheless, the more intricate failure modes that presented failure in the load application holes were still partially captured by the numerical simulations.

### 5.3.2 Compact compression tests

#### Results

The load vs. CMCD obtained are shown in Figures 5.9 (a) and (b) and the main results are summarised in Table 5.3.

Firstly, the experimental linear behaviour is well depicted for all materials, even though Table 5.3 presents some overestimation in the stiffness values for I200-FC and U150-ST. These differences are the consequence of adopting only one elastic modulus for each direction in the damage model based on the assumption that tensile and compressive moduli are similar, which is evident in the longitudinal direction, but not in the transverse direction. This effect is particularly relevant for I200-FC and U150-ST's stiffness values, with relative differences of 20.3% and 8.4%, respectively. Both these materials exhibited

higher transverse elastic modulus in tension than compression ( $E_{22}^+ > E_{22}^-$ , cf. Table B.1). As for other materials, numerical stiffness values are in excellent agreement with experimental data, presenting relative differences of 0.1% for I150-ST and 1.4% for I152-CP. Moreover, as registered experimentally, the non-linear stage that followed the linear phase for the I200-FC material was also registered numerically.

Secondly, the maximum loads obtained with the models follow the same trend as stiffness results, except I152-CP, for which a 1.4% relative difference in stiffness resulted in a 11.7% relative difference in the maximum load. This higher difference can be explained again by the author's doubts regarding the mesh regularisation parameter used for this material, even though this input is not particularly relevant for the compact compression test. Furthermore, it should be stressed that, for I200-FC, the maximum load values refer to the load immediately after the linear stage, as was done for experimental results in Section 3.3.4, and not the true maximum load. This approach was used due to the instability in numerical results after the linear stage.

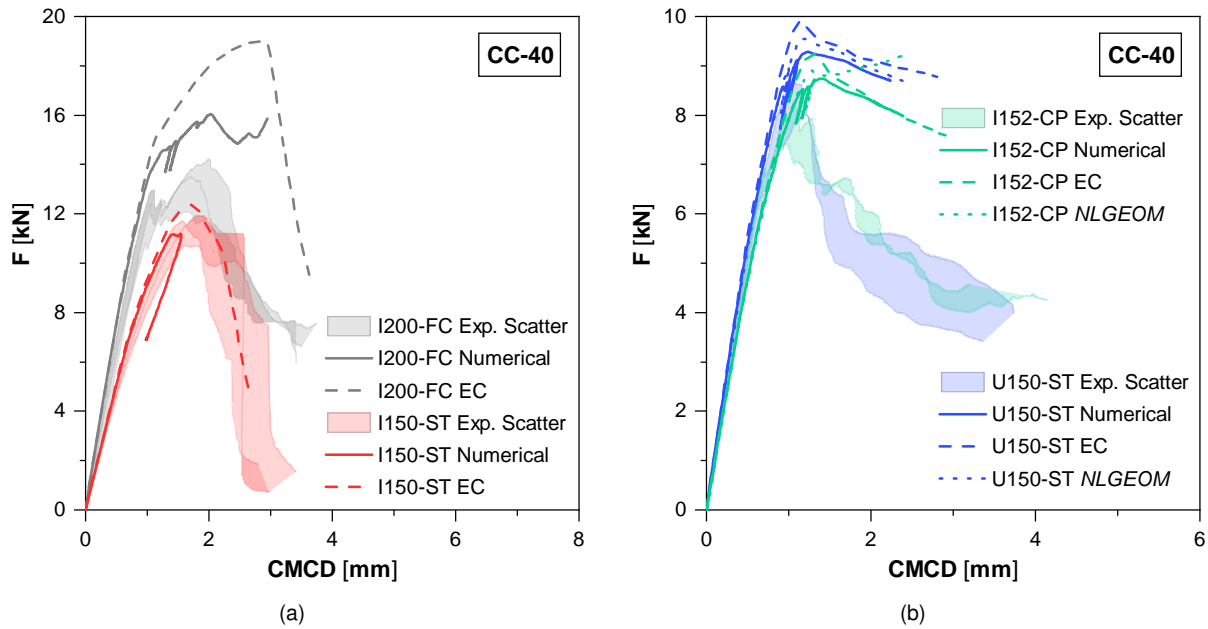


**Figure 5.9:** Compact compression test - experimental and numerical load vs. displacement curves for: (a) I200-FC and I150-ST (b) I152-CP and U150-ST.

Thirdly, and as shown in Figures 5.9 (a) and (b), all materials' load vs. CMCD curves near the maximum load region are compromised by displacement fluctuations that were not expected. These fluctuations are associated with transverse elastic modulus degradation in the GFRP specimen near the load application holes caused by the high stress concentrations in these zones. When these degraded elements reach total failure, the model tends slightly to its initial position, hence the load and displacement decrease for a short time. This effect can be seen in the next section when the failure modes are specifically addressed (Figure 5.11 (a)). For this reason, a model considering only elastic deformation for the GFRP materials in these zones was also used in order to isolate the numerical failure to the crack growth behaviour observed in the notch region. These results are also presented in Figures 5.9 (a) and (b) and Table 5.3 with the nomenclature "EC" (stands for engineering constants, which was the method used to define the material in the software), and can be interpreted as an upper bound of the numerical

behaviour since they inhibited any kind of degradation near the holes. In fact, stiffness values remained the same when compared to the original numerical results, and the maximum load increased for all materials. Furthermore, these alternative results show better agreement regarding the non-linear phase of I200-FC's curve and the softening stage of both I200-FC and I150-ST, allowing for the convergence of the model and the development of tensile stresses in the opposite side of the notch that ultimately leads to total failure.

Finally, for materials I152-CP and U150-ST, where failure did not occur due to tensile stresses on the opposite side of the notch, additional models considering a non-linear geometric analysis were adopted in order to capture the out-of-plane displacements that occurred experimentally in the softening stage. These simulations did not improve the results, showing practically the same behaviour as the “EC” and the original numerical curve.

### Residual strength parametric study

Additionally, given the author's doubt regarding the residual strength parameter  $r_{22}^-$  obtained with the CLC tests (especially for I200-FC, which registered a very high value of  $r_{22}^- = 0.5$ ), a parametric study was performed in order to understand the influence of this input in the compact compression test's numerical behaviour. To reduce relative differences between numerical and experimental tests, the compressive elastic modulus ( $E_{22}^-$ ) was adopted instead of the tensile one ( $E_{22}^+$ ).

The results obtained regarding the I200-FC material are shown in Figure 5.10, and Table 5.3 presents the best-case scenario, which was obtained for a residual strength input of  $r_{22}^- = 0.4$ . As expected, the stiffness and the maximum load's relative difference decreased to 3.0% and -0.2%, respectively. The load vs. CMCD curves show that (i) for a  $r_{22}^- = 0.4$ , the numerical behaviour is similar to the experimental (and to the “EC” curve), and although ultimate failure is delayed, it is still captured correctly, (ii) for a  $r_{22}^- = 0.3$ , the simulation presented convergence problems and stopped after the linear stage, (iii) for a  $r_{22}^- = 0.2$ , the load was practically constant after the linear stage, with sudden changes occurring due to failure in the load application holes, as described earlier, and (iv) for  $r_{22}^- = 0.1$ , the non-linear stage between the end of the linear stage and ultimate failure was not captured by the numerical simulation. In the last two cases, ultimate failure was not reached.

With these results, it is predicted that the real residual strength for I200-FC is between 0.3 and 0.4. Nonetheless, the calibration parameters were not altered for other tests.

As for other materials, this parametric study was also performed, but no significant changes were obtained, therefore the results are not presented. In fact, residual strength inputs for I150-ST, I152-CP and U150-ST were not as high as for I200-FC, hence the lack of significant changes.

### Failure modes

As described in Section 3.3.4, every specimen exhibited damage in the form of a kink band that originated due to compressive stresses and propagated along the longitudinal direction, starting at the notch tip. This damage propagation phenomenon was correctly depicted for every numerical simulation,

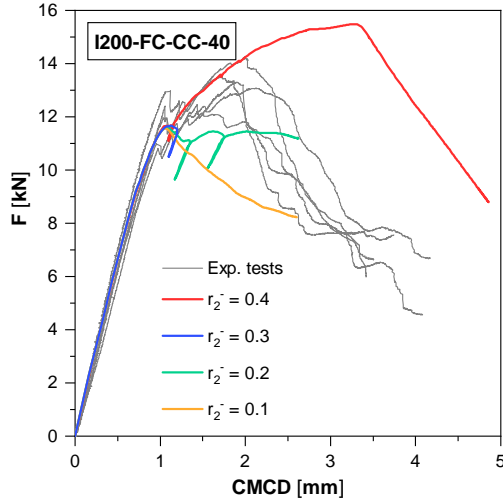


**Figure 5.10:** Compact compression test -  $r_{22}^-$  parametric study for I200-FC with compressive elastic modulus  $E_{22}^-$  as input.

Material	$K$ [kN/mm]		$F_{max}$ [kN]	
	Value	$\Delta$ (%)	Value	$\Delta$ (%)
I200-FC	15.5	20.3	14.7	24.5
EC	15.5	20.3	15.1	27.9
$r_{22}^- = 0.4$	13.3	3.0	11.8	-0.2
I150-ST	10.3	0.1	11.2	-4.0
EC	10.3	0.5	12.4	6.2
I152-CP	9.83	1.4	8.74	11.7
EC	9.84	1.5	9.25	18.2
NLGEOM	9.99	3.0	9.25	18.2
U150-ST	11.1	8.4	9.28	11.3
EC	11.3	11.0	9.91	19.0
NLGEOM	10.9	6.5	9.55	14.5

**Table 5.3:** Compact compression test - summary of main results.

and its effect on the transverse elastic modulus degradation is shown in Figure 5.11 (a).

Additionally, and as mentioned in the section above, every numerical simulation presented unexpected failure in the load application holes region (Figure 5.11), with different degrees of intensity, and which possibly hindered the crack propagation. For example, this type of damage was more prominent in I150-ST than in I152-CP, as depicted by the CMCD fluctuations in Figures 5.9 (a) and (b).

Regarding the ultimate failure mode of this test, and by using the “EC” simulations (the  $r_{22}^- = 0.4$  version of I200-FC was also able to depict this failure), the tensile failure on the opposite side of the notch was correctly depicted for materials I200-FC and I150-ST, the same that verified it experimentally. This type of failure is shown in Figure 5.12.

Finally, the out-of-plane displacements that were registered in experimental data for materials I152-CP and U150-ST were not captured by the model, even when considering a non-linear geometric analysis, showing compact compression tests are especially challenging to model.

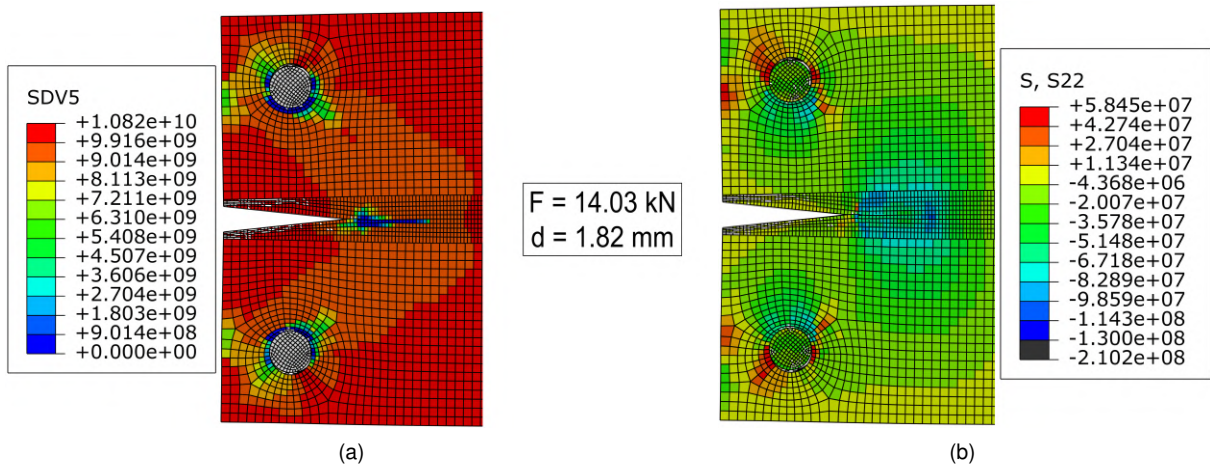


**Figure 5.11:** Compact compression test - notch and application holes' failure of a numerical simulation for I200-FC-CC-40- $E_{22}^-$ - $r_{22}^- = 0.4$ : (a)  $E_{22}$  (SDV5) in Pa; (b)  $\sigma_{22}$  (S22) in Pa units.



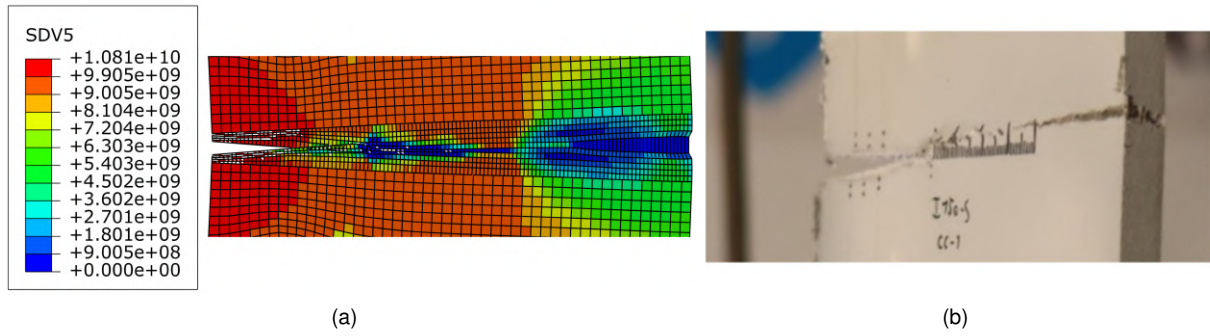


**Figure 5.12:** Compact compression test - tensile failure of: (a) a numerical simulation for I200-FC-CC-40- $E_{22}^- - r_{22}^- = 0.4$ ; (b) an experimental specimen.

### 5.3.3 Web-crippling tests

#### Results

The results obtained regarding load vs. displacement curves for all configurations are summarised in Figures 5.13 (a) and (b) (adjusted for easier comparison with experimental data) and Table 5.4. Starting with the I200-FC profile, both stiffness and maximum load results are overestimated in  $\approx 20\%$  for ITF-100 and in  $\approx 15\%$  for ETF-15 configurations. These values can be correlated with the aforementioned use of the tensile elastic modulus in the damage model inputs instead of the compressive modulus (for I200-FC,  $E_{22}^+ > E_{22}^-$ ), with compressive (and shear) stresses being the main source of damage in these tests.

As for I150-ST, the results for the ITF-100 configuration present a stiffness underestimation of -9.8%. However, the maximum load is still overestimated in 20.7%, which can be justified by the simplification of the web-flange junction properties. As for the ETF-15 configuration, a relative difference of -2.74% and -0.9% for stiffness and maximum load was obtained, respectively, showing very good agreement with experimental data.

For these two materials where profiles failed exclusively due to crushing, the residual stress phase is clearly overestimated. This is mainly caused by the high residual strength input calibrated in Section 4.3.4 for compressive transverse tests, which is a consequence of the standard used for determining the mechanical properties in this direction [3].

Regarding I152-CP, numerical results show excellent agreement with experimental ones, apart from an underestimation in stiffness of -9.4% for the ITF-100 configuration. After the maximum load, however, there were convergence difficulties for the ITF-100 configuration and for ETF-15 the residual stress phase is overestimated as in other materials.

Lastly, for the U150-ST profile, there were significant differences between numerical and experimental results, with a stiffness overestimation of 74.4% and 110.6% and maximum load overestimation of 157.6% and 165.4%, for ITF and ETF configurations, respectively. In this case, for an easier comparison, the load vs. displacement curves were not adjusted. These errors are associated with the overestimation of the buckling load due to the over-constrained critical buckling mode conditions. More specifically, while in all experimental cases a portion of the flanges (farthest from the web junction) detached from

the bearing plate where the load was applied, in the numerical models, the critical mode obtained and used as an initial deformation for the non-linear geometric analysis, the flange was always tied to the bearing plate, hence not predicting correctly the buckling mode. This is a limitation of the ABAQUS software package, and some suggestions to solve this limitation are addressed in Section 6.2. Additionally, as Figures 5.13 (a) and (b) show, when using a 10 mm amplitude imperfection instead of a 0.01 mm, the numerical load vs. displacement curve gets closer to the experimental curve, which indicates that this may be part of the problem. Nevertheless, a 10 mm imperfection is a gross overestimation and cannot be real, being only used to identify the problem.

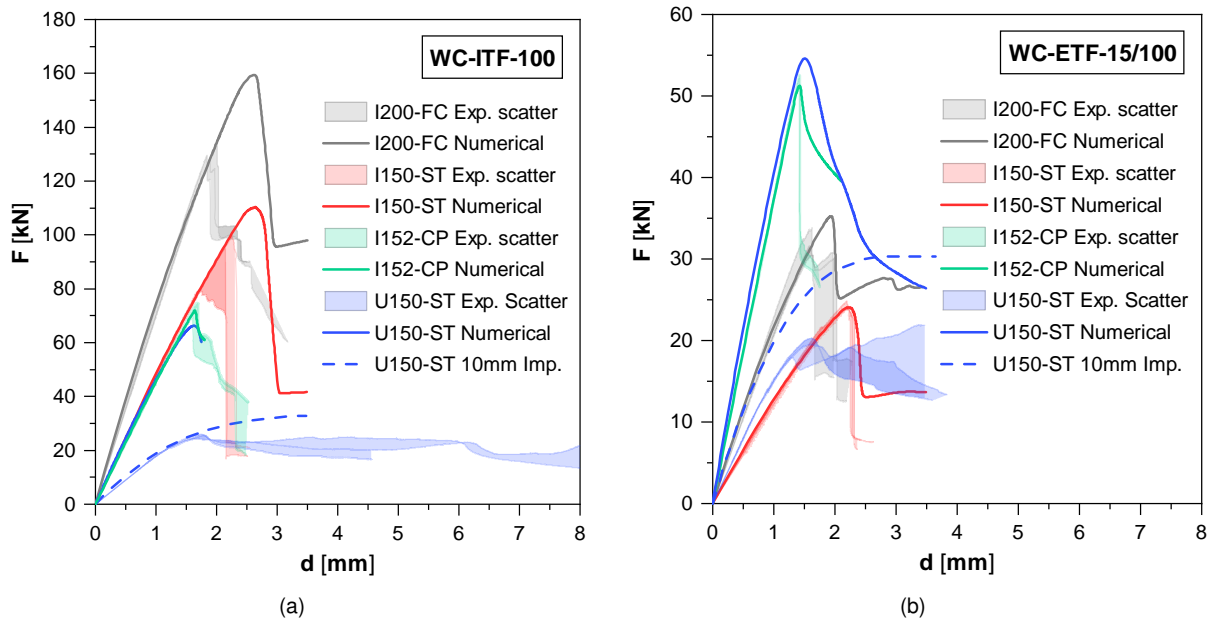


**Figure 5.13:** Web-crippling test - experimental and numerical load vs. displacement curves for: (a) ITF-100 configuration (b) ETF-15 (I200-FC and I150-ST) and ETF-100 (I152-CP and U150-ST) configurations.

Material	ITF-100				ETF-15			
	$K$ [kN/mm]		$F_{max}$ [kN]		$K$ [kN/mm]		$F_{max}$ [kN]	
	Value	$\Delta$ (%)	Value	$\Delta$ (%)	Value	$\Delta$ (%)	Value	$\Delta$ (%)
I200-FC	147.5	19.7	159.5	21.5	38.35	16.5	32.26	10.2
I150-ST	82.07	-9.8	110.3	20.7	21.03	-2.7	24.06	-0.9
	ETF-100							
	$K$ [kN/mm]		$F_{max}$ [kN]					
	Value	$\Delta$ (%)	Value	$\Delta$ (%)				
I152-CP	77.05	-9.4	72.00	-0.4	66.77	0.5	51.24	-0.9
U150-ST	64.92	74.4	66.25	157.6	54.45	110.6	54.63	165.4

**Table 5.4:** Web-crippling test - summary of main results.

## Failure modes

As mentioned in Chapter 3, both configurations of materials I200-FC and I150-ST presented only crushing failure in the web-flange junction near the bearing plates. The numerical models for both con-

figurations show the same failure pattern as experimental data, with Figures 5.14 (a) and (b) exhibiting the complete degradation of the transverse elastic modulus. This failure is promoted by compressive and shear stresses in these zones and is present through the entire web thickness.

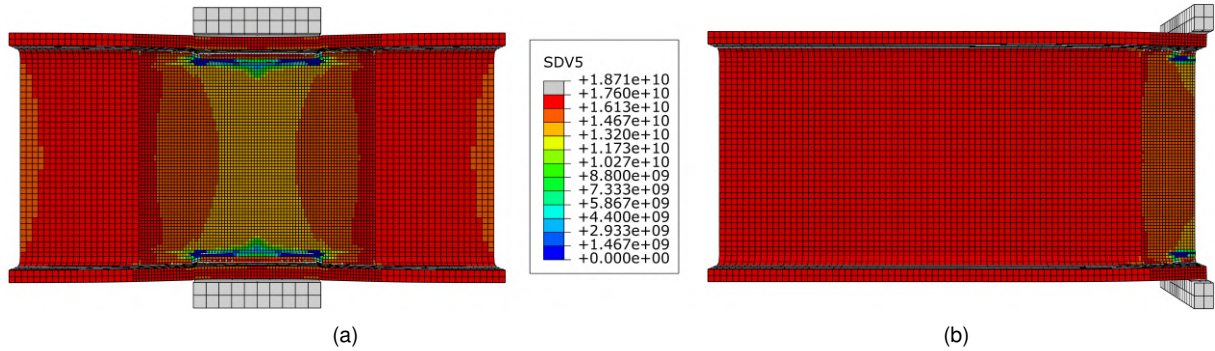


**Figure 5.14:** Web-crippling test - web-crushing failure of an I200-FC numerical model for different configurations: (a) ITF-100; (b) ETF-15.

Regarding I152-CP, both numerical models show clear signs of buckling and some signs of crushing (Figure 5.15), although the transverse elastic modulus due to crushing near the web-flange junction is not propagated through the entire thickness. In fact, the web's out-of-plane displacements induce high stresses in the more deformed web zones and those sections where compressive stresses are higher (concave side of the deformation) exhibit higher transverse elastic modulus degradation. This effect is more relevant in the ETF-100 configuration than in ITF-100, which is in line with the experimental data, since in the former crushing was registered and in the latter there was only buckling.

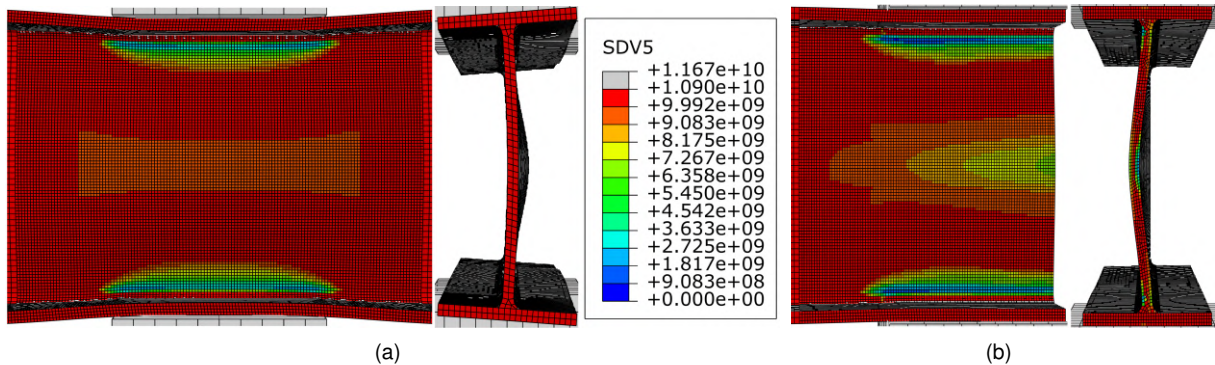


**Figure 5.15:** Web-crippling test - buckling and mixed failure of an I152-CP numerical model for different configurations: (a) ITF-100 (with a scale factor of 3); (b) ETF-100.

### 5.3.4 Double-lap tests

As mentioned earlier, the double-lap tests are mainly characterised by presence of high shear and compressive stresses that lead to ultimate failure. Given the author's doubts regarding which in-plane shear test method - *losipescu* or  $10^\circ$  off-axis tensile test - produces the better calibration parameters (see Section 4.3.6), several different sets of properties were used. These sets are summarised in Table 5.5 and are divided in: (i) "OAT", with all inputs directly retrieved from OAT tests, (ii) "OAT-vIS", with



calibration inputs ( $d_{4,max}$ ,  $m_4$ ,  $\gamma_{12,u}$  and  $r_{12}$ ) retrieved from OAT tests and mechanical properties ( $G_{12}$  and  $S_{12}$ ) retrieved from *losipescu* tests; (iii) “IS”, with all inputs directly retrieved from *losipescu* tests; (iv) “IS-vOAT”, with damage progression control inputs and maximum shear stress retrieved from *losipescu* tests, and residual strength control inputs and shear modulus from OAT tests; and (v) “OAT+IS”, with all parameters retrieved from the OAT test, except for the maximum shear stress.

Material	Set	$G_{12}$ [GPa]	$S_{12}$ [MPa]	$d_{4,max}$	$m_4$	$\gamma_{12,u}$	$r_{12}$
I150-AP	OAT	4.70	20.4	0.95	0.4	0.024	0.01
	OAT-vIS	3.01	46.8	0.95	0.4	0.024	0.01
	IS	3.01	46.8	0.95	5	1	1
	IS-vOAT	4.70	46.8	0.95	5	0.024	0.01
	OAT+IS	4.70	46.8	0.95	0.4	0.024	0.01
S120-AP	OAT	3.45	16.8	0.97	0.3	0.030	0.01
	OAT-vIS	3.45	41.4	0.97	0.3	0.030	0.01

**Table 5.5:** Double-lap test - different sets of in-plane shear calibration variables tested.

These different sets were used based on the experimental data available for each test and their stress vs. strain curves, although not shown, presented similar results to the ones already obtained in Chapter 4. For the I150-AP material, all data was available, however for S120-AP, the *losipescu* test data was incomplete, allowing only for the obtainment of the maximum shear stress.

Moreover, as was the case in Section 5.2.4, the numerical curves were adjusted for an easier comparison with the experimental scatter and the stiffness results are not valid for any comparison, hence they are omitted hereafter. Due to this approach, the different shear modulus obtained from *losipescu* and 10° OAT tests were not a subject of study in these results.

## Results

Figures 5.16 and 5.17 present the load vs. displacement curves obtained for different configurations, materials, and sets of properties, while Table 5.6 summarises the maximum loads values and their relative difference to experimental data. The numerical results were obtained for all different sets of calibration inputs only for DL-15 and DL-70 configurations, since they represent the two most extreme cases of failure characteristics. For DL-35 and DL-2B, only the most relevant sets of properties were tested, and DL-25 results are omitted due to their similarity to DL-15 tests regarding the general curve's behaviour and failure modes.

For the configuration DL-15 (Figure 5.16 a), the results obtained with different sets have considerable variability. When using “IS” properties, although the behaviour until failure is similar to experimental data (and a maximum load overestimation of 18.6%), after a first loss in stiffness, the load enters a new stage where it increases further, instead of the typical residual stress with considerably smaller loads. This effect was expected and happens because of the residual strength control input values of  $\gamma_{12,u} = 1$  and  $r_{12} = 1$ .

The results obtained with “OAT” and “OAT-vIS” lead to maximum load's overestimation of 14.3% and 22.7%, respectively, and present a very similar load vs. displacement curve behaviour. The higher

maximum load registered for “OAT-vIS” is associated directly with the higher maximum shear stress (*cf.* Table 5.6), and the decrease in stiffness near the maximum load occurs because of the small  $m_4$  used. As for “IS-vOAT”, a relative difference of 11.4% for the maximum load was registered. Additionally, there is practically no decrease in stiffness before the maximum load, in opposition to “OAT” and “OAT-vIS”, due to the higher  $m_4$  utilised, and the loss in stiffness after failure is more accentuated. Finally, using the set “OAT+IS” results in a much higher maximum load (relative difference of 53.4%), indicating that this combination of properties may not be a good approach.

Regarding the I150-AP-DL-70 configuration’s results shown in Figure 5.16 (b), the same pattern between different sets explained for DL-15 applies, although the variability between the maximum load predictions is smaller (maximum difference of 42 percentage points between “IS-vOAT” and “OAT+IS” for DL-15, and 19.6 p.p between the same sets for DL-70). Moreover, for “IS” properties, the residual load value is similar to other sets and is considerably lower than the experimental ones. This phenomenon relates to 2 different aspects: (i) the failure mode, which is mainly characterised by bearing failure and not shear-out, and (ii) the inability of the implicit analyses to “transfer” the stiffness of the material to the adjacent elements of the failed ones. In fact, this inability was already relevant in compact compression models (*cf.* Section 5.3.2) when analysing the premature failure near the load application holes. In the ABAQUS software, this problem could only be overcome with explicit analysis and element removal. As for S120-AP-DL-70, both sets of properties tested followed the same pattern as in the I150-AP material, although with considerably higher relative differences regarding the maximum load predictions (-37.0% for “OAT” properties and -29.2% for “OAT-vIS”).

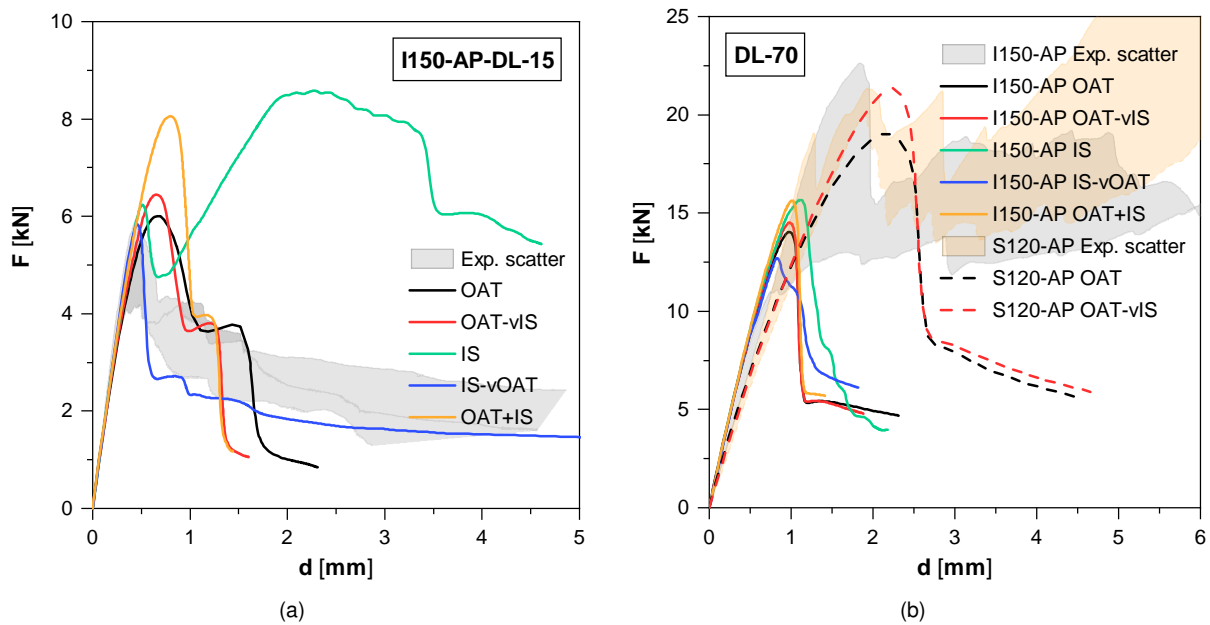


**Figure 5.16:** Double-lap test - experimental and numerical load vs. displacement curves with different calibration parameters for: (a) DL-15 configuration for I150-AP (b) DL-70 configuration for I150-AP and S120-AP.

Finally, for DL-35 (or 37, for S120-AP) and DL-2B configurations, the results obtained follow similar trends as in other configurations. While in I150-AP-DL-35 the maximum load values present small

differences ( $\approx 6\%$  for “OAT” and “IS-vOAT”, and  $10\%$  for OAT+IS), for S120-AP-DL-37 the loads are somewhat underestimated ( $-38.4\%$  for “OAT” and  $-12.4\%$  for “OAT-vIS”). For the double bolt (2B) configuration, both “OAT” and “IS-vOAT” properties produced proximate values with relative differences of  $26.9\%$  and  $18.7\%$ , respectively, and the set “OAT+IS” overestimated the result in  $52.1\%$ .

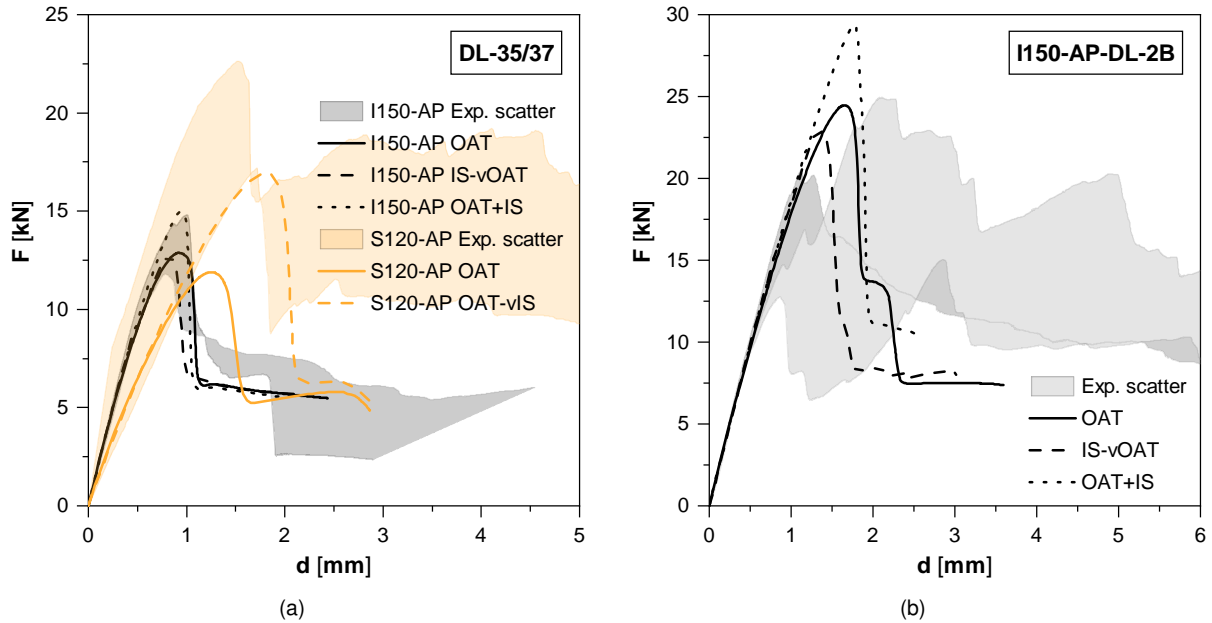


**Figure 5.17:** Web-crippling test - failure of an I152-CP numerical model for different configurations: (a) ITF-100 (with a scale factor of 3); (b) ETF-100.

Material	Set	$F_{max}$ [kN]									
		DL-15		DL-25		DL-35*		DL-70		DL-2B	
		Value	$\Delta$ (%)	Value	$\Delta$ (%)	Value	$\Delta$ (%)	Value	$\Delta$ (%)	Value	$\Delta$ (%)
I150-AP	OAT	6.00	14.3	9.41	-13.3	12.88	-5.8	14.04	-5.9	24.46	26.9
	OAT-vIS	6.45	22.7	-	-	-	-	14.51	-2.7	-	-
	IS	6.23	18.6	-	-	-	-	15.66	5.0	-	-
	IS-vOAT	5.85	11.4	9.25	-14.7	12.77	-6.6	12.70	-14.8	22.89	18.7
	OAT+IS	8.06	53.4	13.13	21.0	15.04	10.0	15.63	4.8	29.33	52.1
S120-AP	OAT	-	-	-	-	11.89	-38.4	19.02	-37.0	-	-
	OAT-vIS	-	-	-	-	16.93	-12.4	21.37	-29.2	-	-

**Table 5.6:** Double-lap test - maximum load results for different sets of properties.

\* For S120-AP, the edge distance is 37 mm.

## Failure modes

The failure modes registered in numerical models are mostly in line with experimental data presented in Chapter 3. For DL-15 and DL-25 configurations, the shear-out failure is visible for every set of properties, as shown in Figure 5.18 for the DL-15 configuration and for “OAT” and “IS-vOAT” properties. Additionally, the difference between sets of properties is also highlighted. When using the sets “OAT”, “OAT-vIS” and “OAT+IS”, shear modulus degradation (SDV7) occurs in large areas, with

most of the specimen experiencing a reduction in  $\approx 50\%$ , while the most affected area (the region near the extremities of the bolt between the bolt and the edge, as expected) experiences full degradation (Figure 5.18 (a)). For the set “IS-vOAT”, the shear modulus (total) degradation exclusively occurs between the bolt and the edge (through the entire thickness), with other areas remaining unaffected (Figure 5.18 b). These differences are readily justified by the exponential evolution variable  $m_4$  values (Table 5.5) - using a lower value leads to earlier degradation, therefore a larger region is affected, and the latter failure mode is in better agreement with the one verified experimentally.

As for the DL-70 configuration, Figure 5.19 shows the same effect between sets of properties regarding the shear modulus degradation as in DL-15. The bearing failure registered experimentally was not entirely captured in numerical simulations, even though there was significant shear modulus degradation. Some suggestions to improve these results are suggested in Section 6.2.

For the DL-35 and 37 configurations, none of the numerical simulations reached shear-out failure. However, these models presented convergence problems, and the failure modes were similar to DL-25 and DL-15, but with a less developed degradation stage, leading the author to believe that, had the models successfully converged, shear-out failure would have been registered.

Regarding the double bolt (2B) configuration, all sets of properties registered a mixed failure mode. The outer bolt (35 mm from the edge) produced induced shear-out failure, while the inner bolt (70 mm from the edge) induced total shear modulus degradation between the two bolts, as in the DL-70 results.

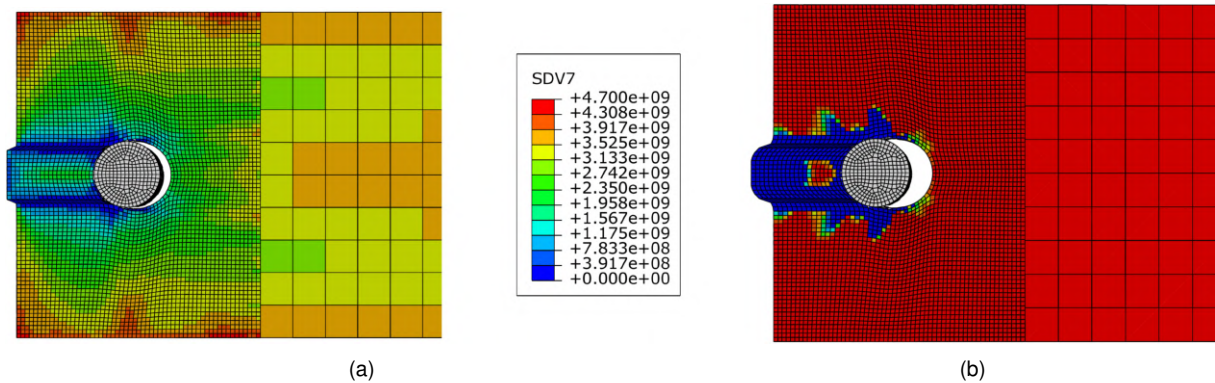


**Figure 5.18:** Double-lap test - numerical failure and shear modulus degradation (SDV7) of I150-AP-DL-15 for different sets of properties: (a) OAT; (b) IS-vOAT.

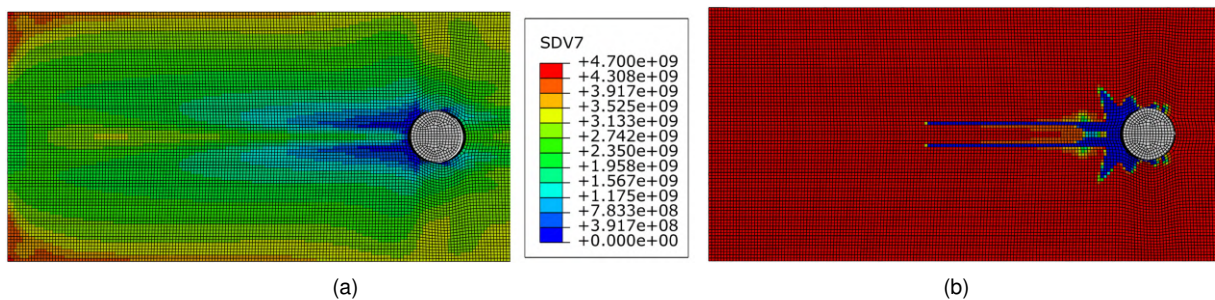


**Figure 5.19:** Double-lap test - numerical failure shear modulus degradation (SDV7) of I150-AP-DL-70 for different sets of properties: (a) OAT; (b) IS-vOAT.

## Chapter 6

# Conclusions and future developments

### 6.1 Conclusions

The main goal of this thesis was the assessment of the validity of a new progressive failure model for quasi-orthotropic pultruded FRPs. With this in mind, the calibration of the model for 6 new materials was performed, and the validation of the model was attested by simulating several application tests.

The calibration process for longitudinal tests (both tensile and compressive) is straightforward and precise, given their almost linear behaviour. Transverse tensile tests, due to their non-linearity, are more difficult to calibrate. Nevertheless, the model's approach allows for very good numerical vs experimental curve fitting, as demonstrated in Section 4.3.2. For transverse compressive tests, and because of the model's simplification of using only one elastic modulus for each direction (the tensile modulus was adopted), the curve fitting process is more difficult. Nonetheless, it is still possible to calibrate the materials, as shown in Section 4.3.4. *Iosipescu* tests were also successfully calibrated, although (i) for small  $m_2$  inputs there were some challenges regarding convergence problems and premature compressive damage onset, given that a compromise had to be reached between this test and the transverse compressive test, and (ii) the in-plane shear modulus was consistently underestimated in  $\approx 25\%$ , which is probably related to the uncertainty of the experimental test method. For the  $10^\circ$  OAT tests, the calibration was also deemed successful, with the only difficulty being associated with the very small  $m_4$  inputs, which led to significant damage onset regarding the shear modulus. The need to calibrate the mesh regularisation parameter with compact tension tests was also shown in Sections 4.2.3 and 4.3.7.

The application tests used to validate the model were also, in almost every case, successful. Compact tension and wide compact tension tests showed very good numerical vs experimental curve fitting in all stages, and maximum load predictions were mostly under a 10% relative difference with respect to experimental results. The failure modes were also well depicted, with crack propagation and even compressive failure on the opposite side of the notch (with out-of-plane displacements) evident in numerical models. Compact compression tests, however, presented more intricate results, with an early damage onset near the load application holes that hindered the development of the softening stage in the numerical models. Nonetheless, for materials with similar  $E_{22}^+$  and  $E_{22}^-$ , maximum load relative dif-

ferences were under 12%. Web-crippling tests that presented only web-crushing failure were also well depicted, with maximum load and stiffness relative differences lower than 20%. These could be lowered to  $\approx 9\%$  by using  $E_{22}^-$  instead of  $E_{22}^+$  as an input. Web-crippling tests with mixed failure modes (buckling and crushing), where non-linear analyses were used, showed excellent results for I sections regarding maximum load, stiffness and failure mode predictions, but largely overestimated the maximum load and stiffness predictions for U sections. These overestimations were due to the inability to correctly model the initial imperfections with the software used.

Finally, regarding the double-lap tests and the comparison between different sets of properties used, the main conclusions are: (i) the use of properties fully retrieved from *losipescu* tests is not appropriate to predict shear-out failure, given the limitations of the residual strength parameters; (ii) the use of a low exponential parameter, retrieved from the OAT test, induces a more accentuated loss in stiffness near the maximum load, which is not in agreement with the experimental behaviour, unlike using a larger exponential parameter, from the *losipescu* test; (iii) for all configurations except those with very large edge distance, the set of mixed properties “IS-vOAT” presents better agreement with experimental data. In order to correctly model the specimens with very large edge distance, element removal should be implemented, which would require an explicit analysis that is out of the scope of the present work.

Overall, the results presented in this work show that it is possible to predict the failure loads, modes, and post-failure behaviour under several different actions, for a significant range of pultruded GFRP materials.

## 6.2 Future developments

To improve the results obtained in this study, the author identified two different subjects where modifying the UMAT would lead to better numerical vs experimental agreement. The first suggestion is to adopt both tensile and compressive elastic moduli as separate inputs which would allow for a better calibration without needing to compromise the curve’s shape, and would also increase the prediction capabilities of application tests where both tensile and compressive stresses are present. This only adds two more inputs to the already extensive list, and no further calibration tests would be needed. Another suggestion would be to modify the current UMAT to a VUMAT - used for explicit analyses - which allow for element removal and would better predict, for example, the bearing failure effect in the DL-70 test.

As for further testing of the proposed failure progression model, new studies should be focused on application tests where the longitudinal stresses are predominant and ultimately cause delamination. Given the model’s simplification of considering FRPs as a homogeneous material, it would be interesting to understand if the numerical results match that experimental data. Moreover, and specifically regarding the web-crippling results obtained for U sections in this work, the results should be improved by, for example, manually introducing an initial imperfection that simulates the real behaviour of the material, and by studying the amplitude of the deformation which is more in line with real profiles.

# Bibliography

- [1] M. K. Buragohain. *Composite Structures: Design, Mechanics, Analysis, Manufacturing, and Testing*. CRC Press, Boca Raton, FL, 1<sup>st</sup> edition, 2017.
- [2] M. Hinton, A. Kaddour, and P. Soden. *Failure Criteria in Fibre-Reinforced-Polymer Composites: The World-wide Failure Exercise*. Elsevier, Oxford, 2004. <https://doi.org/10.1016/B978-008044475-8/50002-0>.
- [3] J. A. Gonilha, N. Silvestre, J. R. Correia, V. Tita, and D. Martins. Novel progressive failure model for quasi-orthotropic pultruded FRP structures: Formulation and calibration of parameters (Part I). *Composite Structures*, 255:112974, Jan 2021. <https://doi.org/10.1016/j.compstruct.2020.112974>.
- [4] S. Tsai. Strength characteristics of composite materials. *NASA CR-224*, 1965. Available at: <https://ntrs.nasa.gov/api/citations/19650012040/downloads/19650012040.pdf>.
- [5] Z. Hashin. Failure criteria for unidirectional fiber composites. *Journal of Applied Mechanics*, 47(2): 329–334, Jun 1980. <https://doi.org/10.1115/1.3153664>.
- [6] F. Nunes, M. Correia, J. R. Correia, N. Silvestre, and A. Moreira. Experimental and numerical study on the structural behavior of eccentrically loaded GFRP columns. *Thin-Walled Structures*, 72:175–187, 2013. <https://doi.org/10.1016/j.tws.2013.07.002>.
- [7] J. A. Gonilha, J. R. Correia, and F. A. Branco. Structural behaviour of a GFRP-concrete hybrid footbridge prototype: Experimental tests and numerical and analytical simulations. *Engineering Structures*, 60:11–22, 2014. <https://doi.org/10.1016/j.engstruct.2013.12.018>.
- [8] L. A. Fernandes, F. Nunes, N. Silvestre, J. R. Correia, and J. Gonilha. GFRP pultruded profiles. Part 2: Numerical analysis and design. *Composite Structures*, 120:578–590, 2015. <https://doi.org/10.1016/j.compstruct.2014.09.026>.
- [9] F. Nunes, N. Silvestre, and J. R. Correia. Structural behaviour of hybrid FRP pultruded columns. Part 2: Numerical study. *Composite Structures*, 139:304–319, 2016. <https://doi.org/10.1016/j.compstruct.2015.12.059>.
- [10] A. Matzenmiller, J. Lubliner, and R. L. Taylor. A constitutive model for anisotropic damage in

- fiber-composites. *Mechanics of Materials*, 20(2):125–152, 1995. [https://doi.org/10.1016/0167-6636\(94\)00053-0](https://doi.org/10.1016/0167-6636(94)00053-0).
- [11] A. Puck and H. Schürmann. Failure Analysis of FRP Laminates by Means of Physically Based Phenomenological Models. *Composites Science and Technology*, 58(7):1045–1067, Jul 1998. [https://doi.org/10.1016/S0266-3538\(96\)00140-6](https://doi.org/10.1016/S0266-3538(96)00140-6).
- [12] K. V. Williams, R. Vaziri, and A. Poursartip. A physically based continuum damage mechanics model for thin laminated composite structures. *International Journal of Solids and Structures*, 40(9):2267–2300, Jan 2003. [https://doi.org/10.1016/S0020-7683\(03\)00016-7](https://doi.org/10.1016/S0020-7683(03)00016-7).
- [13] C. G. Dávila, P. P. Camanho, and C. A. Rose. Failure Criteria for FRP Laminates. *Journal of Composite Materials*, 39(4):323–345, Feb 2005. <https://doi.org/10.1177/0021998305046452>.
- [14] S. T. Pinho, L. Iannucci, and P. Robinson. Physically-based failure models and criteria for laminated fibre-reinforced composites with emphasis on fibre kinking: Part I: Development. *Composites Part A: Applied Science and Manufacturing*, 37(1):63–73, 2006. <https://doi.org/10.1016/j.compositesa.2005.04.016>.
- [15] M. V. Donadon, S. F. M. de Almeida, M. A. Arbelo, and A. R. de Faria. A Three-Dimensional Ply Failure Model for Composite Structures. *International Journal of Aerospace Engineering*, 2009, Jan 2009. <https://doi.org/10.1155/2009/486063>.
- [16] J. A. Gonilha, N. Silvestre, J. R. Correia, V. Tita, and L. Almeida-Fernandes. Novel progressive failure model for quasi-orthotropic pultruded FRP structures: Application to compact tension and web-crippling case studies (Part II). *Composite Structures*, 255:112973, 2021. ISSN 0263-8223. <https://doi.org/10.1016/j.compstruct.2020.112973>.
- [17] D. Gay. *Composite Materials: Design and Applications*. CRC Press, Boca Raton, FL, 3<sup>rd</sup> edition, 2015.
- [18] R. M. Jones. *Mechanics of Composite Materials*. Taylor & Francis, 2<sup>nd</sup> edition, 1975.
- [19] P. P. Camanho. Failure criteria for fibre-reinforced polymer composites. *Secção de Mecânica Aplicada, Departamento de Engenharia Mecânica e Gestão Industrial, Faculdade de Engenharia da Universidade do Porto*, 2002. Available at: <https://paginas.fe.up.pt/~stpinho/teaching/feup/y0506/fcriteria.pdf>.
- [20] S. Tsai and E. Wu. A general theory of strength for anisotropic materials. *Journal of Composite Materials*, 5(1):58–80, Jan 1971. <https://doi.org/10.1177/002199837100500106>.
- [21] SIMULIA. *ABAQUS Version 6.13 Document Collection*. Dassault Systèmes, 2013.
- [22] P. Schubel, J.-J. Luo, and I. Daniel. Through-thickness Characterization of Thick Composite Laminates. *Proceedings of the 2006 SEM Annual Conference and Exposition on Experimental and Applied Mechanics 2006*, 4:1793–1800, Jan 2006.



- [23] R. Govender, L. A. Louca, A. Pullen, A. Soleiman Fallah, and G. Nurick. Determining the through-thickness properties of thick glass fiber reinforced polymers at high strain rates. *Journal of Composite Materials*, 46:1219–1228, May 2012. <https://doi.org/10.1177/0021998311415444>.
- [24] X. Qian, H. Wang, D. Zhang, and G. Wen. High strain rate out-of-plane compression properties of aramid fabric reinforced polyamide composite. *Polymer Testing*, 53:314–322, 2016. <https://doi.org/10.1016/j.polymertesting.2016.06.006>.
- [25] L. C. Bank. *Composites for Construction: Structural Design with FRP Materials*. John Wiley & Sons, Hoboken, New Jersey, 2006.
- [26] A. Vedernikov, A. Safonov, F. Tucci, P. Carlone, and I. Akhatov. Pultruded materials and structures: A review. *Journal of Composite Materials*, 54(26):4081–4117, Nov 2020. <https://doi.org/10.1177/0021998320922894>.
- [27] ACI Committee 440. *State-of-the-art report on fiber reinforced plastic (FRP) reinforcement for concrete structures*, 1996. Available at: <https://tinyurl.com/j8nt4rvw>.
- [28] K. K. Chawla. *Composite Materials: Science and Engineering*. Springer, 4<sup>th</sup> edition, 2019. ISBN 9783030289829.
- [29] M. Leite Ribeiro. *Damage and progressive failure analysis for aeronautic composite structures with curvature*. PhD thesis, University of São Paulo, São Carlos School of Engineering, and Catholic University of Leuven, Faculty of Engineering Science, 2013.
- [30] S. T. Pinho, R. Gutkin, S. Pimenta, N. V. De Carvalho, and P. Robinson. 7 - Fibre-dominated compressive failure in polymer matrix composites. In *Woodhead Publishing Series in Composites Science and Engineering*, pages 183–223. Woodhead Publishing, 2012. <https://doi.org/10.1533/9780857095329.1.183>.
- [31] T. L. Anderson. *Fracture Mechanics : Fundamentals and Applications*. CRC Press, Boca Raton, 4<sup>th</sup> edition, 2017.
- [32] M. Nikbakht, J. Yousefi, H. Hosseini-Toudeshky, and G. Minak. Delamination evaluation of composite laminates with different interface fiber orientations using acoustic emission features and micro visualization. *Composites Part B: Engineering*, 113:185–196, 2017. <https://doi.org/10.1016/j.compositesb.2016.11.047>.
- [33] C. Sun, B. Quinn, and J. Tao. Comparative Evaluation of Failure Analysis Methods for Composite Laminates. *U.S. Department of Transportation*, May 1996. Available at: <http://www.tc.faa.gov/its/worldpac/techrpt/ar95-109.pdf>.
- [34] R. M. Christensen. *The Theory of Materials Failure*. OUP Oxford, Oxford, 1<sup>st</sup> edition, 2013. ISBN 9780199662111.
- [35] Hill Rodney. *The Mathematical Theory of Plasticity*. Oxford University Press, London, 1950.

- [36] O. Hoffman. The Brittle Strength of Orthotropic Materials. *Journal of Composite Materials*, 1(2): 200–206, Apr 1967. <https://doi.org/10.1177/002199836700100210>.
- [37] H. Thom. A review of the biaxial strength of fibre-reinforced plastics. *Composites Part A: Applied Science and Manufacturing*, 29(8):869–886, 1998. [https://doi.org/10.1016/S1359-835X\(97\)00090-0](https://doi.org/10.1016/S1359-835X(97)00090-0).
- [38] Z. Hashin and A. Rotem. A fatigue failure criterion for fiber reinforced materials. *Journal of Composite Materials*, 7(4):448–464, Oct 1973.
- [39] P. Camanho, S. Bowron, and F. Matthews. Failure Mechanisms in Bolted CFRP. *Journal of Reinforced Plastics and Composites*, 17(3):205–233, Feb 1998. <https://doi.org/10.1177/073168449801700302>.
- [40] K. C. Warren, R. A. Lopez-Anido, S. S. Vel, and H. H. Bayraktar. Progressive failure analysis of three-dimensional woven carbon composites in single-bolt, double-shear bearing. *Composites Part B: Engineering*, 84:266–276, 2016. <https://doi.org/10.1016/j.compositesb.2015.08.082>.
- [41] A. M. G. Coelho and J. T. Mottram. Numerical Evaluation of Pin-Bearing Strength for the Design of Bolted Connections of Pultruded FRP Material. *Journal of Composites for Construction*, 21(5): 4017027, Oct 2017. [https://doi.org/10.1061/\(ASCE\)CC.1943-5614.0000809](https://doi.org/10.1061/(ASCE)CC.1943-5614.0000809).
- [42] M. Akterskaia, P. P. Camanho, E. Jansen, A. Arteiro, and R. Rolfes. Progressive delamination analysis through two-way global-local coupling approach preserving energy dissipation for single-mode and mixed-mode loading. *Composite Structures*, 223:110892, 2019. <https://doi.org/10.1016/j.compstruct.2019.110892>.
- [43] F. Zhuang, A. Arteiro, C. Furtado, P. Chen, and P. P. Camanho. Mesoscale modelling of damage in single- and double-shear composite bolted joints. *Composite Structures*, 226:111210, 2019. <https://doi.org/10.1016/j.compstruct.2019.111210>.
- [44] L. Almeida-Fernandes. *Fracture behaviour of pultruded GFRP profiles: application to web-crippling phenomena*. PhD thesis, Instituto Superior Técnico, December 2020.
- [45] L. Almeida-Fernandes, N. Silvestre, and J. R. Correia. Characterization of transverse fracture properties of pultruded GFRP material in tension. *Composites Part B: Engineering*, 175:107095, 2019. <https://doi.org/10.1016/j.compositesb.2019.107095>.
- [46] L. Almeida-Fernandes, N. Silvestre, J. R. Correia, and M. R. T. Arruda. Fracture toughness-based models for damage simulation of pultruded GFRP materials. *Composites Part B: Engineering*, 186: 107818, 2020. <https://doi.org/10.1016/j.compositesb.2020.107818>.
- [47] L. Almeida-Fernandes, N. Silvestre, J. R. Correia, and M. Arruda. Compressive transverse fracture behaviour of pultruded GFRP materials: Experimental study and numerical calibration. *Composite Structures*, 247:112453, 2020. <https://doi.org/10.1016/j.compstruct.2020.112453>.

- [48] L. Almeida-Fernandes, J. R. Correia, and N. Silvestre. Effect of fibre layup and bearing length on the web-crippling behaviour of pultruded GFRP profiles. *Composite Structures*, 267:113884, 2021. <https://doi.org/10.1016/j.compstruct.2021.113884>.
- [49] L. A. Fernandes, J. Gonilha, J. R. Correia, N. Silvestre, and F. Nunes. Web-crippling of GFRP pultruded profiles. Part 1: Experimental study. *Composite Structures*, 120:565–577, 2015. <https://doi.org/10.1016/j.compstruct.2014.09.027>.
- [50] D. Martins, M. Proença, J. R. Correia, J. Gonilha, M. Arruda, and N. Silvestre. Development of a novel beam-to-column connection system for pultruded gfrp tubular profiles. *Composite Structures*, 171:263–276, 2017. <https://doi.org/10.1016/j.compstruct.2017.03.049>.
- [51] D. Martins, J. Gonilha, J. R. Correia, and N. Silvestre. Exterior beam-to-column bolted connections between GFRP I-shaped pultruded profiles using stainless steel cleats. Part 1: Experimental study. *Thin-Walled Structures*, 163, Jun 2021. <https://doi.org/10.1016/j.tws.2021.107719>.
- [52] ISO 527-4. *Determination of tensile properties - Test conditions for isotropic and orthotropic fibre-reinforced plastic composites*. International Organization for Standardization, Geneva, Switzerland, 1997.
- [53] ASTM D6641/D6641M – 09. *Standard test method for compressive properties of polymer matrix composite materials using a combined loading compression (CLC) test fixture*. American Society for Testing and Materials, West Conshohocken, PA, USA, 2009.
- [54] ASTM D 695. *Standard Test Method for Compressive Properties of Rigid Plastics*. American Society for Testing and Materials, West Conshohocken, PA, USA, 2002.
- [55] P. M. Wegner and D. F. Adams. Verification of the Combined Load Compression (CLC) Test Method. *U.S. Department of Transportation*, Aug 2000. Available at: <https://www.tc.faa.gov/its/worldpac/techrpt/ar00-26.pdf>.
- [56] ASTM D5379/D5379M. *Standard test method for shear properties of composites materials by the v-notched beam method*. American Society for Testing and Materials, West Conshohocken, PA, USA, 2005.
- [57] J. M. Hodgkinson. *Mechanical Testing of Advanced Fibre Composites*. Woodhead Publishing, Boca Raton, FL, 2000. ISBN 9781855733121.
- [58] M.-J. Pindera, G. Choksi, J. Hidde, and C. Herakovich. A Methodology for Accurate Shear Characterization of Unidirectional Composites. *Journal of Composite Materials*, 21(12):1164–1184, Jan 1987. <https://doi.org/10.1177/002199838702101205>.
- [59] F. Pierron and A. Vautrin. The 10 ° off-axis tensile test: A critical approach. *Composites Science and Technology*, 56(4):483–488, 1996. [https://doi.org/10.1016/0266-3538\(96\)00004-8](https://doi.org/10.1016/0266-3538(96)00004-8).

- [60] H. Ho, M. Y. Tsai, J. Morton, and G. L. Farley. A comparison of three popular test methods for determining the shear modulus of composite materials. *Composites Engineering*, 3(1):69–81, 1993. [https://doi.org/10.1016/0961-9526\(93\)90032-F](https://doi.org/10.1016/0961-9526(93)90032-F).
- [61] N. J. Pagano and J. C. Halpin. Influence of End Constraint in the Testing of Anisotropic Bodies. *Journal of Composite Materials*, 2(1):18–31, Jan 1968. <https://doi.org/10.1177/002199836800200102>.
- [62] A. F. Bower. *Applied mechanics of solids*. CRC Press. Taylor & Francis, Boca Raton, FL, 1<sup>st</sup> edition, 2009.
- [63] G. J. Turvey and Y. Zhang. A computational and experimental analysis of the buckling, postbuckling and initial failure of pultruded GRP columns. *Computers and Structures*, 84(22):1527–1537, Jan 2006. <https://doi.org/10.1016/j.compstruc.2006.01.028>.
- [64] L. Feo, A. S. Mosallam, and R. Penna. Mechanical behavior of web–flange junctions of thin-walled pultruded I-profiles: An experimental and numerical evaluation. *Composites Part B: Engineering*, 48:18–39, 2013. <https://doi.org/10.1016/j.compositesb.2012.11.001>.
- [65] A. Quadrino, R. Penna, L. Feo, and N. Nisticò. Mechanical characterization of pultruded elements: Fiber orientation influence vs web-flange junction local problem. experimental and numerical tests. *Composites Part B: Engineering*, 142:68–84, 2018. <https://doi.org/10.1016/j.compositesb.2018.01.001>.

## Appendix A

# Additional background on the new progressive failure model

$$A_{11} = \frac{S_{11}^+ - C_{11}}{\sqrt{1 - \left(\frac{C_{22}}{A_{22}}\right)^2}} \quad (\text{A.1})$$

$$A_{22} = \sqrt{\frac{(S_{22}^+ - C_{22})^2 - \left(\frac{C_{11}C_{22}}{S_{11}^+ - C_{11}}\right)^2}{1 - \left(\frac{C_{11}}{S_{11}^+ - C_{11}}\right)^2}} \quad (\text{A.2})$$

$$A_{12} = \frac{S_{12}}{\sqrt{1 - \left(\frac{C_{11}}{A_{11}}\right)^2 - \left(\frac{C_{22}}{A_{22}}\right)^2}} \quad (\text{A.3})$$

$$A_{33} = S_{33}^+ + |S_{33}^-| \quad (\text{A.4})$$

$$A_{13} = \frac{S_{13}}{\sqrt{1 - \left(\frac{C_{33}}{A_{33}}\right)^2}} \quad (\text{A.5})$$

$$A_{23} = \frac{S_{23}}{\sqrt{1 - \left(\frac{C_{33}}{A_{33}}\right)^2}} \quad (\text{A.6})$$

## Appendix B

# Summary of experimental results

Property		I200-FC		I150-ST		I152-CP		U150-ST		S120-AP
		W	F	W	F	W	F	W	F	-
$E_{11}^+$ [GPa]	Average	29.6	35.3	29.4	33.9	25.2	26.8	26.6	27.3	32.7
	CoV (%)	5.3	6.3	8.2	6.9	5.9	1.5	5.2	2.1	9.3
$S_{11}^+$ [MPa]	Average	322.6	316.8	376.4	385.3	426.0	466.7	347.1	373.6	326.2
	CoV (%)	3.2	5.9	4.8	5.4	3.4	1.4	2.9	0.2	5.2
$E_{22}^+$ [GPa]	Average	17.6	-	8.4	-	10.9	-	8.7	-	-
	CoV (%)	18.1	-	12.6	-	7.3	-	15.0	-	-
$S_{22}^+$ [MPa]	Average	70.7	-	33.8	-	121.3	-	69.5	-	-
	CoV (%)	2.6	-	17.9	-	7.0	-	8.8	-	-
$E_{11}^-$ [GPa]	Average	29.9	-	28.1	-	24.6	-	25.8	-	21.2
	CoV (%)	6.3	-	11.9	-	3.0	-	10.1	-	15.3
$S_{11}^-$ [MPa]	Average	441.5	-	550.5	-	436.9	-	450.6	-	435.1
	CoV (%)	6.5	-	12.8	-	6.0	-	5.1	-	12.1
$E_{22}^-$ [GPa]	Average	10.9	-	12.9	-	11.3	-	7.0	-	4.8
	CoV (%)	11.2	-	14.7	-	7.3	-	7.1	-	17.6
$S_{22}^-$ [MPa]	Average	121.6	-	122.9	-	104.2	-	83.5	-	88.9
	CoV (%)	13.7	-	6.1	-	10.6	-	8.5	-	18.3
$G_{12}$ [GPa] <sup>1</sup>	Average	2.89	3.06	3.17	3.50	4.24	-	4.16	-	-
	CoV (%)	12.1	10.1	11.0	4.1	15.0	-	14.2	-	-
$S_{12}$ [MPa] <sup>1</sup>	Average	67.1	69.3	69.8	66.2	65.3	-	70.8	-	41.4
	CoV (%)	2.9	4.2	7.0	6.5	3.3	-	8.7	-	15.0
$G_{12}$ [GPa] <sup>2</sup>	Average	-	-	-	-	-	-	-	-	3.45
	CoV (%)	-	-	-	-	-	-	-	-	12.6
$S_{12}$ [MPa] <sup>2</sup>	Average	-	-	-	-	-	-	-	-	16.8
	CoV (%)	-	-	-	-	-	-	-	-	19.9

**Table B.1:** Average and co-variation of all materials' mechanical properties.

<sup>1</sup> Results obtained with *Iosipescu* tests.

<sup>2</sup> Results obtained with 10° Off-Axis Tensile tests.

Test	Property		I200-FC	I150-ST	I152-CP	U150-ST
CT-30	$K$ [kN/mm]	Average	5.75	4.15	4.12	3.83
		CoV (%)	7.2	2.3	2.3	8.4
	$F_{\max}$ [kN]	Average	3.11	1.55	4.66	2.62
		CoV (%)	6.4	1.7	4.4	3.9
CT-35	$K$ [kN/mm]	Average	2.70	2.63	2.54	2.44
		CoV (%)	4.4	5.2	10.0	8.0
	$F_{\max}$ [kN]	Average	1.96	1.17	2.92	1.81
		CoV (%)	7.4	5.5	3.1	1.7
WCT-30	$K$ [kN/mm]	Average	7.19	5.18	5.47	5.02
		CoV (%)	9.9	11.9	-	2.9
	$F_{\max}$ [kN]	Average	5.52	2.80	4.82	4.70
		CoV (%)	4.9	8.1	-	2.7
WCT-40 <sup>3</sup>	$K$ [kN/mm]	Average	4.20	3.11	2.62	2.92
		CoV (%)	10.4	8.4	13.0	4.8
	$F_{\max}$ [kN]	Average	4.76	2.33	4.85	3.79
		CoV (%)	2.3	3.4	6.7	7.0
CC-40	$K$ [kN/mm]	Average	12.9	10.3	9.7	10.2
		CoV (%)	6.5	3.9	9.6	6.1
	$F_{\max}$ [kN]	Average	11.8	11.7	7.8	8.3
		CoV (%)	7.0	2.2	4.1	2.8
CC-45	$K$ [kN/mm]	Average	11.1	8.0	-	9.1
		CoV (%)	-	9.3	-	-
	$F_{\max}$ [kN]	Average	10.7	10.4	-	7.14
		CoV (%)	-	2.0	-	-
WC-ITF-100	$K$ [kN/mm]	Average	123.2	91.0	85.1	37.2
		CoV (%)	2.8	2.1	4.4	9.3
	$F_{\max}$ [kN]	Average	131.2	91.4	72.3	25.7
		CoV (%)	2.1	9.7	3.6	0.6
WC-ETF-15	$K$ [kN/mm]	Average	32.9	21.6	-	-
		CoV (%)	7.8	4.2	-	-
	$F_{\max}$ [kN]	Average	32.0	24.3	-	-
		CoV (%)	4.3	1.7	-	-
WC-ETF-100	$K$ [kN/mm]	Average	-	-	66.4	25.9
		CoV (%)	-	-	11.6	0.9
	$F_{\max}$ [kN]	Average	-	-	51.7	1.8
		CoV (%)	-	-	20.6	4.9

**Table B.2:** Average and co-variation of CT, WCT, CC and WC test results.

<sup>3</sup> For I200-FC, the notch length is 38 mm.

Test	Property		I150-AP <sup>4</sup>	S120-AP
DL-15	$K$ [kN/mm]	Average	14.3	-
		CoV (%)	10.6	-
	$F_{\max}$ [kN]	Average	5.3	-
		CoV (%)	16.9	-
DL-25	$K$ [kN/mm]	Average	17.4	-
		CoV (%)	13.8	-
	$F_{\max}$ [kN]	Average	10.8	-
		CoV (%)	1.7	-
DL-35 <sup>5</sup>	$K$ [kN/mm]	Average	20.1	12.9
		CoV (%)	7.1	17.6
	$F_{\max}$ [kN]	Average	13.7	19.3
		CoV (%)	12.0	9.9
DL-70	$K$ [kN/mm]	Average	18.9	13.0
		CoV (%)	1.2	15.1
	$F_{\max}$ [kN]	Average	14.9	30.2
		CoV (%)	6.5	7.6
DL-2B	$K$ [kN/mm]	Average	19.3	-
		CoV (%)	23.0	-
	$F_{\max}$ [kN]	Average	19.9	-
		CoV (%)	6.0	-

**Table B.3:** Average and co-variation of DL results.

<sup>4</sup> All results were obtained using plates with the same fibre architecture and matrix as I150-AP.

<sup>5</sup> For S120-AP, the edge distance is 37 mm.



## Appendix C

### Finite element models

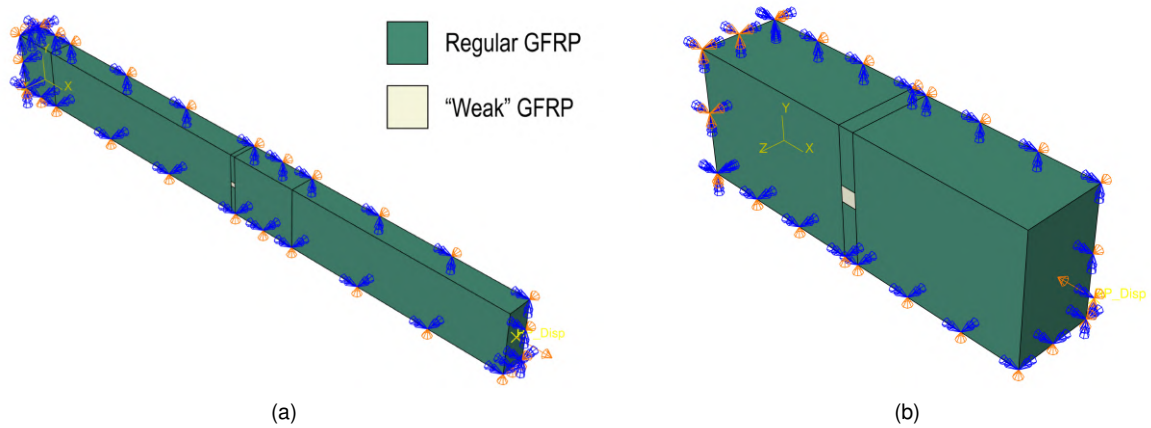


**Figure C.1:** Boundary conditions' model view for different tests: (a) tensile test; (b) compressive test.

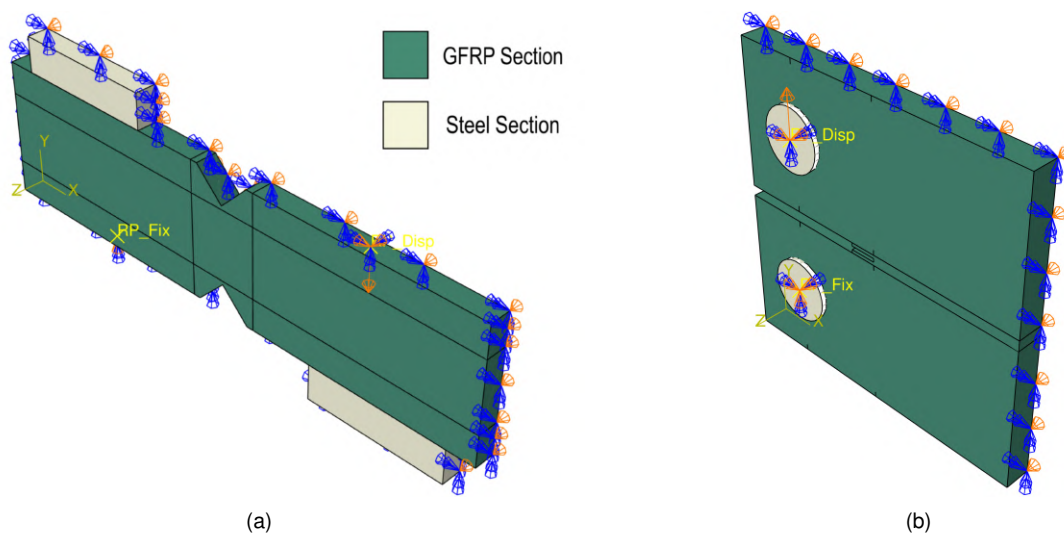


**Figure C.2:** Boundary conditions' model view for different tests: (a) *losipescu* test; (b) compact tension test.

## Appendix D

### Damage model input data

Parameter	I200-FC		I150-AP		I150-ST		I152-CP		U150-ST		S120-AP
	W	F	W	F	W	F	W	F	W	F	-
$E_{11}$ [GPa]	29.6	35.3	43.4	39.6	29.4	33.9	25.2	26.9	26.6	27.3	32.7
$E_{22}$	17.6	17.3	9.4	9.5	8.41	8.41	10.9	10.9	8.7	8.7	4.8
$E_{33}$	3.5	3.5	3.5	3.5	3.5	3.5	3.5	3.5	3.5	3.5	3.5
$\nu_{12}$ -	0.24	0.24	0.23	0.29	0.23	0.23	0.23	0.23	0.23	0.23	0.30
$\nu_{13}$	0.24	0.24	0.23	0.29	0.23	0.23	0.23	0.23	0.23	0.23	0.30
$\nu_{23}$	0.30	0.30	0.30	0.30	0.30	0.30	0.30	0.30	0.30	0.30	0.30
$G_{12}$ [GPa]	2.9	2.9	4.7	4.7	3.2	3.5	4.2	4.2	4.2	4.2	3.5
$G_{13}$	2.9	2.9	4.7	4.7	3.2	3.5	4.2	4.2	4.2	4.2	3.5
$G_{23}$	2.9	2.9	4.7	4.7	3.2	3.5	4.2	4.2	4.2	4.2	3.5
$S_{11}^+$ [MPa]	322.6	316.8	388.0	353.5	376.4	385.3	426.0	466.7	347.1	373.6	326.2
$S_{11}^-$	441.5	441.5	461.9	461.9	550.5	550.5	436.9	436.9	450.6	450.6	435.1
$S_{22}^+$	41.3	41.3	15.2	15.2	20.0	20.0	69.6	69.6	21.6	21.4	15.2
$S_{22}^-$	121.6	121.6	64.2	64.2	122.9	122.9	104.2	104.2	83.5	83.5	88.9
$S_{33}^+$	8.0	8.0	8.0	8.0	8.0	8.0	8.0	8.0	8.0	8.0	8.0
$S_{33}^-$	90.0	90.0	90.0	90.0	90.0	90.0	90.0	90.0	90.0	90.0	90.0
$S_{12}$	67.1	69.3	46.8	47.9	69.8	66.2	65.3	65.3	70.8	70.8	41.4
$S_{13}$	27.0	27.0	27.0	31.2	27.0	27.0	27.0	27.0	27.0	27.0	27.0
$S_{23}$	8.1	8.1	8.1	6.3	8.1	8.1	8.1	8.1	8.1	8.1	8.1

**Table D.1:** Input data for FE models: mechanical properties for all materials.

Parameter	I200-FC		I150-AP		I150-ST		I152-CP		U150-ST		S120-AP
	W	F	W	F	W	F	W	F	W	F	-
$d_{1,max}^+$	0.001	0.001	0.001	0.001	0.001	0.001	0.001	0.001	0.001	0.001	0.001
$d_{1,max}^-$	0.001	0.001	0.001	0.001	0.001	0.001	0.001	0.001	0.001	0.001	0.001
$d_{2,max}^+$	0.8	0.8	0.55	0.55	0.8	0.8	0.6	0.6	0.6	0.6	0.55
$d_{2,max}^-$	0.4	0.4	0.5	0.5	0.4	0.4	0.2	0.2	0.4	0.4	0.5
$d_{3,max}^+$	0.9	0.9	0.9	0.9	0.9	0.9	0.9	0.9	0.9	0.9	0.9
$d_{3,max}^-$	0.001	0.001	0.001	0.001	0.001	0.001	0.001	0.001	0.001	0.001	0.001
$d_{4,max}$	0.95	0.95	0.95	0.95	0.99	0.98	0.90	0.90	0.95	0.95	0.97
$d_{5,max}$	0.5	0.5	0.5	0.5	0.5	0.5	0.5	0.5	0.5	0.5	0.5
$d_{6,max}$	0.5	0.5	0.5	0.5	0.5	0.5	0.5	0.5	0.5	0.5	0.5
$m_1^+$	10	10	10	10	10	10	10	10	10	10	10
$m_1^-$	10	10	10	10	10	10	10	10	10	10	10
$m_2^+$	0.8	0.8	1	1	0.8	0.8	1	1	0.8	0.8	1
$m_2^-$	0.7	0.7	10	10	2	2	5	5	0.5	0.5	10
$m_3^+$	100	100	100	100	100	100	100	100	100	100	100
$m_3^-$	100	100	100	100	100	100	100	100	100	100	100
$m_4$	5	5	5	5	5	5	5	5	5	5	0.3
$m_5$	1	1	1	1	1	1	1	1	1	1	1
$m_6$	100	100	100	100	100	100	100	100	100	100	100
$\epsilon_{11,u}^+$	0.011	0.009	0.009	0.009	0.013	0.012	0.017	0.018	0.013	0.014	0.011
$\epsilon_{11,u}^-$	0.015	0.015	0.011	0.012	0.020	0.020	0.018	0.018	0.017	0.017	0.021
$\epsilon_{22,u}^+$	0.011	0.011	0.010	0.010	0.011	0.011	0.019	0.019	0.017	0.017	0.010
$\epsilon_{22,u}^-$	0.010	0.010	0.010	0.010	0.015	0.015	0.010	0.010	0.013	0.013	0.018
$\epsilon_{33,u}^+$	1	1	1	1	1	1	1	1	1	1	1
$\epsilon_{33,u}^-$	1	1	1	1	1	1	1	1	1	1	1
$\gamma_{12,u}$	1	1	0.024	0.024	1	1	1	1	1	1	0.030
$\gamma_{13,u}$	0.0085	0.0085	0.0085	0.0085	0.0085	0.0085	0.0085	0.0085	0.0085	0.0085	0.0085
$\gamma_{23,u}$	0.0065	0.0065	0.0065	0.0041	0.0065	0.0065	0.0065	0.0065	0.0065	0.0065	0.0065
$r_{11}^+$	0.01	0.01	0.01	0.01	0.02	0.01	0.01	0.01	0.01	0.01	0.01
$r_{11}^-$	0.05	0.05	0.05	0.05	0.05	0.05	0.04	0.04	0.04	0.04	0.05
$r_{22}^+$	0.02	0.02	0.05	0.05	0.01	0.01	0.03	0.03	0.05	0.05	0.05
$r_{22}^-$	0.50	0.50	0.20	0.20	0.20	0.20	0.25	0.25	0.32	0.32	0.20
$r_{33}^+$	1	1	1	1	1	1	1	1	1	1	1
$r_{33}^-$	1	1	1	1	1	1	1	1	1	1	1
$r_{12}$	1	1	0.01	0.01	1	1	1	1	1	1	0.01
$r_{13}$	0.4	0.4	0.4	0.4	0.4	0.4	0.4	0.4	0.4	0.4	0.4
$r_{23}$	0.4	0.4	0.4	0.4	0.4	0.4	0.4	0.4	0.4	0.4	0.4
$\eta_i^\pm$	0.001	0.001	0.001	0.001	0.001	0.001	0.001	0.001	0.001	0.001	0.001
$\alpha$ [m]	0.030	0.030	0.015	0.015	0.040	0.040	0.050	0.050	0.030	0.030	0.015

**Table D.2:** Input data for FE models: damage progression parameters for all materials.